Stony Brook University

Structural and Optical Characterization of Semiconductors for Solar Water Splitting

A Dissertation Presented

by

Andrew Malingowski

to

The Graduate School

in Partial Fulfillment of the

Requirements

for the Degree of

Doctor of Philosophy

in

Chemistry

Stony Brook University

December 2014

Stony Brook University

The Graduate School

Andrew Malingowski

We, the dissertation committee for the above candidate for the

Doctor of Philosophy degree, hereby recommend

acceptance of this dissertation.

Peter G. Khalifah – Dissertation Advisor
Associate Professor, Department of Chemistry, Stony Brook University

Michael G. White - Chairperson of Defense
Professor, Department of Chemistry, Stony Brook University

Clare P. Grey – Third Member of Defense
Professor, Department of Chemistry, Stony Brook University

Glen Kowach – Outside Member of Defense
Professor, Department of Chemistry, City College of New York

This dissertation is accepted by the Graduate School

Charles Taber
Dean of the Graduate School

Abstract of the Dissertation

Structural and Optical Characterization of Semiconductors for Solar Water Splitting

by

Andrew Malingowski

Doctor of Philosophy

in

Chemistry

Stony Brook University

December 2014

Finding a clean and renewable source of energy that can compete commercially with fossil fuels is one of the great challenges facing the world today. Photoactive semiconductors that can be used to split water into hydrogen and oxygen gas by absorbing visible light are one means of harvesting the sun's abundant energy and storing it as chemical fuel. Although several photoactive semiconductor systems have demonstrated water-splitting, one is yet to be found that has a high enough H_2 production efficiency to be a commercially viable source of renewable energy. Water-splitting using a photoactive semiconductor is a complex process requiring the optimization of several factors if the reaction is to proceed. This research focuses on understanding the bulk properties of photoactive semiconductors, such as structure and light absorption and their relationship to overall H_2/O_2 production efficiency.

$InTaO_4$ was the first photoactive semiconductor reported to show overall water-splitting activity without an applied bias when exposed to visible light. The material's H_2/O_2 production efficiency was reported to increase greatly when doped with Ni. Much research has been done attempting to maximize the efficiency of this compound via doping or other methods. However before this work no studies have closely focused on the material's bulk structure or light absorption. The valence state of the Ni substituted into the $InTaO_4$ lattice was determined to be 2+ using X-ray absorption near-edge spectroscopy and magnetic susceptibility measurements. The synthesis was re-examined resulting in higher quality single phase samples. X-ray and neutron diffraction were used to construct a new partial phase diagram for the In_2O_3-Ta_2O_5-NiO system and $(In_{1-x}Ni_{2x/3}Ta_{x/3})TaO_4$. A Ni solubility limit of $x \approx 0.18$ was determined for Ni-doped $InTaO_4$. Diffuse reflectance measurements showed that the 3.96 eV band gap of undoped $InTaO_4$ was only slightly reduced (< 0.2 eV) with Ni doping and that the material's visible light absorption was due to a weak $^3A_{2g} \rightarrow {}^3T_{1g}$ internal $d \rightarrow d$ transition that is commonly seen in Ni containing oxide compounds when Ni^{2+} is octahedrally coordinated.

Oxynitrides are a promising family of compounds for visible light water-splitting because of their smaller band gaps compared to oxides, advantageously placed band edges and chemical stability. The perovskite-like compound $LaTiO_2N$ was demonstrated to be capable of reducing H^+ to H_2 using methanol as a sacrificial electron donor and to be capable of oxidizing water to O_2 in the presence of Ag^+, making it an interesting candidate for further study. The color of $LaTiO_2N$ powder made by nitriding different lanthanum oxides varies from orange (La_2TiO_5 precursor) to red ($La_4Ti_3O_{12}$ precursor) to brown ($La_2Ti_2O_7$ precursor) as the La content of the starting lanthanum oxide decreases. The structure of $LaTiO_2N$ was examined using X-ray and neutron powder diffraction and the red compound was found to have a slightly larger unit cell

than the other two colors. Diffuse reflectance was used to examine the compounds' visible light absorption and the band edge of the red sample was found to be 2.06 eV, approximately 0.2 eV lower than those of the orange and brown samples, 2.23 eV and 2.20 eV respectively. Additional absorption below the band edge was also seen in the red and brown samples and was attributed to (1) Ti^{3+} and (2) free carriers in the $LaTiO_2N$ sample.

The optical properties of thin films of $LaTiO_2N$ grown on both $La_2Ti_2O_7$ and $La_5Ti_5O_{17}$ single crystal substrates were examined using spectroscopic ellipsometry. The onset of absorption is very rapid with a visible light absorption coefficient greater than 10^5 cm^{-1} by 2.45 eV. The absorption above the band gap was modeled and both the oxygen and lower-lying nitrogen valence states can be clearly seen. The measured spectrum was found to agree with the absorption spectrum of model superstructures with partial O/N ordering calculated using DFT. The O/N ordering on the anion site was separately investigated using pair distribution function analysis on X-ray and neutron diffraction data collected on the powdered $LaTiO_2N$ samples.

This thesis is dedicated to Charlie and Lindy Malingowski, Joe and Nancy Brownrigg and Stacey Hardke.

Table of Contents

List of Figures

List of Tables

List of Abbreviations

ADPs	Anisotropic Displacement Parameters
DFT	Density Functional Theory
DR	Diffuse Reflectance
EXAFS	Extended X-ray Absorption Fine Structure
KM	Kubelak-Munk
NHE	Normal Hydrogen Electrode
PDF	Pair Distribution Function
PV	Photo Voltaic
REELS	Reflection Electron Energy Loss Spectroscopy
TEM	Transmission Electron Microscopy
VSM	Vibrating-Sample Magnetometer
XAFS	X-ray Absorption Spectroscopy
XANES	X-ray Absorption Near Edge Spectroscopy
XRD	X-ray Diffraction

Acknowledgments

I would like to thank Professor Peter Khalifah for his guidance and for all the opportunities he provided for me over the last seven years. I've gotten to see, do and learn some amazing things during the course of my graduate school career and I will always be grateful for everything my mentor has done for me. When I joined his research group it was empty rooms and three people. I love being a trendsetter and consider myself very lucky to have been part of the Khalifah group before it was cool.

I would like to thank all of the current and past Khalifah group members. I had a blast working with you guys. Thanks for looking after my turtles. I would like to say a special thank you to Limin Wang, Yuri Janssen, and Polina Burmistrova. The one thing my graduate school experience lacked was a senior student to show me the ropes. Thanks you for all your help.

I would also like to thank my committee members Professor Clare Grey and Professor Michael White for all of the advice, guidance and support they gave me throughout my time here. I am indebted to Professor Peter Stephens (Dept. of Physics, Stony Brook University) and Professor Jonathan Hanson (Dept. of Chemistry, Brookhaven National Laboratory) for teaching me everything I know about X-ray diffraction at a synchrotron. Professor Stephens pointed out the cot he keeps at his beam line and Professor Hanson loaned me quarter so I could buy a much-needed Coke. These things alone make them heroes to me.

I would like to acknowledge all of my friends at Stony Brook, but there are too many. You know who you are and you are great. This includes everyone involved with the Alan Alda Center for Communicating Science. I had to present this dissertation, so thanks guys.

I would like to thank all of the members of Renegade Improv. You are the absolute best. Charlie, Ken, Lauren, Socrates, Shannon, Karen, Scott, Peach, Nick and especially Joanie. I couldn't have done it without you. I actually looked forward to working until 7:00 so I could practice with you guys.

Finally, I would like to thank all of my family. Mom, Dad thanks for all the support you've given me. I know it can't be easy to tell people your son has been in college for a decade and a half. Thank you for not letting me quit. Thank you Knitting Grandma and Grandpa Joe. If you never give me anything ever again I will still consider you the most generous people I will ever have in my life. If I've accomplished anything it is in no small part because of you. Thank you Stacey Hardke for staying with me these last few years. You didn't have to, but you did. Now I have somewhere to go when I leave.

Chapter 1

Introduction

1.1 Motivation

Solar energy is clean, renewable and abundant enough to potentially satisfy the entirety of the world's energy needs[1]. However, only a fraction of global energy is currently produced from solar sources compared to non-renewable sources such as coal, oil and natural gas. Current technologies for harvesting solar energy, such as photovoltaic devices (PV) or wind farming, produce electricity directly and consequently vary greatly in daily and seasonal output making them more difficult to integrate into the existing power grid. Electricity is also very expensive to effectively transport over long distance or store for extended periods, limiting the efficacy of current solar technologies in places with unfavorable weather or where space is at a premium. Photoactive semiconductors that can split water into H_2 and O_2 gas via the process of photoelectrolysis are a means of converting solar energy into a chemical fuel, circumventing many of the transport and storage problems associated with electricity. H_2 produced in this way can be converted into electricity with a fuel cell, simply burned or used as feed-stock for producing hydrocarbons using Fischer−Tropsch reactions[2].

The process of semiconductor water splitting is well known[1, 3]. It was first demonstrated by Honda *et al.* in 1972 using rutile TiO_2 and UV light. Subsequently, several other systems have been developed, some of which can utilize visible light. However, no semiconductors for driving water splitting discovered to date can convert solar radiation to chemical fuel with a high enough overall efficiency to be adopted commercially. Also, expensive materials are often needed to

catalyze H_2 production. Substantial improvements in efficiency are needed before this process can become a viable technology. The mechanism of photoactive semiconductor electrolysis is complex and can be affected by many factors. It is therefore important to examine water-splitting compounds in detail in order to determine their potential water splitting ability and not just rely on overall H_2 production. This dissertation will present the results of such detailed investigations into the structure and optical properties of the photoactive semiconductors $(In_{1-x}Ni_{2x/3}Ta_{x/3})TaO_4$ and $LaTiO_{2-x}N_y$.

1.2 Water-Splitting Photoactive Semiconductors

Some metal oxide semiconductors have properties such that on absorption of light they can be used to produce H_2 and O_2 gas from water by driving the following electrolysis reaction:

(1) $2H_2O \rightarrow 4H^+ + 4e^- + O_2$ +1.23 eV vs. Normal Hydrogen Electrode (NHE)

(2) $4H^+ + 4e^- \rightarrow 2H_2$ 0.0 eV vs. NHE

(3) $2H_2O \rightarrow 2H_2 + O_2$ +1.23 eV vs. NHE

The process, called photoelectrolysis, begins when the absorbed radiation promotes electrons in the material's valence band to the conduction band. The promoted electron and the positively charged hole generated in the valence band are free to travel to the surface of the material. If the magnitude of the energy potential difference, or band gap (E_g), between the two bands is greater than that needed to hydrolyze water, the carriers will have the energy necessary to drive the electrolysis of water producing hydrogen and oxygen, usually with the help of surface catalyst to facilitate the formation of the H_2 and/or O_2 gas.

Thermodynamically only 1.23 eV (1000 nm) are needed to drive the overall reaction. It is

therefore, ignoring all other factors, possible to utilize the majority of the energy of the solar spectrum that the earth receives. In practice about 0.4 eV of extra energy is needed to overcome thermodynamic losses due to the rise in the entropy of mixing when electrons are excited into the conduction band and a total of approximately 0.3-0.4 eV is required to overcome overpotentials if the reaction is to proceed at reasonable rates. This means that to drive a water splitting reaction photoactive semiconducting materials need to have minimum band gaps of ~1eV (653 nm)[4, 5]. The great majority of the light intensity that the earth receives lies in the visible spectrum below ~3.2 eV (400 nm) so an ideal band gap would have an energy between approximately 2 and 3 eV, in the energy range of visible light [1, 4].

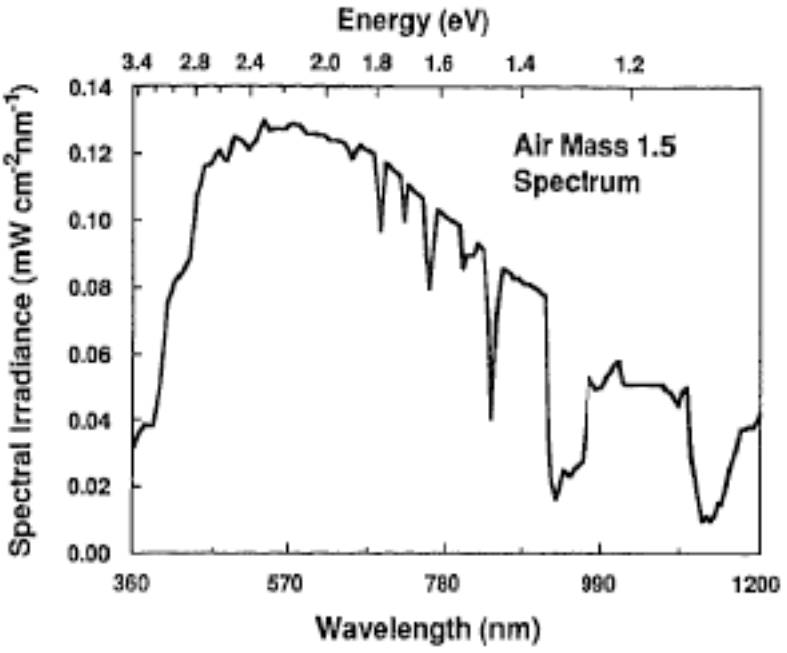

Figure 1.1 The spectral distribution of sunlight under Air Mass 1.5 conditions. Air mass 1.5 refers to a standard measurement condition when the sun is 48° above the horizon. Note that the energy of the majority of the light is in the visible spectrum[1].

In addition to having a band gap of the appropriate magnitude, the band edge energies must be appropriately placed. If the material's conduction band does not lie below the potential

necessary to reduce H_2 gas from H^+ ions (0.0 eV) or the valence band does not lie above the potential necessary to oxidize water to form O_2 gas (1.23 eV), that compound will not have the driving force needed for both the water splitting half-reactions[1]. If a semiconductor is able to drive both halves of the water splitting reaction, exposing a simple powder suspension of the material in water to light is all that is necessary for H_2/O_2 production[6]. If the material can only drive one of the half reactions then in order to split water an applied bias needs to be applied or the semiconductor needs to be paired with an electron (hole) acceptor either in the solution or as a counter electrode in a photochemical cell[1, 3, 6, 7]. (Figure 1.2)

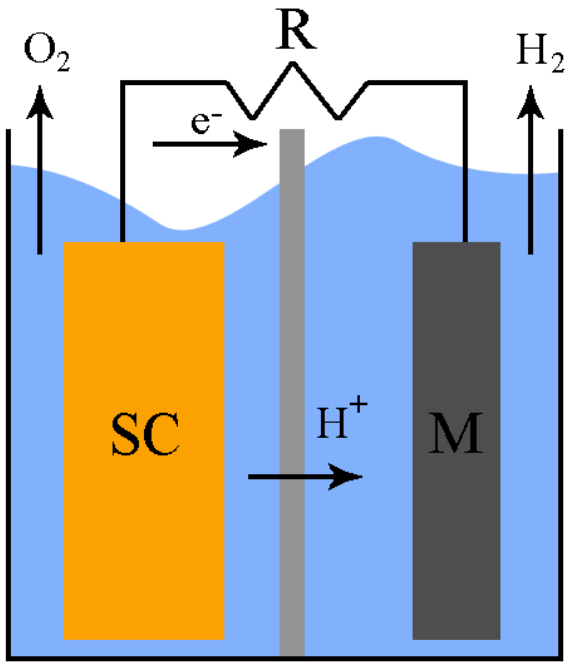

Figure 1.2 A schematic of a photochemical cell. A photochemical cell can produce electricity, H_2 and O_2 gas, or both depending on the chemical reactions at the electrode surfaces. In this schematic light striking the semiconductor cathode (SC) generates holes that oxidize water into O_2 gas and H^+ cations. Electrons travel to the metal anode (M) where H^+ is reduced to H_2 gas[1].

1.3 d^0/d^{10} metal oxides

After the initial report by Honda *et al.* in 1972 little progress was made in developing an

efficient system for water splitting using photoactive semiconductors. This was partially due to the fact that most photoactive semiconductors that demonstrate water splitting utilize UV light, which accounts for only ~5% of the light earth receives. (Figure 1.1) While the conduction bands of many d^0 and d^{10} metal oxide semiconductors are well placed for driving the water-splitting reaction, the valence bands, typically composed of oxygen 2*p* states, generally have a potential of approximately +2 eV vs. NHE[8]. This results in typical band gaps larger than 3 eV (413 nm), which corresponds to absorption in the UV range. (Figure 1.3)

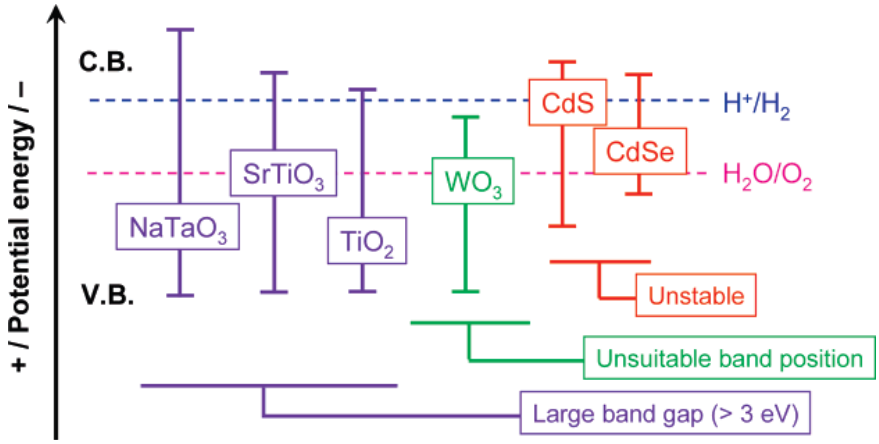

Figure 1.3 This schematic shows the band gap energies of various semiconductors relative to the potential needed to drive the water splitting reaction[7].

Most non-oxide photoactive semiconductors are not stable against photo-corrosion[4]. For instance, the semiconductor CdS does have an appropriately positioned and spaced band gap, but because the sulfur in the semiconductor is more easily oxidized than oxygen in water the compound degrades during the reaction[7, 9].

$InTaO_4$ was the first photoactive metal-oxide semiconductor compound reported to utilize visible light for water splitting, although with low efficiencies (quantum yield of ~0.7% at 402 nm)[5]. Further research into the structure and the absorption behavior of this compound, described later in this report, determined it to be inactive for water splitting utilizing visible light, but its

discovery renewed interest in photoactive semiconductors for water splitting and other systems have been developed that can utilize visible light.

1.4 Oxynitride materials

One promising strategy for developing semiconductor compounds with appropriately placed band edges is to adjust the position of the valence band by doping onto the anionic lattice. Nitrogen can often substitute onto the oxygen sites of transition metal oxides to form oxynitride compounds, because they have similar chemical and structural properties such as ionic radii, coordination number and electronegativity[10, 11]. When nitrogen replaces a portion of the oxygen the hybridization of the oxygen 2*p* orbitals with the 2*p* orbitals of the less electronegative nitrogen raises the energy of the top of the material's valence band. This reduces the material's band gap without greatly affecting the position of the conduction band[9, 10, 12]. Adjusting the O/N ratio can control the magnitude of the material's band gap. For instance, the brightly colored solid solution $Ca_{1-x}La_xTaO_{2-x}N_{1-x}$ shows colors ranging from yellow to red, while typically perovskite type transition metal oxide compounds are either colorless or black, depending on the carrier concentration[11].

The reduced band gap of oxynitride compounds relative to oxide and nitride materials and the ability to adjust the band gap make oxynitrides particularly interesting candidates for use in photoactive water splitting. The compound $(Ga_{1-x}Zn_x)(N_{1-x}O_x)$ has a band gap ranging from 2.6 eV-2.8 eV, smaller that either those of GaN (3.4 eV) or ZnO (2.8 eV), and shows H_2 and O_2 production from pure water using wavelengths less than 460 nm when loaded with an appropriate surface catalyst[9]. The transition metal oxide perovskite compound $LaTiO_2N$ was shown to reduce H^+ to H_2 using methanol as a sacrificial electron donor and oxidizing H_2O to O_2

using Ag^+ as a sacrificial electron acceptor when exposed to wavelengths as long as 600 nm (2.07 eV)[13]. Both of these compounds showed no decomposition over the course of the water splitting reaction reflecting the relative stability of oxynitride compounds which are generally also stable in acid and on heating in air to several 100° C. $LaTiO_2N$ powders are purified by washing with ~2M nitric acid and do not degrade until heated in air to ~300° C.

1.5 Perovskite derived structures

The oxynitride $LaTiO_2N$ and the oxides $La_2Ti_2O_7$ and $La_5Ti_5O_{17}$ investigated in this report have structures derived from the perovskite structure. Octahedral tilting is a simple model that can be used to describe their complicated structures in terms of their perovskite like features.

The perovskite structure consists of metal-anion octahedra that corner share on each of their tetrad axes. The relationship of perovskite derived structures to the undistorted structure can be described by imagining the Ti-O(N) octahedra as rigid units that are tilted relative to the original cubic axes. Since the octahedra are connected by their corners, a tilt applied to the octahedra in any direction effects the crystal structure in a predictable way. The general method for describing perovskite related structures in terms of the tilts of the B-site octahedra was first described by A. M. Glazer[14]. In the notation used by Glazer unequal tilts of the *B*-site octahedra about the [100], [010] and [001] axes of the pseudocubic cell are denoted *a*, *b*, and *c*. When tilts are equal they are given the same letter, for example *aac* would indicate two equal tilts about the [100] and [010] axes a different tilt along the [001] axis. The tilts of the *B*-site octahedra along any given axis are constrained by the tilts of the neighboring octahedra in the perpendicular directions, but are unaffected by the tilts of the octahedra along the that axis. Neighboring octahedra along that axis can have no tilt, denoted "0", the same sense of tilt, denoted "+", or the

opposite sense of tilt, denoted "-".

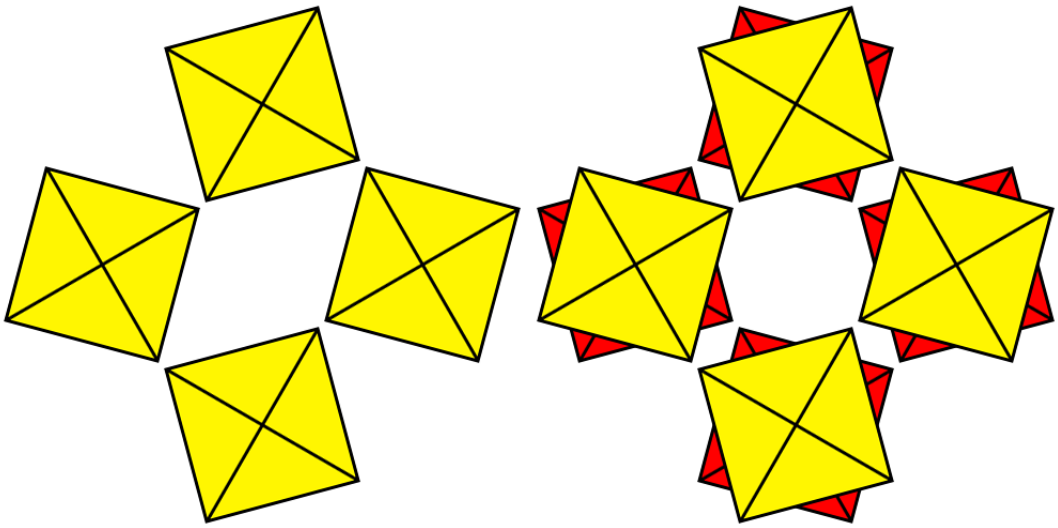

Figure 1.4 A view of a "+" octahedral tilt (left) and a "-" octahedral tilt (left) viewed along the tilt axis.

The space group associated with each tilt system can be determined, however further lowering of symmetry is possible due to atom displacement. For example, $LaTiO_2N$ has an $a^-b^-c^-$ tilt system where tilts in all directions have different magnitudes and octahedra along each tilt axis have the opposite sense of tilt. This corresponds to the *P-1* space group (#2)[14, 15]. Most structures cannot be described by tilting alone however since ordering on either the cation or anion sites and octahedral distortion will further affect the symmetry[16].

The situation becomes more complicated in layered structures like those of $La_2Ti_2O_7$, and $La_5Ti_5O_{17}$. These and other $A_nB_nX_{3n+2}$ structures are composed of slabs of perovskite layers that run parallel to the cubic {110} direction[17]. Other structure types where the layers run parallel to the cubic {001} or {110} direction have also been identified[17]. In each layer tilting relative to the tetrad axes of the octahedra affects the layer similar to the effect of tilting in the 3-dimensional structures. A gap, or spacer separates these layers from each other. A motif is a distinct repeat

unit in the structure, either a single layer if all the layers are identical, or multiple layers in mixed layer compounds[17]. Each layer in a motif can have either an even (**e**) or odd (**o**) number of layers. The tilting within the layers, the types of layers in a motif (**e**, **o** or both), their stacking sequence and the relative directions of the octahedral tilts between motifs all determine the symmetry of the structure[17].

1.6 Research goals

There are six factors that limit the water-splitting efficiency of a given semiconductor: lack of driving force in the valence or conduction bands, loss of energy due to the band gap, the lack of carrier concentration and kinetic barriers at either the O_2 or H_2 nucleation sites[7]. Because of the complexity of the water-splitting reaction using a photoactive semiconductor the efficiency can be adversely affected in many ways, making overall H_2 production a poor metric for determining a material's merit. This research focuses on, understanding the materials' bulk properties and how they contribute to the overall water-splitting efficiency.

1.7 Analytical techniques

1.7.1 Magnetic susceptibility measurements

The magnetic susceptibility of Ni-doped $InTaO_4$ was measured using a vibrating-sample magnetometer (VSM)[18]. Magnetic susceptibility (χ_n) is a dimensionless value that relates the magnetization (M) of a material to the strength of an applied magnetic field (H):

$$M = \chi_n H$$

Measurements are done in an applied constant magnetic field. The sample to be measured, in our case a small powdered sample of Ni-doped $InTaO_4$, is vibrated linearly, in the direction

perpendicular to the magnetic field, between two induction coils. The magnetic moment is determined from the voltage generated by the movement of the sample past the coils.

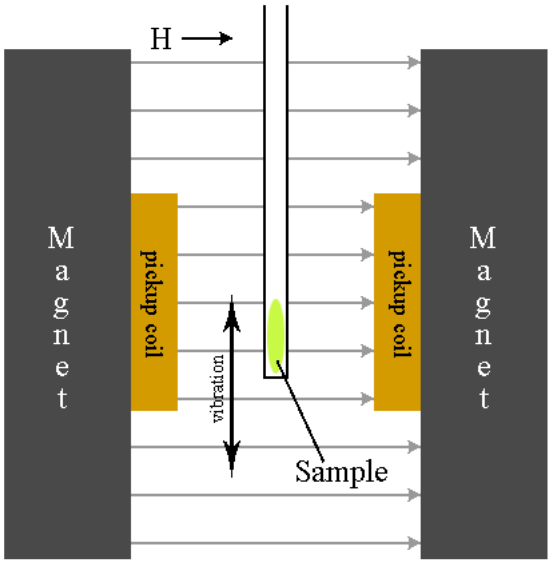

Figure 1.5 A simple schematic of a VSM experiment[18].

The behavior of the magnetic susceptibility in diamagnetic materials with small concentrations of magnetic ions as a function of temperature can be modeled using the Curie-Weiss law:

$$\chi_n = \chi_0 + C/(T-\theta)$$

where χ_n is the magnetic susceptibility, C is the Curie constant, θ is the Weiss constant and χ_0 is the temperature independent diamagnetic contribution[19]. From C the effective magnetic moment per ion (μ_{eff}) can be calculated from:

$$\mu_{eff} = ((3Ck_B/N_A)^{1/2})/\mu_B$$

where N_A is Avogadro's number and k_B is the Boltzmann constant and, μ_B is the Bohr magneton[20]. For Fe and Pt group elements the crystal field quenches the orbital contribution to the angular momentum the values of μ_{eff} for iron group ions can be calculated using the spin only (S) contribution[19]:

$$(\mu_{eff}) = 4(S(S+1))^{1/2}$$

S is easily determined by assigning a value of $S = 1/2$ to each unpaired valence electron predicted for the magnetic ion's spin state and taking the sum. By comparing the μ_{eff} values determined from the experimentally determined χ_n and the theoretical values calculated for different values of S for the ion being examined the oxidation states can be determined[19, 20].

1.7.2 X-ray absorption fine-edge spectroscopy

X-ray absorption fine-edge spectroscopy (XAFS) experiments can be used to determine the local environment and the oxidation state of specific elements in a material. XAFS data is collected by focusing a monochromatic beam of X-rays on a sample and varying the X-ray energy. How strongly the material absorbs X-rays as a function of energy, or the X-ray absorption coefficient $\mu(E)$ is determined. In this work, absorption was determined by measuring the samples' fluorescence as a function of energy, but it is also possible to determine absorption by measuring the transmitted beam intensity[21]. An example of XAFS data is shown in Figure 1.5.

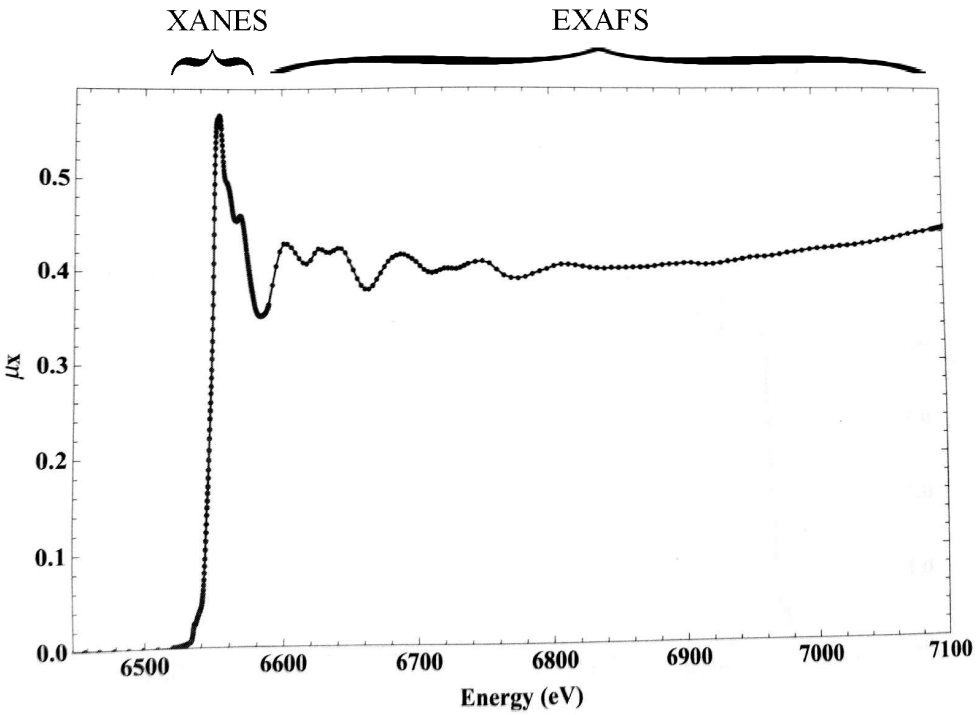

Figure 1.6 The XAFS spectra of Mn_2O_3 taken at 160K. The XANES and EXAFS portions of the pattern are indicated[21].

In XAFS experiments the energy of the X-ray beam is swept over a range close to the ionization energy of a core electron belonging to the particular element of interest. The sharp increase in absorption that corresponds to the transition energy for a core electron is called the absorption edge. The exact energy of this transition is affected by the oxidation state of the atom and the coordination environment. The ejected electron then propagates through the material as a spherical wave exciting the surrounding nuclei. Back scattering effects affect the absorption at energies above the absorption edge and can be used to determine the pair distribution function of the atoms surrounding the measured element, which can then be fit to structure models.

This work is primarily interested in the XANES region of the data. Analysis of the extended structure data (EXAFS region) is complex and beyond the scope of this work. Aside

from some normalization and background determination done on the raw spectrum, determining the oxidation state of an ion using XANES data is relatively straightforward. Data for the sample is collected along with a reference material, usually a metal foil of the same type as the target atom. Data is also collected using this same reference foil for several standards that contain the same element in similar coordination environments, but with different known oxidation states. Proper reference materials need to be used to minimize the contribution to the edge energy from atomic coordination. The unknown oxidation state of the ion in the sample can be determined by comparing the position of the absorption edges after aligning them using the reference spectrum.

1.7.3 Spectroscopic ellipsometry

Spectroscopic ellipsometry is a technique that can determine the absolute optical constants of a crystalline thin film as a function of wavelength as well as some physical properties such as film thickness and density. In this work spectroscopic ellipsometry was used to examine $LaTiO_2N$ films grown from $La_2Ti_2O_7$ single-crystal substrates. An ellipsometry experiment consists of reflecting a beam of circularly polarized light off of a flat crystalline surface. When the light is reflected back through the sample the polarization and intensity change is measured and is used to determine the properties of the sample.

When a beam of light hits a material a portion of the light reflects off of the surface and a portion is transmitted into the material. This process is called refraction and is described by Snell's Law:

$$\tilde{N}_1 \sin\phi_1 = \tilde{N}_2 \sin\phi_2$$

where ϕ_1 is the angle of incidence, ϕ_2 is the angle of reflection and $\tilde{N}$ is the complex index of refraction:

$$\tilde{N} = n - ik$$

where n is the index of refraction, k is the extinction coefficient which in absorbing materials $k \neq 0$. k is related to the absorption coefficient (α) as described in Beer's Law:

$$\frac{I}{I_0} = e^{-\alpha x}$$

by

$$k = \left(\frac{\lambda}{4\pi}\right)\alpha$$

In the case of a light wave hitting a single surface the amplitude of the reflected wave is given by the Fresnel reflection coefficients:

$$r_{12}^{p} = \frac{\tilde{N}_2 \cos\phi_1 - \tilde{N}_1 \cos\phi_2}{\tilde{N}_2 \cos\phi_1 + \tilde{N}_1 \cos\phi_2} \qquad \text{and} \qquad r_{12}^{s} = \frac{\tilde{N}_1 \cos\phi_1 - \tilde{N}_2 \cos\phi_2}{\tilde{N}_1 \cos\phi_1 + \tilde{N}_2 \cos\phi_2}$$

where the p and s superscripts represent the component of the wave parallel and perpendicular to the plane of incidence respectively. For the case of a two-layer sample the portion of the light reflected off of the second interface interferes with the light reflected off of the first interface. In this case the total reflection coefficients are defined as:

$$R^{p} = \frac{r_{12}^{p} + r_{23}^{p}\exp(-i2\beta)}{1 + r_{12}^{p} r_{23}^{p}\exp(-i2\beta)} \qquad \text{and} \qquad R^{s} = \frac{r_{12}^{s} + r_{23}^{s}\exp(-i2\beta)}{1 + r_{12}^{s} r_{23}^{s}\exp(-i2\beta)}$$

where:

$$\beta = 2\pi\left(\frac{d}{\lambda}\right)\tilde{N}_2 \cos\phi_2$$

This case can be expanded for additional layers.

The quantity Ψ is defined as:

$$\tan \Psi = \frac{\left|R^p\right|}{\left|R^s\right|}$$

During reflection a phase shift often occurs. If δ_1 is the phase difference between the p-waves and s-waves before reflection and δ_2 is the phase difference after reflection then the phase shift caused by the reflections:

$$\Delta = \delta_1 - \delta_2$$

The fundamental equation of ellipsometry relates Ψ and Δ to the complex ratio of the total reflection coefficients:

$$\frac{R^p}{R^s} = \tan \Psi e^{i\Delta}$$

Ψ and Δ are the quantities measured in an ellipsometry experiment and from them all other values are calculated. Although it is possible to calculate a unique set of *n* and *k* values from Ψ and Δ when the sample has only one layer, it is not possible to find *n* and *k* values on multilayer samples without using regression analysis. In order to extract meaningful values from spectroscopic ellipsometry measurements the data needs to be fit to a sample model. A typical model consists of a substrate layer of infinite thickness below one or more layers of finite thicknesses. The optical properties of each layer are modeled using a variety of mathematical models depending on the nature of each layer. Using an inaccurate sample model will result in incorrect values for the optical constants, but often will still result in a reasonable fit. It is

important to verify that the model being used truly reflects the sample structure. In this work scanning electron microscopy (TEM) was used to inform the ellipsometry models.

The complex dielectric constant ($\tilde{\varepsilon}$), which describes the degree to which a material can be polarized by an applied external electric field, is often used in place of $\tilde{N}$ in this research. $\tilde{\varepsilon}$ is related to $\tilde{N}$ by: $\tilde{\varepsilon} = \tilde{N}^2$. Like the complex index of refraction $\tilde{\varepsilon}$ is also a complex number and can be expressed as $\tilde{\varepsilon} = \varepsilon_1 + i\varepsilon_2$ where ε_1 and ε_2 are the real and imaginary parts respectively. They are related to n and k by:

$$n = \sqrt{\tfrac{1}{2}\left[\left(\varepsilon_1^2 + \varepsilon_2^2\right)^{1/2} + \varepsilon_1\right]} \qquad \text{and} \qquad k = \sqrt{\tfrac{1}{2}\left[\left(\varepsilon_1^2 + \varepsilon_2^2\right)^{1/2} - \varepsilon_1\right]}$$

Four different oscillator functions are used to model the transitions in the ellipsometry spectra in this research: the Lorentzian oscillator, the Gaussian oscillator, the Tauc-Lorentz oscillator and the Drude oscillator (Appendix 2).

Raw ellipsometric data can be presented in terms of ε_1 and ε_2 (or n and k) without being fit to a model. These values are referred to as "pseudo-dielectric constants" or "pseudo-optical constants" in this research and are calculated by modeling the entire sample as a substrate. This allows the raw data to be compared to the calculated spectra in terms of n and k (or ε_1 and ε_2), but they do not represent the actual values of the constants.

Because of the sensitivity of the technique and the large number of parameters great care must be taken to prepare samples to minimize variables and ensure meaningful results. The film samples must be flat on the scale of the wavelengths used in the experiment to prevent surface roughness effects, although these can be modeled in some cases. Films should also be checked for things such as homogeneity and the presence of surface layers as these can greatly change the

results if they are not included in the fitting model. If transparent substrates are being used the backsides should be made rough to prevent light reflected off of the back of the sample from interfering with the data.

1.7.4 Diffuse reflectance measurements

Diffuse reflectance (DR) spectroscopy was used to investigate the light absorption behavior of powdered semiconductor samples. Light reflected off of a matte material, such as a densely packed powder, has a specular and diffuse component. The diffuse component is the portion of the incident light that penetrated the sample and was scattered off the volume of particles that compose the sample before it is reflected back. There is no quantitative solution that describes this type of multiple scattering in a matte material, however based on the observation that a matte surface irradiated with constant intensity appears uniformly lit at all angles, the intensity of light radiated from an ideal non-absorbing diffuser can be described by the Lambert cosine law[22]:

$$B = \left(I_0/\pi\right)\cos\gamma\cos\theta$$

where I_0 is the radiation strength at perpendicular incidence, γ is the angle of incidence and θ is the angle of observation. According to this law the intensity of the reflected light is the same for all values of γ and θ; an approximation that is generally true for compressed powder samples.

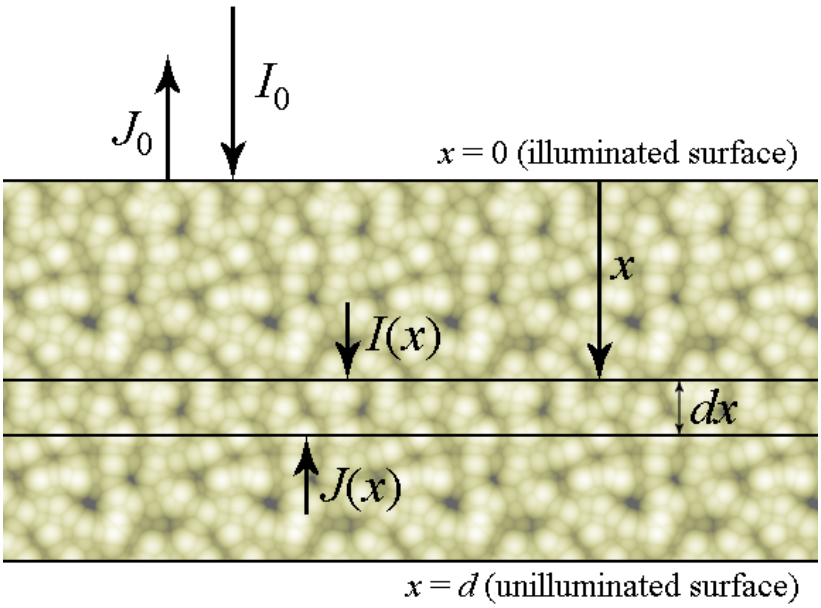

Figure 1.7 A schematic of a layer of light absorbing, light scattering particles[22].

An absorbing sample can be described using the Kubelka-Munk Theory in terms of two coefficients, *s* and *k*, that are proportional to the fraction of light scattered and absorbed respectively. The sample is modeled as a layer composed of light-absorbing and light-scattering particles of a size smaller that the thickness of the layer (*d*) that are uniformly and randomly distributed above a background layer with reflectance R_g. The surface of this layer at x = 0 is lit with monochromatic light (I_0). Light radiated in the positive *x* direction is *I* and in the *-x* direction is *J*. Only light reflected perpendicular to the surface of the layer is considered. Using this model, for incident light traveling through an infinitesimal layer of thickness *dx*, the intensity of *I* is decreased by absorption and increased by the scattering of *J*. *J* is similarly described. (Figure 1.6) The following equations can be derived in terms of *s* and α (assuming an ideal diffusion)[22-24]:

$$dI = -(\alpha + s)Idx + sJdx$$

$$dJ = (\alpha + s)Jdx - sIdx$$

These equations can be integrated using the boundary conditions:

$I = I_0$ for $x = 0$

$I = I_{x=d}$, $J = 0$ for $x = d$

to obtain the formulas for transmittance (T) and diffuse reflectance (R).

$$T \equiv \frac{I_{x=d}}{I_0} = \frac{2\beta}{(1+\beta^2)\sinh \kappa d + 2\beta \cosh \kappa d}$$

$$R = \frac{J_{x=0}}{I_0} = \frac{(1-\beta^2)\sinh \kappa d}{(1+\beta^2)\sinh \kappa d + 2\beta \cosh \kappa d}$$

where:

$$\kappa \equiv \left[\alpha(\alpha + 2s)\right]^{1/2} \qquad \text{and} \qquad \beta \equiv \left[\alpha/(\alpha + 2s)\right]^{1/2}$$

If there is no scattering in the layer ($s = 0$) then the Beer-Lambert law is recovered[23] $T = e^{-kd}$. For the case where $d = \infty$, as in a thick, compacted powder sample, $T_\infty = 0$ and R_∞ = the Kubelka-Munk (KM) function[22]:

$$R_\infty = \frac{1 - \left[\alpha/(\alpha + 2s)\right]^{1/2}}{1 + \left[\alpha/(\alpha + 2s)\right]^{1/2}}$$

which is usually rewritten to give the ratio of the absorption coefficient to the scattering coefficient (k/s)[22-24]:

$$\frac{\alpha}{s} = \frac{\left(1 - R_\infty\right)^2}{2R_\infty}$$

The diffuse reflectance is measured using an integrating sphere coated with a high reflectance material. The diffuse reflectance of the sample is measured relative to a reflectance standard that is assumed to be 100% reflecting in the energy range of interest[22].

$$\frac{R_{\infty\, sample}}{R_{\infty\, std}} = r_\infty$$

r_∞ replaces R_∞ in the KM function. After the data is converted to α/s values using the (KM) function the magnitude of the band gap (E_g) can be determined from the resulting curve by fitting it with either a direct transition model, where there is no momentum change[25]:

$$\frac{\alpha}{s} = A\left(E - E_g\right)^{1/2}$$

where A is a scaling constant, or an indirect transition model, where there is a momentum change via an accompanying phonon[25]:

$$\frac{\alpha}{s} = A\left(E - E_g\right)^2$$

depending on the material being measured. Often there is additional absorption below the band gap due to the Urbach tail. This effect is caused by broadening of the valence and conduction bands due to sample imperfections. The attenuation of this part of the reflection due to absorption is given by the Brouguer-Lambert Law[25]:

$$I = I_0 \exp(-\varepsilon' d)$$

where I and I_0 are the reflected and incident intensity respectively, ε' is the molar extinction coefficient and d is the penetrated layer thickness. The Brouguer-Lambert Law is another way of stating Beer's Law. Fitting this region in addition to the region dominated by the electronic transition improves the accuracy of the value obtained for the magnitude of the band gap. It is important to remember that although diffuse reflectance can be used to determine accurate values for E_g this method measures the dimensionless ratio α/s and not the absolute values of absorption coefficient as a function of energy.

1.7.5 X-ray diffraction

X-ray diffraction techniques are used to determine long-range structure information on crystalline compounds. Because it is possible to get a large amount of structure information relatively easily, X-ray diffraction data was used for day-to-day analysis (laboratory X-ray) and more detailed analysis (synchrotron). X-ray diffraction can be done on both single crystal samples and crystalline powders. The theory behind both types of experiments is the same.

Crystals are composed of a regular arrangement of atoms that extends in three dimensions. A unit cell is a parallel piped that encloses the smallest repeatable unit from which the extended structure of the crystal can be obtained via translation. The unit cell is described by the length of each edge a, b and c and by three angles α, the angle between the bc-plane and the a-axis; β, the angle between the ac-plane and the b-axis and γ, the angle between the ab-plane and the c-axis. The rotational symmetry of the unit cell defines it as belonging to one of seven categories called Bravis lattices. The atoms inside the unit cell can be related to each other by additional symmetry elements such as rotations, reflections, etc. The total three-dimensional

symmetry of the unit cell is referred to as the cell's space group. The space group and the positions of the atoms inside the unit cell are all that is need to describe a material's extended crystal structure.

Miller indices are a convenient way to describe structural motifs in a crystal. A set of planes can be defined by different sets of atoms in that run through the crystal lattice. Families of these planes can be described by the distance that separates them as they intersect the unit cell or their *d*-spacing. The Miller indices are inversely related to the fraction of the unit cell that separates them in the *a*, *b* and *c* directions, which correspond to the *h*, *k* and *l* directions respectively.

In an X-ray diffraction experiment, a crystal is exposed to a monochromatic beam of X-rays that scatter off all the electrons of the constituent atoms in tandem. Only X-rays that scatter between transitionally equivalent atoms meet this requirement. This creates an interference pattern and only those waves that constructively interfere reach the detector. When discussing diffraction from a crystal lattice a convention called Bragg's law is generally used.

$$n\lambda = 2d_{hkl}\sin\theta_{hkl}$$

where λ is the radiation wavelength, d is the interplanar spacing, θ is the Bragg angle and n is the order of reflection. Bragg's law allows the diffraction conditions to be easily calculated by modeling the crystal as families of lattice planes described the Miller indices.

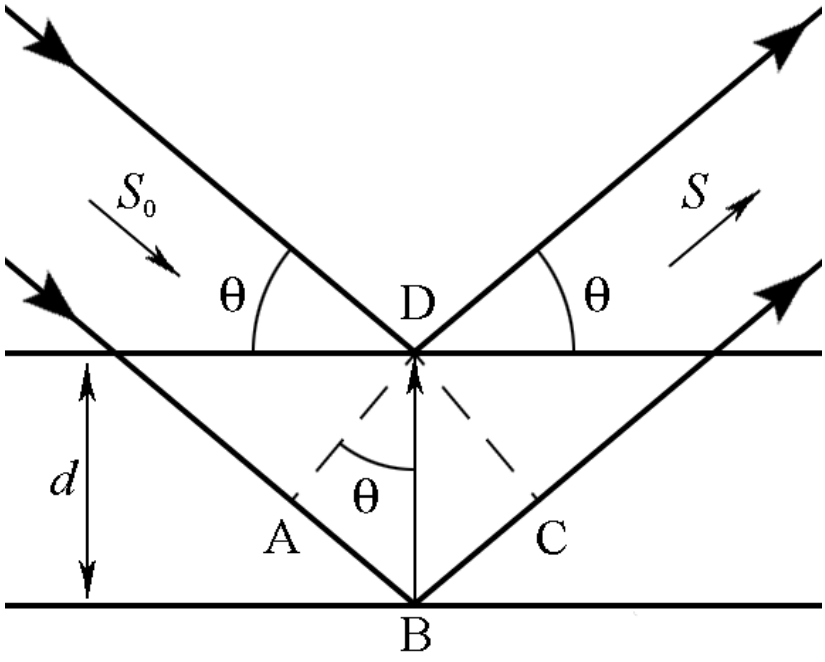

Figure 1.8 A schematic representation of Bragg's Law[26].

As can be seen from Figure 1.8, when the distance AB+AC equals an integer number of wavelengths the Bragg conditions are met. This happens at integer values *h*, *k* and *l*. The resulting diffraction pattern, called the reciprocal lattice, is a pattern of spots where each reflection represents one family of lattice planes separated by a given *d*.

The intensity of the coherent scattered X-ray beam is proportional to the square of the total diffraction of a crystal or structure factor (F_{hkl}):

$$I_c \propto |F_{hkl}|^2$$

Each atom in the compound's unit cell contributes to the total scattering. The scattering that originates from atoms within the unit cell that do not satisfy the diffraction condition for a given

θ destructively interferes with the Bragg reflection and decreases its intensity. This affect is what allows the crystals structure to be determined from diffraction.

The amount that any atom scatters is defined by its atomic scattering factor (f) which in X-ray diffraction increases with atomic number (Z) and is a function of the scattering angle (θ). The total scattering factor (F_{hkl}) is a function of the individual atomic scattering factors summed over all of all the unitcell:

$$F_{hkl} = \sum_{j=1}^{N} f_j \exp 2\pi i\left(hx_j + ky_j + lz_j\right) = A_{hkl} + iB_{hkl}$$

where:

$$A_{hkl} = \sum_{j=1}^{N} f_j \cos 2\pi\left(hx_j + ky_j + lz_j\right), \qquad B_{hkl} = \sum_{j=1}^{N} f_j \sin 2\pi\left(hx_j + ky_j + lz_j\right)$$

where h,k,l are the indices of refraction.

or

$$F_{hkl} = \left|F_{hkl}\right| \exp(i\varphi_{hkl}) \text{ , where } \varphi_{hkl} = \arctan(B_{hkl}/A_{hkl})$$

φ_{hkl} is the phase of the structure factor. Figure 1.9 shows graphically how the individual atomic scattering factors sum to the structure factor. Unfortunately only the real portion of F_{hkl}, is measureable. Since the phases of the structure factors are not known it is not possible to directly find an exact solution for the crystal structure from diffraction data. This is known as the *phase problem*.

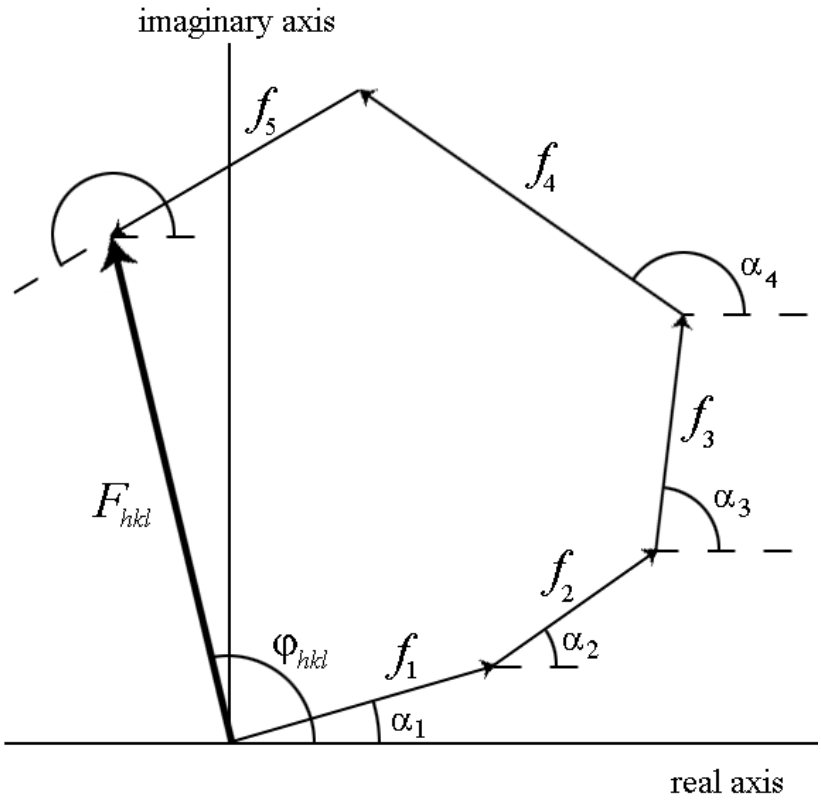

Figure 1.9 A plot of the real and imaginary components of the total scattering factor[26].

If the phases were known, electron density distribution could be calculated from the total structure factor by the equation:

$$\rho(r) = \frac{1}{V}\sum_{hkl} F_{hkl} \exp\left(-2\pi i\left(hx + ky + lz\right)\right)$$

where V is the unit cell volume. This is called a Fourier synthesis of the electron density. However, because of the phase problem, generating electron density maps in this way is not possible, so structures are determined by calculating the diffraction of a model and then comparing that model to the experimental data using least squares analysis. Various structural parameters are refined during the fitting and until the model matches the data within the error of the experiment.

1.7.6 Powder diffraction

Powder diffraction was used much more frequently in this research than single crystal diffraction and the underlying principles are the same as those of single crystal diffraction. In a powder diffraction experiment a polycrystalline sample is used in place of a single crystal. Each grain in the illuminated sample volume is assumed to be randomly oriented single crystal. The reciprocal lattices are therefore also randomly oriented causing the vectors of the scattered beam to be oriented around the surface of a cone that has its apex at the center of the Ewald sphere and its lower edge (Debye ring) on the surface of the Ewald sphere perpendicular to the incident beam. The major consequence of this is that instead of a unique reflection corresponding to each lattice plane, as in a single crystal experiment, the diffracted intensity from all lattice planes with the same *d*-spacing are overlapped together on the same Debye ring. Powder diffraction data is usually presented as an intensity histogram as a function of Bragg angle 2θ or sometimes as a function of interplanar spacing, *d* or *Q*. The intensity histogram is constructed by either averaging the intensity around the entire Debye ring collected using a 2-dimensional plate detector or by measuring only a thin strip of the Ewald sphere using a 1-dimensional detector. Either way the end result is a powder diffraction pattern consisting of several peaks.

Structure information is extracted from a powder diffraction pattern by analyzing the peaks. Peak position gives information about unit cell parameters. Peak shapes give information about crystallite size and strain. Peak intensities give information about atomic positions inside the unit cell and atomic displacement parameters.

Rietveld refinement is the analysis technique used to extract this structure information from powder diffraction data. Rietveld refinement begins with a structure model, often determined from a single crystal experiment or by comparison to a similar compound. A position

and intensity for each Bragg peak is calculated from this model and convoluted with a profile function. The profile function models deviations from ideal peak shape due to experimental effects, such as size and strain, absorption, background, etc. The calculated intensity is compared to the data and individual parameters are refined using the method of least squares to improve the fit until the calculated and experimental patterns match within the experimental error.

Three important fit parameters used are the R-factor (R_p) and the weighted profile R-factor (R_{wp}) and the goodness of fit (χ^2):

$$R_p = \frac{\sum_{i=1}^{n} \left| Y_i^{obs} - Y_i^{calc} \right|}{\sum_{i=1}^{n} Y_i^{obs}}, \qquad R_{wp} = \left[\frac{\sum_{i=1}^{n} w_i \left(Y_i^{obs} - Y_i^{calc} \right)^2}{\sum_{i=1}^{n} w_i \left(Y_i^{obs} \right)^2} \right]^{1/2}, \qquad \chi^2 = \frac{\sum_{i=1}^{n} w_i \left(Y_i^{obs} - Y_i^{calc} \right)^2}{n - p}$$

where: Y_i^{obs} is the observed intensity of the i^{th} data point, Y_i^{calc} is the calculated intensity of the i^{th} data point, w_i is the weighting of the i^{th} data point ($w_i = 1/\sigma_i$), n is the number of data points and p is the number for free least squares parameters. Generally R_p and R_{wp} should be small and χ^2 should be approximately $\chi^2 = 1$.

The physical meaning of the values of the fit parameters depends on the experimental design. Typically a minimum signal to background noise ratio of $Y_i^{obs} \geq 4\sigma_I$ is used to define a diffraction peak. The ratio of background noise to signal scales as a function of collection time squared, meaning to double the signal to noise ration data must be collected for 4-times as long at each point. Intensity resolution needs to be balanced with reasonable experiment time. In order to determine a unique model a sufficient range of *d*-spacings need to be measured as the ratio of data to parameters improves as the measurement range increases. As per the Bragg equation a

shorter incident beam wavelength will also increase the number of *d*-spacings in a given 2θ range. At higher *d*-spacings the diffraction peaks are closer together, especially in the case of complex structures. Peak overlap complicates Rietveld refinement significantly, so an instrument with a small instrumental resolution ($\Delta d/d$) is preferable. Both of these requirements are satisfied in synchrotron radiation experiments. Because of significantly higher energy X-rays that can be generated using a synchrotron source compared to a laboratory source a much higher range of *d*-spacings can be collected. Also, because of the incredible intensity of synchrotron sources, the divergence and monochromaticity of the incident beam can very tightly controlled without sacrificing the signal to noise ration of the data.

1.7.7 Neutron diffraction

Neutron diffraction is in most ways similar to X-ray diffraction and gives the same type of structure information. One important difference is that neutron atomic scattering factors are very different that X-ray atomic scattering factors. Also, neutron atomic scattering factors do not coincide with atomic number. This means that neutron diffraction experiments may be more sensitive to elements that are difficult to distinguish in X-ray diffraction experiments. In this work neutron diffraction was especially useful for examining the anionic structure of metal oxides and oxynitrides as O and N are nearly indistinguishably from each other using X-rays and scatter very poorly compared to the heavier metal cations present in these compounds. It is often possible to co-refine X-ray and neutron diffraction data together to greatly improve the accuracy of the structure model.

Because of the usually lower intensity of neutron beams it is advantageous to collect data with several wavelengths simultaneously using time-of-flight (TOF) techniques. In TOF experiments the entire spectrum can be utilized which can greatly reduce collection times. In a

neutron TOF experiment the angle of the incident beam is constant and the detectors are arranges to cover as much of the Ewald sphere as possible. The sample is exposed to multiple wavelengths at once. Some volume of the sample will lay in a diffraction condition for any given wavelength and the *d*-spacing corresponding to any given neutron scattering event can be calculated from the time from when it is generated to when it is scattered and the time from scattering to when it is detected via:

$$d_{hkl} = \frac{ht_{hkl}}{mL} \cdot \frac{1}{2\sin\theta} = \frac{1}{505.56} \cdot \frac{t_{hkl}}{L\sin\theta}$$

where h is Planck's constant, m is neutron mass, t_{hkl} is the detection time and L is the distance from the source to the detector ($L=L_{\text{source-sample}}+L_{\text{sample-source}}$). Most of the neutron diffraction data and the entirety neutron PDF data used in this work was collected using TOF.

1.7.8 PDF

Pair-distribution function (PDF) analysis is a means of extracting information about a material's local structure from diffraction data by analyzing the inelastic scattering as well as the elastic scattering data. The local structure of complex materials, such as the oxynitrides studied in this work, can be very important to a material's bulk properties. However, because the fundamental assumption of Bragg's law is the periodicity of the samples, standard diffraction techniques are completely insensitive to short-range structure.

X-ray (or neutron) diffraction measures the momentum transfer of a scattered particle (Q) defined as the difference of the initial and scattered wave vector ($k_{initial}$ - k_{final}) and the data collected is the scattered intensity as a function of the wave vector. The total scattering function $S(Q)$ contains intensity contributions from of the Bragg peaks (which give information about the

long-range structure), as well as the scattering not used in typical diffraction analysis such as Rietveld refinement. This includes the elastic diffuse scattering (which gives information from the static local structure) and the ineleastic scattering (which gives information from the atom dynamics). The Fourier transform of $S(Q)$ is the atomic pair density function ($g(r)$):

$$\rho(r) = \rho_0 g(r) = \frac{1}{4\pi N r^2} \sum_{\nu} \sum_{\mu} \delta(r - r_{\nu\mu})$$

where ρ_0 is the average number density of a system of N atoms, δ is the Dirac delta function and the peaks are at distances separating the νth and μth atoms ($r_{\nu\mu} = |r_\nu - r_\mu|$). The function $g(r)$ is the pair distribution function. These functions describe relative atomic position in a sample, crystalline or otherwise. This results in a histogram of all the pairs of atomic distances. Because $|r_\nu - r_\mu|$ is used all directional information is lost so the structure cannot be uniquely determined from $\rho(r)$, but the data does contain much useful information. The position of each peak represents a set of real space distances between atom pairs in the structure. The peaks are Gaussian distributions around the average peak position. The widths of the Gaussians represent the probability distribution of these distances either from thermal displacement or static disorder. The integrated intensity of the peaks in the related function $R(r)$ can be used to determine the scattering intensity of the atoms at each distance $r_{\nu\mu}$ and in some cases the atom types. In simple, one component structures it is easy to determine the structural features that correspond to the peaks just by looking at the PDF, however even for more complex structures it is often possible to get a general idea of the structure over a range of ~2–4 Å. For most materials modeling software is needed to extract meaningful structure information from the PDF. As in other types of diffraction analysis a starting structure model is used to calculate a PDF pattern and parameters are allowed to refine against the data until a satisfactory fit is found.

Two programs were used to model the PDF data. The first was PDFgui[27]. This program calculates the PDF from a model of the smallest unit cell and the distributions of atomic distances are modeled by convoluting the calculated pattern with Gaussians. The other program is RMCprofile[28]. This program defines a large box of atoms (3 times the size of the PDF to be calculated in each direction) to calculate the distribution from the positions of the atoms. The model can be refined using reverse Monte Carlo techniques. As in diffraction experiments, PDF data collected on X-ray and neutron sources can be used to help differentiate between atoms that have similar scattering factors.

1.7.9 Transmission Electron Microscopy

Transmission electron microscopy (TEM) is a technique that uses a high-energy beam of electron to image materials[29]. The resolution of a TEM allows images to me made on the scale of atoms and in this work was used to image cross sections of $LaTiO_2N$ films epitaxially grown on lanthanum titanate substrates. These images were used to inform the models of the film used in fitting the spectroscopic ellipsometry data.

Chapter 2

Substitutional mechanism of Ni into the photoactive semiconductor $InTaO_4$

The mechanism of Ni substitution into the oxide semiconductor $InTaO_4$ has been studied through a combination of structural and spectroscopic techniques, providing insights into its previously reported photoactivity. Magnetic susceptibility and X-ray absorption near-edge spectroscopy (XANES) measurements demonstrate that nickel is divalent within the host lattice. The combined refinement of synchrotron X-ray and neutron powder diffraction data indicates that the product of Ni doping has the stoichiometry of $(In_{1-x}Ni_{2x/3}Ta_{x/3})TaO_4$ with a solubility limit of $x \approx 0.18$, corresponding to 12% Ni on the In site. Single-phase samples were only obtained at synthesis temperatures of 1150 °C or higher due to the sluggish reaction mechanism that is hypothesized to result from small free energy differences between $(In_{1-x}Ni_{2x/3}Ta_{x/3})TaO_4$ compounds with different x values. Un-doped $InTaO_4$ is shown to have an indirect band gap of 3.96 eV, with direct optical transitions becoming allowed at photon energies in excess of 5.1 eV. Very small band gap reductions (less than 0.2 eV) result from Ni doping, and the origin of the yellow color of $(In_{1-x}Ni_{2x/3}Ta_{x/3})TaO_4$ compounds instead results from a weak $^3A_{2g} \rightarrow {}^3T_{1g}$ internal $d \rightarrow d$ transition not associated with the conduction or valence band that is common to oxide compounds with Ni^{2+} in an octahedral environment.

This chapter is adapted from: Malingowski, A.C., et al., Substitutional Mechanism of Ni into the Wide-Band-Gap Semiconductor $InTaO_4$ and Its Implications for Water Splitting Activity in the Wolframite Structure Type. *Inorganic Chemistry*, 2012. **51**(11): p. 6096-6103.[30]

2.1 Introduction

The process of semiconductor water splitting is well known and it has been found that many semiconductor compounds can drive the photoelectrolysis of water by absorbing light in the UV range (>3 eV).[3] This is problematic because UV accounts for only approximately 5% of the light that the Earth receives. Therefore the overall H_2 production efficiency of any UV light utilizing water-splitting semiconductor is substantially handicapped simply because the majority of the solar spectrum is not absorbed. Using a material that could utilize visible light, which accounts for a much larger portion of the solar spectrum (~60%), would be a great step toward developing high efficiency photoactive water-splitting. Unfortunately, visible-light-absorbing semiconductors (band gaps < 3.0 eV) that can drive this water splitting process are quite rare and no materials capable of direct solar water splitting (in the absence of an external bias) with band gaps less than 3.0 eV were discovered in the first 30 years of research in this field.

There was therefore great excitement following the 2001 Nature report by Zou *et al.*[5] that reported for the first time direct water splitting by a medium band-gap semiconductor. The band gap of $InTaO_4$ was reported to be reduced from 2.6 to 2.3 eV when Ni was substituted for In, and aqueous suspensions of powders with formulas $In_{1-x}Ni_xTaO_4$ ($0 < x < 0.15$) were reported to be active in producing both H_2 and O_2 gas when illuminated by light with $\lambda > 420$ nm (2.95 eV) when functionalized with a NiO co-catalyst to aid with H_2 production. However, there were a number of unusual aspects of this report. The stoichiometry of $In_{1-x}Ni_xTaO_4$ assumes a Ni^{3+} oxidation state, which is unexpected for the reported synthesis conditions (1100 °C in air) and was never directly investigated. The maximum activity was found for the $x = 0.10$ sample and not the sample at the reported Ni solubility limit of $x = 0.15$. Finally, the experimentally

determined 2.6 eV band gap of $InTaO_4$ is substantially smaller than that of other tantalates such as Ta_2O_5 (4.6 eV[31]) and $Ca_2Ta_2O_7$ (4.4 eV[32]), perhaps indicating design principles that can be used for designing novel water splitting semiconductors with visible light activity.

It should be noted that the experimentally determined 2.6 eV band gap of $InTaO_4$ was substantially smaller than the 3.5−3.7 eV gaps later obtained from DFT calculations[33-36] despite the fact that DFT methods are known to substantially underestimate the magnitude of semiconductor band gaps.[33-35] On the basis of trial DFT calculations, this discrepancy was suggested[34, 35] to arise from oxygen vacancies within the material, an as-yet experimentally unverified hypothesis. It has also been suggested previously that the true gap of this compound is reflected in the strong absorption feature at 4.3 eV rather than in the much weaker lower energy features[37], a result supported by recent reflection electron energy loss spectroscopy (REELS) studies on $InTaO_4$ films prepared by physical vapor deposition.[38] Given the extensive ongoing interest in this system, we initiated a comprehensive structural and electronic characterization of pristine and Ni-doped $InTaO_4$ with the goal of understanding and reconciling the unusual properties reported for this system.

$InTaO_4$ crystallizes in the wolframite structure type (Figure 2.1) with the monoclinic space group *P2/c* (no. 13).[39] This structure typically forms with an ABO_4 stoichiometry, where the *B*-site cation is an early 4*d*/5*d* transition metal (Nb, Mo, Ta, or W) and the *A*-site is typically a different-sized transition metal or *p*-block cation. It is comprised of hexagonally close-packed oxygens with cations filling one-half of the available octahedral holes. The octahedra formed around the A and B cations form separate infinite edge-sharing "zigzag" chains that run along the *c*-direction. These chains share corners with chains of the other cation type, forming offset layers stacked in the *a*-direction. The wolframite structure type is tolerant of ionic substitution,

and examples of wolframite compounds exist with mixed occupancies on both of the cation sites as well as on the anion site (in fluorinated compounds).[40] The substantially different ionic radii[41] of In^{3+} (0.80 Å) and Ta^{5+} (0.64 Å) can be comfortably accommodated via the distinctly different local environments of the *A* and *B*-site cation positions. However, if the *A*-site and *B*-site cation radii are too close in size, cation disorder occurs and a smaller orthorhombic cell occurs, as is observed for $GaTaO_4$.[39] For Ni-doped $InTaO_4$, the Ni is believed to substitute only on the In site and known to cause a decrease in the length of the unit cell axes when substituted at concentrations up to its solubility limit (15−20% substitution),[42] an effect that is greatest along the *a*-axis, which decreases at about twice the rate of the *b* and *c*-axes.[42] There is substantial variation in the ionic radius of octahedral Ni depending on its valence state and whether it is in the high-spin (HS) or low-spin (LS) state, with tabulated ionic radii[41] of 0.48 (4+, LS), 0.56 (3+, LS), 0.60 (3+, HS), or 0.69 Å (2+). If the Ni cation is smaller than Ta, it might be expected to displace Ta from the *B*-site to the *A*-cation site rather than directly substitute for In on the *A*-site.

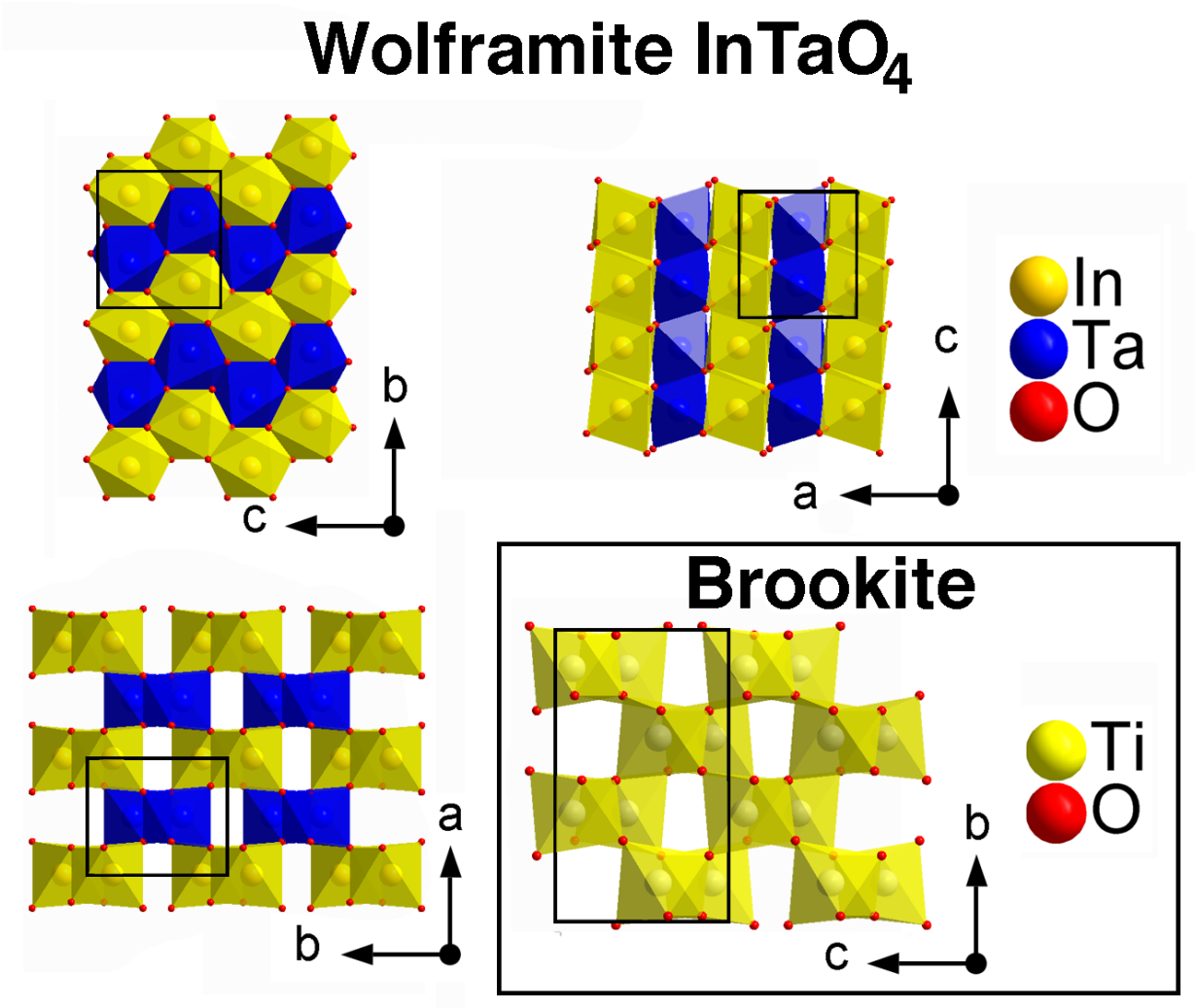

Figure 2.1 Three views of the structure of wolframite-type $InTaO_4$, which contains alternating edge-sharing chains of TaO_6 octahedra (blue) and InO_6 octahedra (gold) that run along the *c*-axis direction. (Inset) Structure of the brookite form of TiO_2. Structures of brookite TiO_2 (*Pnma*, a = 5.16 Å, b = 9.25 Å, c = 5.46 Å, inset) and wolframite $InTaO_4$ (*P2/c*, a = 5.16Å, b = 5.77Å, c = 4.83Å, β = 91.4°) are very similar, and lattice parameters of the brookite (*B*) cell are related to the wolframite (*W*) cell via the relationships $a_B \approx c_W$; $b_B \approx 2a_W$; $c_B \approx b_W$.

The wolframite compound $InTaO_4$ is chemically analogous to brookite, with equimolar amounts of In^{3+} and Ta^{5+} cations present in the place of the Ti^{4+} that is present in brookite-type TiO_2. The wolframite structure is also closely related to that of orthorhombic brookite, which has a similar arrangement of edge-sharing octahedral chains (Figure 2.1, with the relationship between their lattice parameters given in the figure caption). One subtle difference is that the close-packed oxygen layers in the wolframite structure are hexagonally close packed (AB), while

those in the brookite structure have a mixed closed-packed arrangement (ABAC) involving both hexagonal and cubic motifs. This leads to roughly a doubled length of the brookite cell normal to the close-packed oxygen relative to the wolframite cell planes (brookite *b*-axis direction in space group Pbca, and the wolframite *a*-axis direction in space group *P2/c*).

The utility of $InTaO_4$ for visible-light-driven water splitting was initially remarked upon by Zou *et al.* in 2000,[43] where H_2 production was observed at a rate of about 2 μL/h (0.5 g sample, 300 W Xe lamp, 420 nm cutoff filter) using a NiO_x cocatalyst. In follow-up studies, Ni doping of $InTaO_4$ was found to improve H_2 production under the same conditions to values up to ~15 μL/h (quantum yield of ~0.7% at 402 nm), accompanied by approximately stoichiometric O_2 production.[5] Slightly lower activities were observed when a RuO_2 cocatalyst was used instead of NiOx. Other 3*d* dopants than Ni were later found to reduce the visible light activity of this system relative to pure $InTaO_4$, though modest activities for H_2 production from a methanol sacrificial reagent (50−500 μL/h from a 1g sample illuminated by a 400 W Hg lamp) were robustly found in both doped and undoped samples.[44] The water splitting activity of this material was recently revisited by Douiheche *et al.*, who observed mild activity for overall water splitting (up to ~6 μL/h H_2 production but with O_2 production substantially below stoichiometric levels for 0.3 g samples illuminated with a 150 W Hg lamp).[45] Curiously, activity was only observed in the absence of functionalization with a cocatalyst such as NiO_x and Ni doping of $InTaO_4$ was not found to improve the UV response of this system.

2.2 Experimental methods

Three sample sets were prepared with the nominal compositions $In_{1-x}Ni_xTaO_4$ (x = 0.05, 0.10, 0.15, and 0.20), $(In_{1-x}Ni_{2x/3}Ta_{x/3})TaO_4$ (x = 0.025, 0.050, 0.075, 0.10, 0.15, 0.225, and 0.30), and $In_{0.9}Ni_xTaO_4$ (x = 0.05, 0.075, 0.10). Stoichiometric amounts of In_2O_3 (Alfa Aesar,

99.993%), Ta_2O_5 (Alfa Aesar, 99.994%), and NiO (Alfa Aesar, 99.998%) were ground together in an agate mortar and pestle under acetone. The reagents were placed in dense alumina crucibles and reacted at 1150 °C in air with regrinding every 24 h. Each reaction's progress was checked with X-ray powder diffraction on a Bruker D8 Advance laboratory diffractometer (λ = 1.54059 Å) using 12 mm variable slits and a 192-channel Lynx-Eye linear strip detector. When possible, samples were reacted until the X-ray diffraction patterns showed them to be free of In_2O_3 or Ta_2O_5 impurities within the detection limit of the diffractometer, estimated to be less than 1 wt % for this system.

The set of "Ni-deficient" samples with nominal composition $In_{0.9}Ni_xTaO_4$ (x = 0.05, 0.075, 0.10) was specifically prepared for X-ray absorption near-edge structure (XANES) analysis at the Ni K-edge, (8.333 keV), as the low Ni content ensured that the only Ni-containing phase would be Ni-doped $InTaO_4$ even though the exact stoichiometry of this phase was not yet known. Fluorescence data were collected using a Canberra PIPS (passivated implanted planar silicon) detector on beamline X19A (2.1−16.5 keV) at the National Synchrotron Light Source (NSLS) located at Brookhaven National Lab (BNL). X19A is equipped with a Si(111), double-crystal, fixed-exit height monochromator with feedback on the second crystal. The monochromator crystals were detuned to reject harmonics. The beam was collimated by a spherical mirror of Rh-coated glass and focused by a toroidal mirror of Rh-coated glass. Due to the relatively low Ni content and the high absorption coefficient of the host $InTaO_4$ matrix (8.3 μm X-ray absorption length), it was found that the best signal-to-noise could be obtained in fluorescence rather than transmission mode, and therefore, only fluorescence data are presented. Data were processed with the program ATHENA, part of the Horae software package.[46-48]

Standards used for determining the Ni-dopant edge energy were Ni-metal foil, NiO, and

$KNiIO_6$, representing Ni oxidation states of 0, 2+, and 4+, respectively. The Ni foil was provided by beamline X-19A, and the NiO was purchased from Alfa Aesar (99.998% pure). $KNiIO_6$ was prepared using the procedure outlined by Murphy.[49] Powder samples and standards were ground with an agate mortar and pestle and spread over a piece of Scotch tape approximately 1 m long, which was then folded over multiple times and sealed on the edges with more tape. A Ni-metal foil reference was placed in the beam path after the sample and used to calibrate the energies of the absorption data.

Magnetic susceptibility data were collected using the Vibrating Sample Magnetometer option on a Physical Properties Measurement System (PPMS) manufactured by Quantum Design. Powder samples were measured in clear plastic sample holders supplied by Quantum Design for use with the instrument and held in place with clear two-part epoxy. Measurement of an empty sample holder showed a small diamagnetic response that has no appreciable effect on data interpretation. Samples were measured using both zero-field-cooled and field-cooled scans in magnetic fields of 0.1, 1, and 5 T over a temperature range from 300 to 2 K. Data were fit to a modified Curie-Weiss law using the program Igor Pro.[50]

High-resolution X-ray powder diffraction data used in the X-ray/neutron corefinements were taken at the National Synchrotron Light Source (NSLS) beamline X16C. Data was collected using a λ = 0.69755 A over a range of 5−50° 2θ (0.8−8 Å−1 *d*-spacing). X16C uses a parallel-beam setup employing a channel-cut Si(111) monochromator and a Ge(111) analyzer crystal giving $\Delta d/d \approx 2 \times 10{-}4$. The exposure time was increased as the scan progressed to increase counting statistics at low *d*-spacing.

Constant wavelength neutron diffraction data were collected on preliminary $In_{1-x}Ni_xTaO_4$ samples at the BT-1 high-resolution powder diffractometer located at the National Institute of

Standards and Technology. Measurements were taken with a neutron wavelength of 1.54030 Å using a Cu(311) monochromator over a range of 2.5−167° 2θ.

Time-of-flight (TOF) neutron diffraction data were collected on the POWGEN instrument in the Spallation Neutron Source (SNS) located at Oak Ridge National Laboratory (ORNL). Data was collected at a temperature of 300 K using a proton pulse rate of 30 Hz, 1.5 × 1014 protons/pulse. Collection times varied from approximately 8.3 to 5.5 h. Three detector banks were used at 155°, 85°, and 45° with ranges of 12−34 μm, 11−33 μs, and 8−50 μs respectively. The resolution in terms of $\Delta d/d$ is between 0.01 and 0.02 over the measured range of 0.45−4.05 Å.

Diffuse reflectance data were collected on a Perkin-Elmer Lambda 950 Spectrophotometer over a range of 200−1000 nm (1.24−6.20 eV). $BaSO_4$ was used as a 100% reflectance standard. Sample responses in the far-UV range were also checked using larger band-gap Al_2O_3 standard and found to be consistent with the $BaSO_4$ data.

2.3 Results and discussion

In the initial synthesis trials, samples with the nominal stoichiometry $In_{1-x}Ni_xTaO_4$ were heated for 48 h at 1100 °C, a temperature routinely used to prepare these materials. This synthesis method always produced samples that clearly contained In_2O_3 as well as NiO impurities. In addition to these impurities, high-resolution powder diffraction experiments performed on NSLS beamline X16C (Figure 2.2) showed that the wolframite X-ray peaks are split, indicating the presence of two separate wolframite phases with different compositions. The kinetic reasons for this will be discussed later. Increasing the temperature to 1150 °C and increasing the heating time to 72 h produced samples that did not show this peak splitting or In_2O_3 impurities; however, the NiO impurity persisted. All subsequent samples were reacted at

1150 °C until the X-ray diffraction data indicated the reaction was complete (no noticeable split peaks, a stable unit cell size, no change in phase fractions).

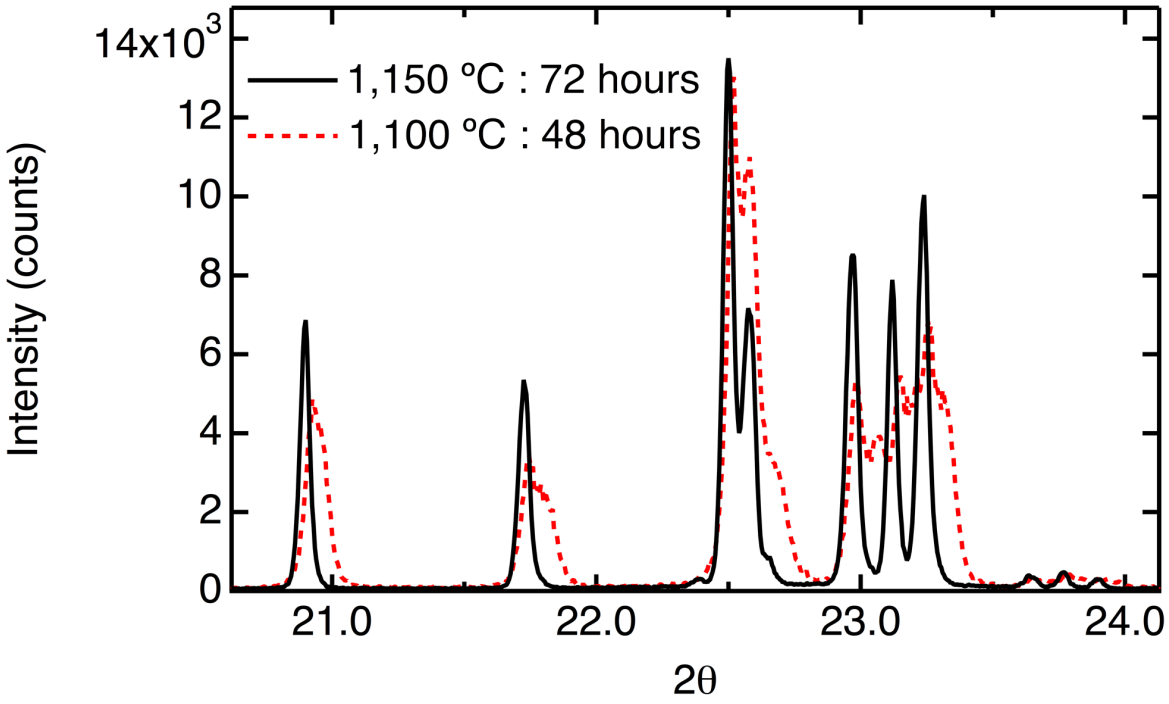

Figure 2.2 Samples of "$In_{0.90}Ni_{0.10}TaO_4$" heated for 48 hrs. at 1100 °C (red, dashed) and 72 h at 1150 °C (solid, black). Peaks of the sample synthesized at 1100 °C are split indicating the presence of two wolframite phases of slightly different composition, a problem that is resolved by heating samples longer and at higher temperatures.

Both synchrotron and lab X-ray diffraction patterns of $In_{1-x}Ni_xTaO_4$ samples show a small but noticeable impurity that can be assigned to the NiO (200) diffraction peak, which persisted even after the wolframite phase appeared to reach equilibrium (Figure 2.3). This NiO impurity phase was much more apparent in the neutron powder diffraction data collected on these samples due to the high neutron cross-section of Ni relative to the other elements present. The presence of NiO in equilibrated samples shows that the true stoichiometry of Ni-doped $InTaO_4$ is Ni deficient relative to $In_{1-x}Ni_xTaO_4$, suggesting that the Ni valence is unlikely to be 3+.

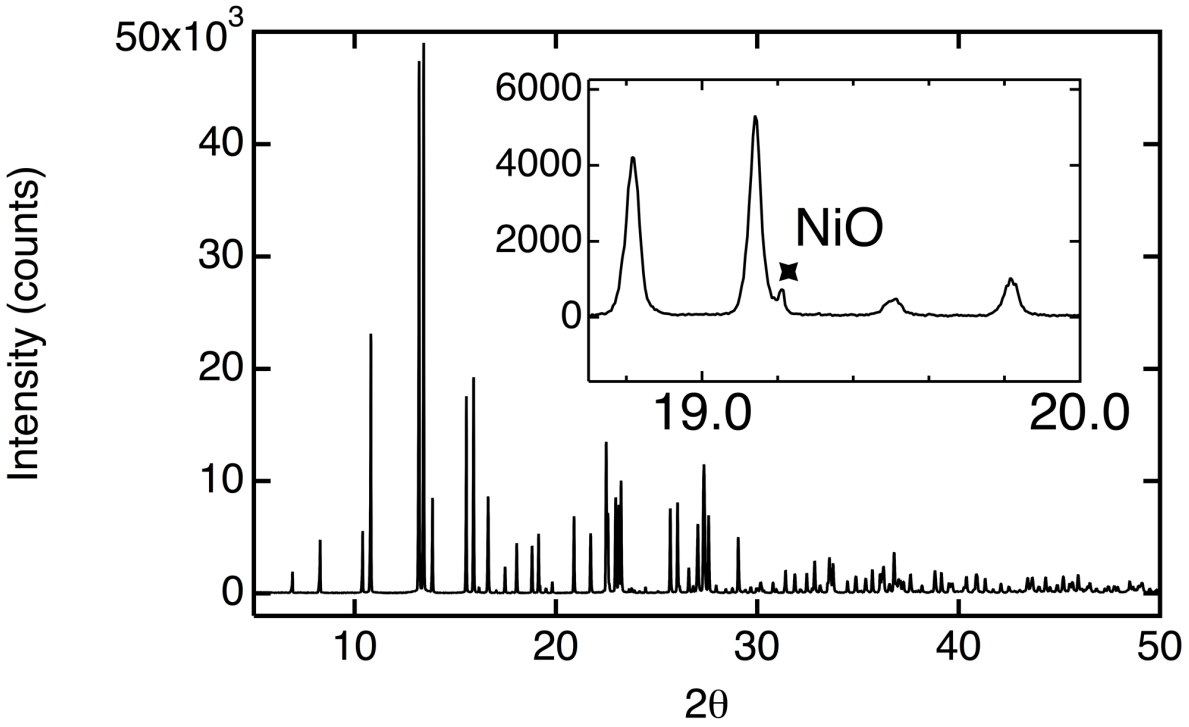

Figure 2.3 Synchrotron X-ray diffraction pattern, collected at NSLS beamline X16C, which results from heating a sample with a nominal stoichiometry of "$In_{0.90}Ni_{0.10}TaO_4$". (Inset) Most visible peak of the NiO impurity phase.

Our first step in determining the correct stoichiometery of Ni-doped $InTaO_4$ was to use X-ray absorption near-edge spectroscopy (XANES) at the Ni K-edge to make a direct measurement of the Ni oxidation state. Although single-phase samples were not available, the element-specific nature of the technique ensures that impurity phases without Ni will not affect the measured X-ray absorption spectrum. For this reason, the stoichiometries of several samples were purposely made Ni deficient (compositions of $In_{0.9}Ni_xTaO_4$ with x = 0.10, 0.075, 0.05) and reacted until powder X-ray diffraction experiments showed that there were no Ni-containing impurity phases that could affect the measured absorption edge energy. Determination of the oxidation state from XANES data was done by comparing the Ni X-ray absorption edge energy of Ni-doped $InTaO_4$ to a series of Ni-containing standards with known oxidation states (Figure 2.4). In all samples, the Ni absorption edge best aligns with the 2+ standard, NiO, indicating that

Ni-doped $InTaO_4$ contains Ni^{2+}.[5]

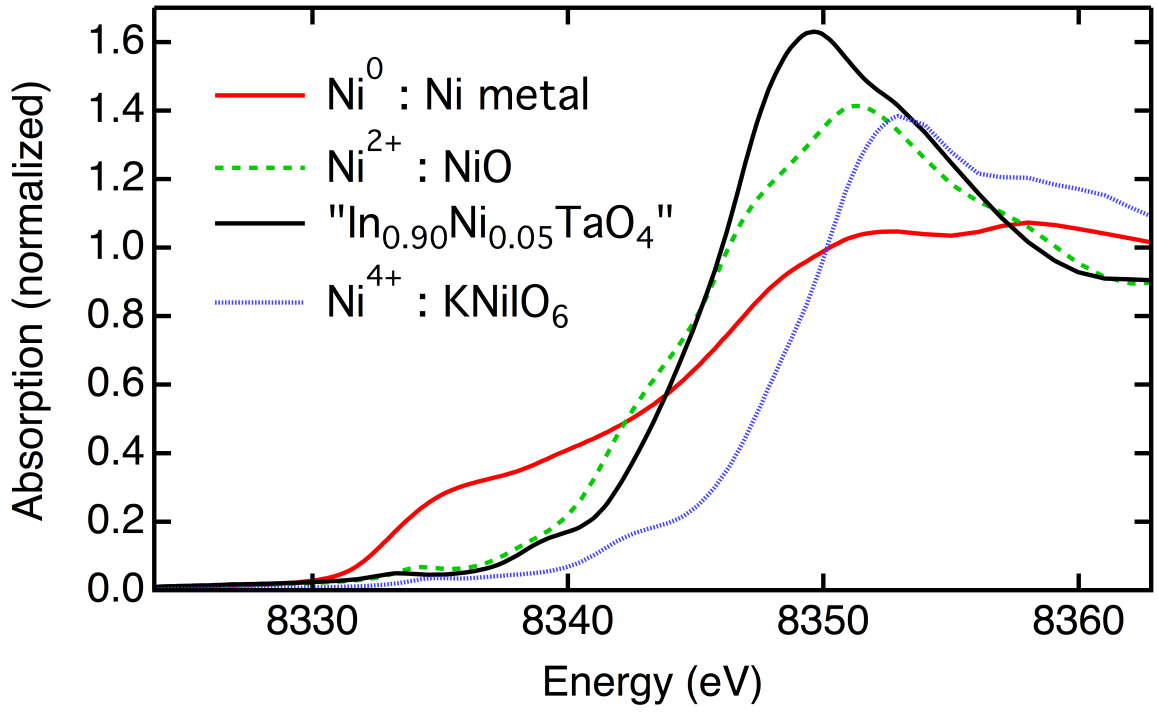

Figure 2.4 XANES data for a sample with the nominal composition $In_{0.90}Ni_{0.05}TaO_4$ reacted at 1150 °C. Sample Ni K-edge energy aligns with that of the NiO standard, demonstrating the presence of Ni^{2+} in Ni-doped $InTaO_4$.

Additional insights into the Ni valence and the distribution of Ni cations within the wolframite structure were obtained from magnetic susceptibility (χ_n) measurements on samples with compositions $(In_{1-x}Ni_{2x/3}Ta_{x/3})TaO_4$ with x = 0, 0.025, and 0.05 (Figure 2.5). Magnetic parameters determined from fits to a modified Curie-Weiss law of $\chi_n = \chi_0 + C/(T - \theta)$ are given in Table 2.1, where χ_n is the magnetic susceptibility, χ_0 is a temperature-independent diamagnetic contribution, C is the Curie constant, T is temperature, and θ is the Weiss constant.[19, 20]

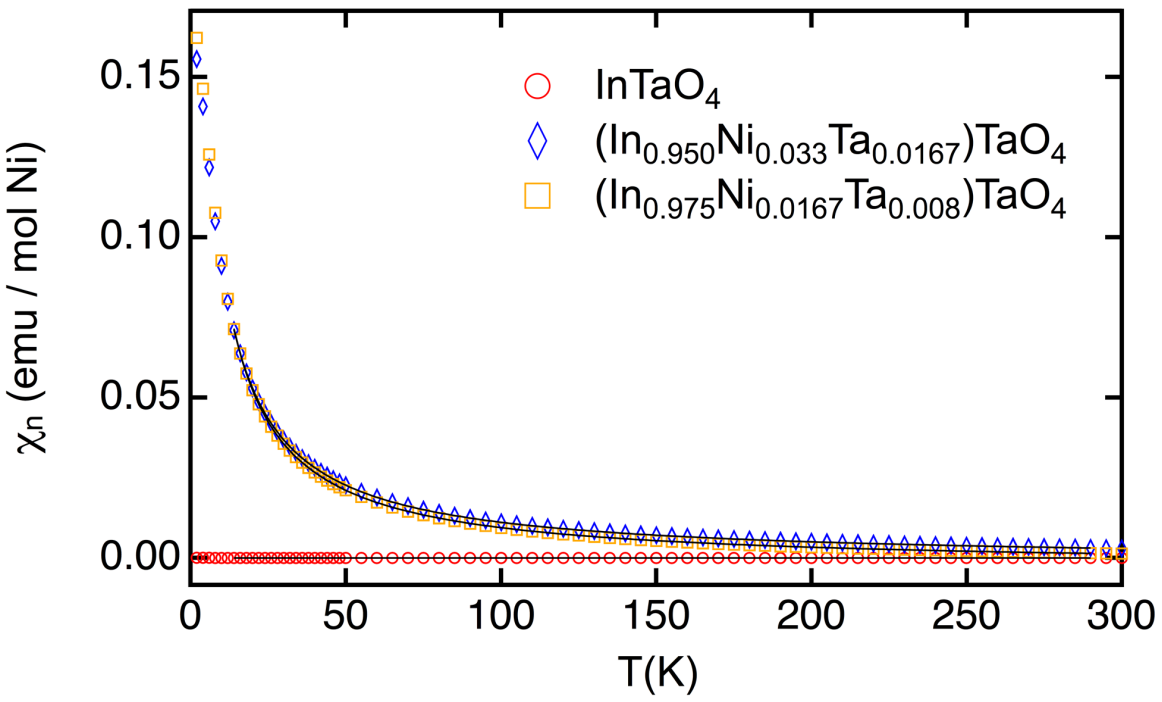

Figure 2.5 Temperature-dependent magnetic susceptibility of $(In_{1-x}Ni_{2x/3}Ta_{x/3})TaO_4$ samples with $x = 0$, 0.025, and 0.05. Curie−Weiss fits to the data are shown in black.

Table 2.1 Experimentally determined modified Curie−Weiss fit constants and resulting effective magnetic moments fit from zero-field-cooled scans

50000 Oe ZFT	θ (K)	C (emu•K•mol^{-1})	μ_{eff} (μ_B)	X_0 (emu•mol^{-1})
$InTaO_4$	-9.2(3)	0.000586(6)	0.068(4)	-0.00004026(8)
$(In_{0.975}Ni_{0.0167}Ta_{0.008})TaO_4$	-3.16(2)	1.278(1)	3.20(7)	-0.00297(1)
$(In_{0.950}Ni_{0.033}Ta_{0.0167})TaO_4$	-3.79(8)	1.289(5)	3.21(1)	-0.001311(4)

Single-phase $InTaO_4$ is essentially nonmagnetic, therefore, confirming that Ni is the only contributor to the paramagnetic susceptibility of Ni-doped $InTaO_4$. The Ni effective magnetic moment (μ_{eff}) is very effective in uniquely discriminating between the different oxidation states and spin states of octahedral Ni cations, as can be seen in Table 2.2. The effective moments fit to $(In_{1-x}Ni_{2x/3}Ta_{x/3})TaO_4$ samples are most consistent with a Ni^{2+} (μ_{eff} = 2.83 μ_B) oxidation state. There are a few possible explanations for the observed excess moment. The very small mole fraction of Ni in these samples makes a precise moment determination challenging. Also, it is not

uncommon to have a Ni^{2+} moment that exceeds the spin-only moment due to incomplete orbital quenching, and the appearance of a feature in the range of 2.9−3.4 μ_B has been previously found to be common among Ni^{2+} species.[51] Finally, Ni is about 0.1 Å smaller than In^{3+} and is not necessarily expected to be found in ideal octahedral coordination, as will be discussed more later.

Table 2.2 Possible spin states of Ni in $InTaO_4$, associated spin number (S), and corresponding values for μ_{eff} calculated from the spin state

State	S	$(4S(S+1))^{1/2}$
Ni^{2+} d^8	1	2.83
Ni^{3+} d^7 low spin	1/2	1.73
Ni^{3+} d^7 high spin	3/2	3.87
Ni^{4+} d^6 low spin	0	0
Ni^{4+} d^6 high spin	2	4.90

Following the results above, it is important to ask the following question: What is the substitutional mechanism of Ni^{2+} for In^{3+} in the wolframite $InTaO_4$ structure? There are two likely routes that could accommodate Ni^{2+} for In^{3+} substitution in the wolframite structure while maintaining overall charge balance. The first possibility is that Ni^{2+} stoichiometrically replaces In^{3+} and that charge balance is maintained through the loss of oxygen, giving an oxygen-deficient formula of $In_{1-x}Ni_xTaO_{4-x/2}$. We can rule out this model due to the consistent observation of a NiO impurity phase present in the X-ray patterns of samples synthesized with this cation stoichiometry. The second route for maintaining charge balance is the co-substitution of Ni^{2+} and Ta^{5+} for In^{3+}, resulting in a stoichiometry of $(In_{1-x}Ni_{2x/3}Ta_{x/3})TaO_4$ and structures that are fully stoichiometric in oxygen. The relationship of these two substitutional models within the context of our proposed In_2O_3-Ta_2O_5-NiO equilibrium phase diagram at 1150 °C (based on the analysis of X-ray patterns for the four sets of stoichiometries synthesized during this work) is illustrated in Figure 2.6.

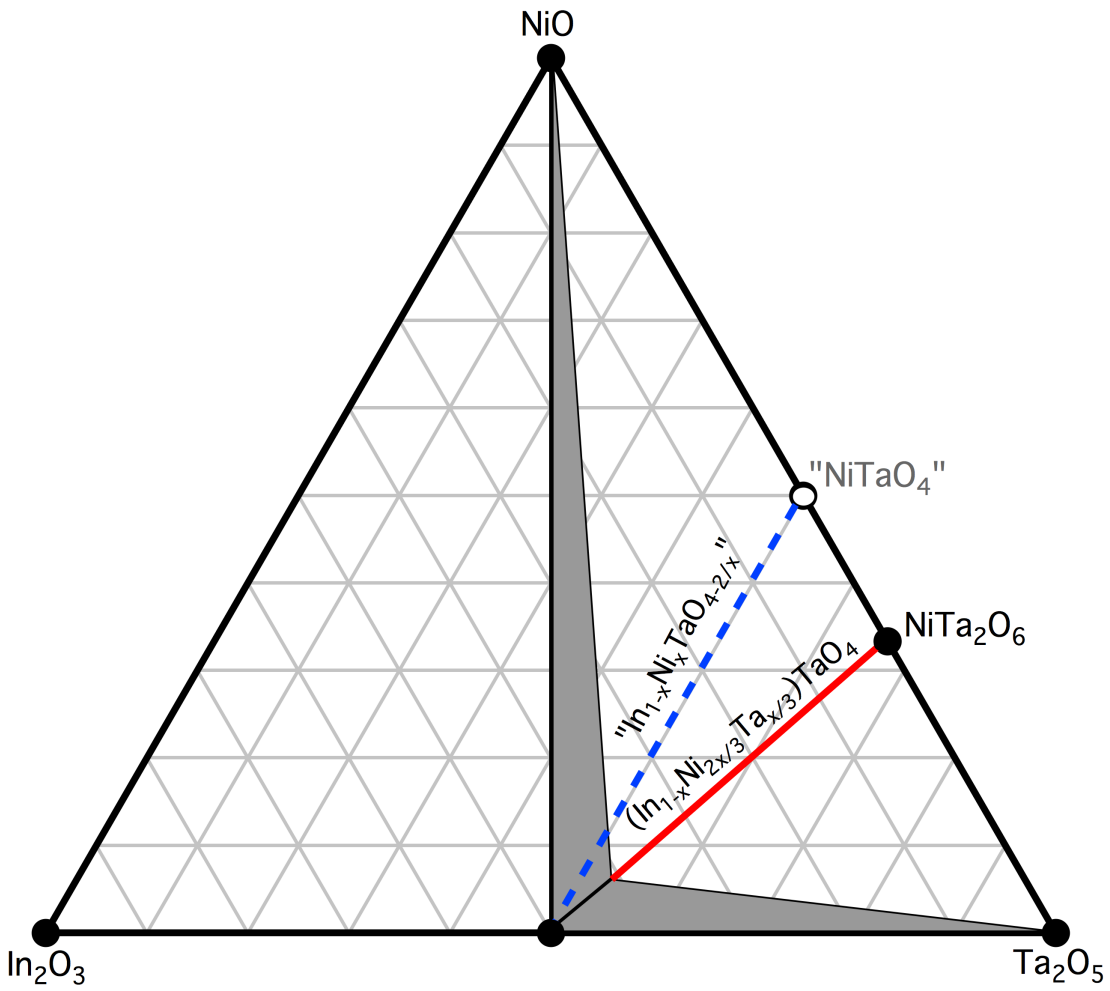

Figure 2.6 Phase diagram of In_2O_3, Ta_2O_5, and NiO at 1150 °C in air. The solid red line marks the $(In_{1-x}Ni_{2x/3}Ta_{x/3})TaO_4$ stoichiometry, and actual solid solution region is highlighted in black. Samples made with the initial composition $In_{1-x}Ni_xTaO_4$ falls on the dashed blue line crossing the NiO−wolframite two-phase region. Only the right half of the phase diagram was directly investigated in this work.

It can be clearly seen that all samples made with the originally proposed composition[5] of $In_{1-x}Ni_xTaO_4$ fall in the NiO-wolframite solid solution two-phase region and will therefore have NiO as the one and only impurity phase. This NiO impurity is quite easy to miss in conventional X-ray diffraction experiments due to the near-perfect peak overlap with the $InTaO_4$ wolframite peaks with the exception of one peak at $d \approx 2.09$ Å that may show up as a peak shoulder. Single-phase samples can be made with the $(In_{1-x}Ni_{2x/3}Ta_{x/3})TaO_4$ stoichiometry until the solubility limit

of Ni is reached; higher x values will result in a two-phase mixture of $NiTa_2O_6$ with maximally doped wolframite, a result we confirmed experimentally using a series of samples with compositions of $(In_{1-x}Ni_{2x/3}Ta_{x/3})TaO_4$ with x = 0.025, 0.050, 0.075, 0.10, 0.15, 0.225, and 0.30. The solubility limit was quantified both by following the lattice parameter variation of these samples (Figure 2.7) obtained through a fundamental parameters Rietveld refinement and by the lever-rule analysis of wolframite/$NiTa_2O_6$ phase fractions of samples beyond the solubility limit. The maximum level of Ni doping at 1150 °C was found to be 12%, corresponding to a value of x = 0.18. It should be noted that extremely long reaction times (greater than 380 h) at 1150 °C were needed to equilibrate to single-phase samples and that incompletely reacted samples had noticeably larger cell volumes than the final products. This might explain the variability in the lattice parameters reported by different groups[42, 45] and suggests that even higher Ni substitution levels could potentially be obtained at higher reaction temperatures. The sluggish kinetics for the equilibration of the solid solution may be related to the phase behavior of this system. $NiTa_2O_6$ rapidly forms along with a Ni-deficient (relative to the starting stoichiometry) wolframite phase as the starting material is consumed. Continued heating causes the $NiTa_2O_6$ impurity phase to diminish, with the shifting mass balance causing the wolframite phase unit cell to shrink as more Ni is incorporated into this phase in a process that is slow due to the relatively low free energy differences involved between wolframite phases with different Ni concentrations.

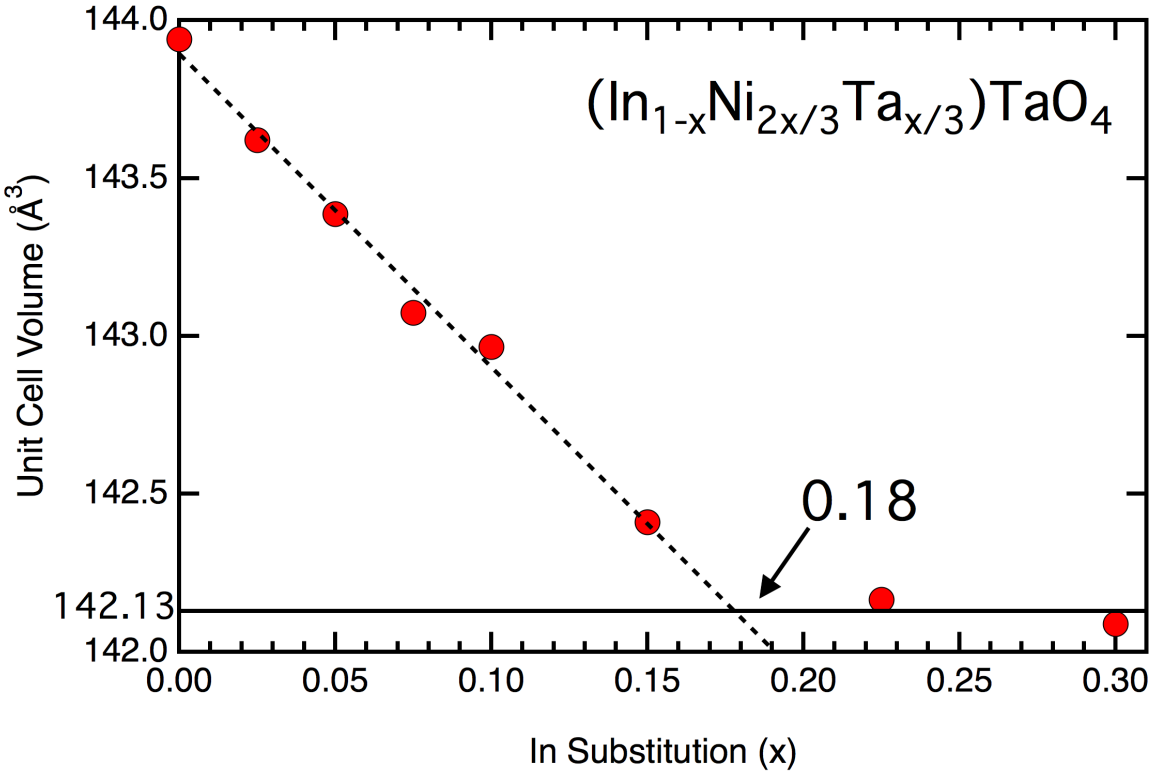

Figure 2.7 Cell volume of $(In_{1-x}Ni_{2x/3}Ta_{x/3})TaO_4$ decreases with increasing Ni content, reaching a minimum volume at about 142.13 Å^3, $x = 0.18$ (dotted line).

Neutron powder diffraction experiments offer the possibility of accurately probing oxygen contents, and tests of the putative $In_{1-x}Ni_xTaO_{4-x/2}$ structural model as well as free refinements of the oxygen occupancies provided no evidence for oxygen vacancies. Combined refinements of the neutron diffraction data and synchrotron X-ray data were carried out to have good sensitivity to species on triply occupied sites suggested by our proposed $(In_{1-x}Ni_{2x/3}Ta_{x/3})TaO_4$ stoichiometry. The large differences in the atomic scattering factors between X-rays and neutrons give two different and complementary pictures of the system that result in a more stable refinement than is possible from analyzing the data sets separately. However, due to the complexity of refining a triply occupied site, refinement of the $(In_{1-x}Ni_{2x/3}Ta_{x/3})TaO_4$ structure still required a variety of restraints to guarantee a valid crystal structure.

First, the stoichiometry of the model was constrained so that charge balance is maintained. Second, the atomic displacement parameters (ADPs) of all the atoms residing on the indium site were constrained to be equal, although this is likely not the case due to the large differences in Ni, In, and Ta radii and masses. The phase fractions and scale factors of the different data sets collected on identical samples were constrained so that the fraction of any phases present were constant among them. Lastly, the X-ray data sets were down-weighted by a factor of 3 to prevent them from dominating the refinements due to their much higher counting statistics relative to the neutron data. Within these constraints, no evidence for oxygen deficiency was found. The final structural model was able to very effectively simultaneously model the X-ray and neutron data sets. The experimentally determined phase fractions and final structural parameters determined from this analysis are tabulated in Table 2.3.

Table 2.3 Final cell parameters and phase fractions for $(In_{1-x}Ni_{2x/3}Ta_{x/3})TaO_4$ determined from X-ray/neutron Rietveld co-refinements

Formula	$InTaO_4$	$(In_{0.95}Ni_{0.033}Ta_{0.017})TaO_4$	$(In_{0.90}Ni_{0.066}Ta_{0.033})TaO_4$
a (Å)	4.830251(2)	4.824528(3)	4.818630(2)
b (Å)	5.775132(2)	5.773787(3)	5.770230(3)
c (Å)	5.157150(1)	5.155303(3)	5.152369(2)
β (°)	91.42510(3)	91.37640(3)	91.3467(4)
Volume (Å^3)	143.8160(1)	143.5640(2)	143.2200(1)
R_p	0.0438	0.0539	0.0556
wR_p	0.0496	0.0532	0.0521
χ^2	0.9172	0.8348	0.9826
NiO impurity (wt%)	-	0.3(2)	0.9(1)

Given the revised composition of the Ni-doped wolframite phase, it was important to revisit the optical properties of this compound as secondary phases can interfere with the measurements of the intrinsic optical response. Diffuse reflectance measurements of $(In_{1-x}Ni_{2x/3}Ta_{x/3})TaO_4$ samples with $x = 0$, 0.025, 0.050, and 0.075 were collected to determine the magnitude and nature of the band gap. The raw reflectance (R) data were converted to units of

relative absorption (α) via a Kubelka−Munk (KM) transform:[52] $\alpha(E) = (1\text{-}R)^2/(2R)$.

For all compositions studied, the absorption spectra have their major feature associated with transitions across the band gap below 300 nm, far from the visible range (Figure 2.8). In the Ni-containing samples there is a much less intense second feature in the visible region, centered at approximately 450 nm (2.8 eV). The intensity of this feature scales as the Ni content increases, but its position and shape do not change (Figure 2.9).

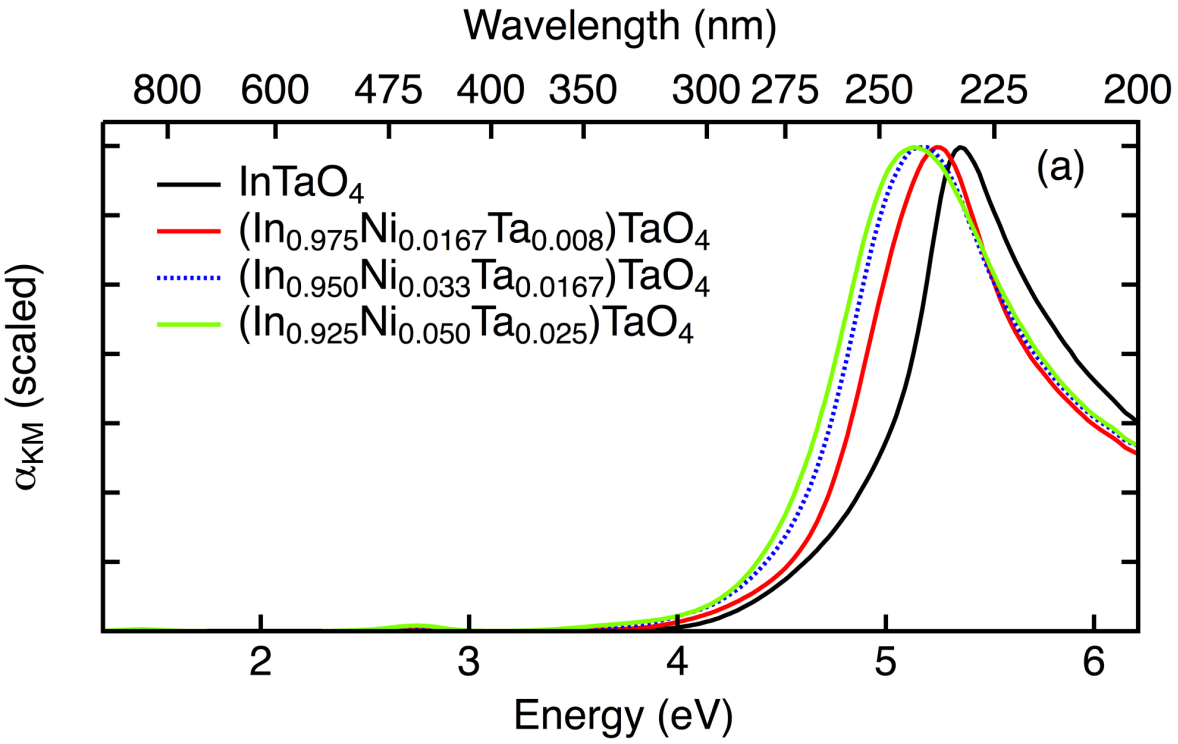

Figure 2.8 Relative absorption calculated via a Kubelka−Munk transform for various *x* values of $(In_{1-x}Ni_{2x/3}Ta_{x/3})TaO_4$. Data shows a small shift in the band edge toward lower energies as the Ni content increases.

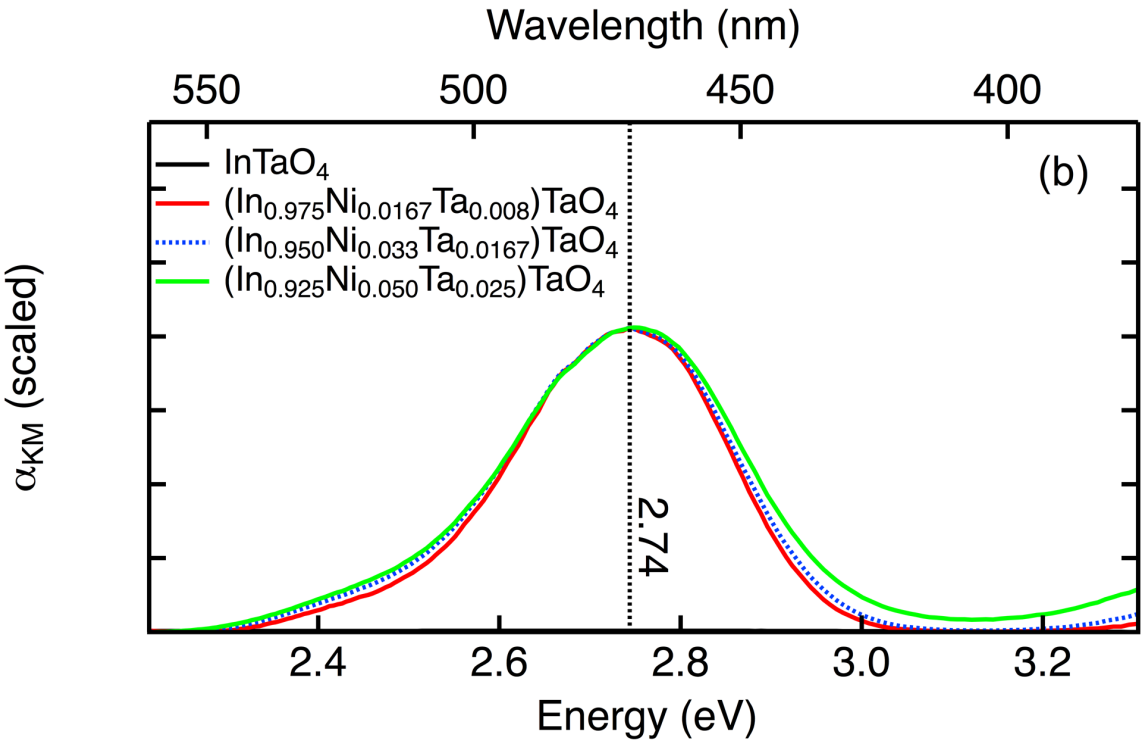

Figure 2.9 Weak absorption feature in the Ni-doped $InTaO_4$ absorption spectrum centered at 2.74 eV (453 nm) is the result of internal $d \rightarrow d$ transitions from the octahedrally coordinated Ni^{2+}.

The magnitudes of the optical band gaps (*E*g) were determined from an analysis of the major absorption feature (Figure 2.8). The slow onset of absorption by wolframite $InTaO_4$ is characteristic of an indirect band-gap semiconductor,[25, 53] a result that quantitative fits confirmed. E_g was determined by fitting the absorption data to the function describing the optical absorption of an indirect band-gap semicondcutor: $\alpha(E) = A^*(E - E_g)^2/E$, where E is the photon energy expressed in eV and A is a constant.[25] The photon energy (E) was included in the denominator of this equation to account for the typical energy dependence of the refractive index (n), though this has a minor influence on the fit results. In the case of pure $InTaO_4$, the indirect band gap was found to be 3.96 eV and the functional form for indirect band-gap absorbance was followed over the energy range of 4.2−4.7 eV (Figure 2.10 and 2.11).

At higher photon energies, the $InTaO_4$ absorbance increased more quickly in a manner

consistent with a direct optical transition with a gap of about 5.1 eV and can be easily visually seen when the data are rescaled (Figure 2.12) to emphasize the scaling of a direct band-gap transition: $\alpha(E) = A^*(E - E_g)^{1/2}/E$.[25] At lower photon energies, including energies below the band gap, the optical response was dominated by an Urbach tail that reflects a broadened distribution of electronic states around the gap energy[25]. The function describing the Urbach tail is $\alpha_{\text{Urbach}}(E) = A^* \exp((E - E_g)k_BT/\sigma)$, where σ is an empirical parameter corresponding to the breadth of the distribution and k_B is the Boltzmann constant. The range where the Urbach response dominates (3.7−4.1 eV) can readily be seen from a plot of the logarithm of absorbance as a function of energy (Figure 2.13).

When the same type of analysis is carried out on Ni-doped samples with compositions of $(In_{1-x}Ni_{2x/3}Ta_{x/3})TaO_4$ with x = 0.025, 0.050, and 0.075, the small influence of Ni on the size of the band gap can be seen (Table 2.4). With increasing Ni doping, the magnitude of the band gap (E_g) slightly decreases from the 3.96 eV of the pristine material by a few tenths of an electronvolt, but it clearly never moves into the visible light energy range. The optical changes are believed to result more from compression of the unit cell volume and broadening of the valence and conduction band rather than from electronic interactions between Ni and In/Ta states. The magnitude of the Urbach broadening (Table 2.4) was substantially larger in the doped samples than in pristine $InTaO_4$ and was generally independent of the amount of Ni.

However, Ni doping does induce a weak absorption peak in the visible regime (2.74 eV, 453 nm) that is not associated with excitations across the band gap. The position of this excitation is essentially independent of doping level, as can be seen when data at doping levels are scaled to match in intensity (Figure 2.9). In a broad study of compounds containing octahedrally coordinated Ni^{2+}, it has previously been observed that there is an absorption feature

at 400 nm range that is the result of a $^3A_{2g} \rightarrow {}^3T_{1g}$ (G) internal $d \rightarrow d$ transition. The weak absorption feature seen in the Ni-doped $InTaO_4$ diffuse reflectance data is almost certainly the result of this local Ni excitation. Prior studies have also observed other internal Ni transitions at energies of approximately 800 and 1100 nm, excitations that were not clearly resolved in our data, probably due to the low concentration of Ni. These types of symmetry-forbidden internal transitions seem poorly suited for driving photochemical reactions such as overall water splitting.

Table 2.4 Indirect band gaps of $(In_{1-x}Ni_{2x/3}Ta_{x/3})TaO_4$ samples

Formula	Band Gap	σ_{urbach}
$InTaO_4$	3.958(3)	0.141(1)
$(In_{0.975}Ni_{0.017}Ta_{0.008})TaO_4$	3.819(9)	0.237(2)
$(In_{0.950}Ni_{0.033}Ta_{0.0017})TaO_4$	3.809(8)	0.310(5)
$(In_{0.925}Ni_{0.050}Ta_{0.025})TaO_4$	3.787(9)	0.308(4)

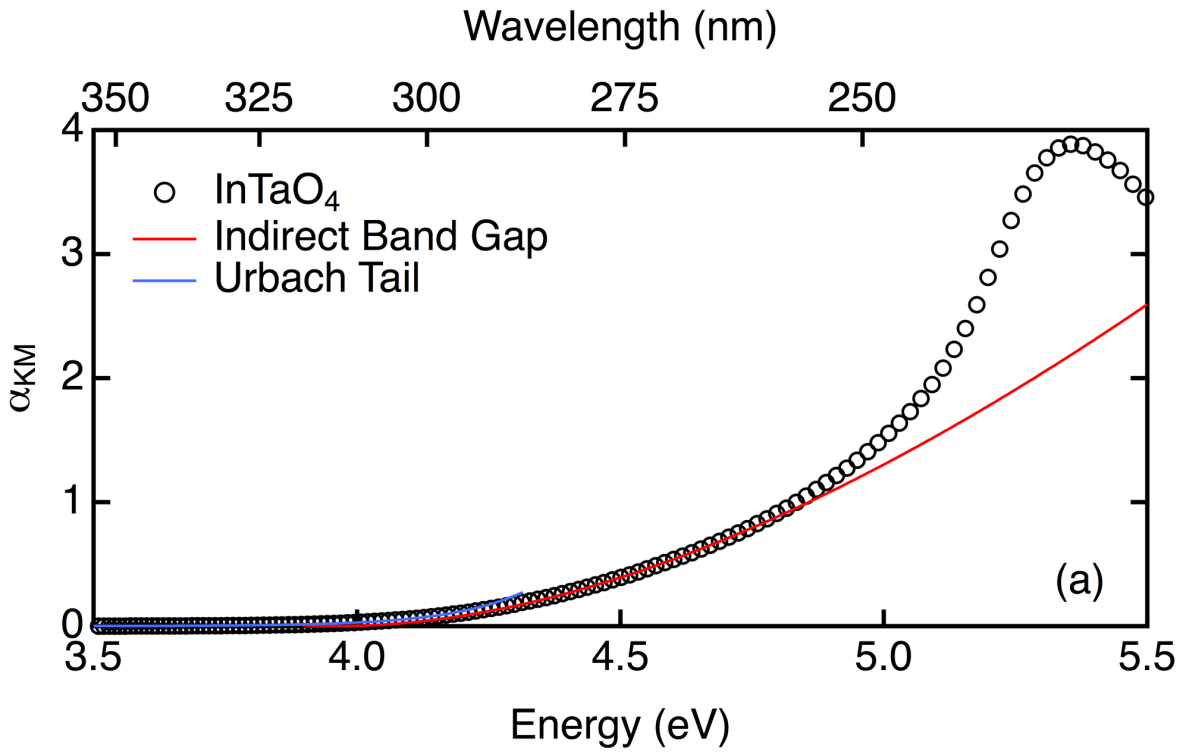

Figure 2.10 Relative absorbance (α_{KM}) of $InTaO_4$ obtained from the Kubleka−Munk transform of diffuse reflectance data with overlaid fits of the fit of the indirect band gap (red) and Urbach tail (blue).

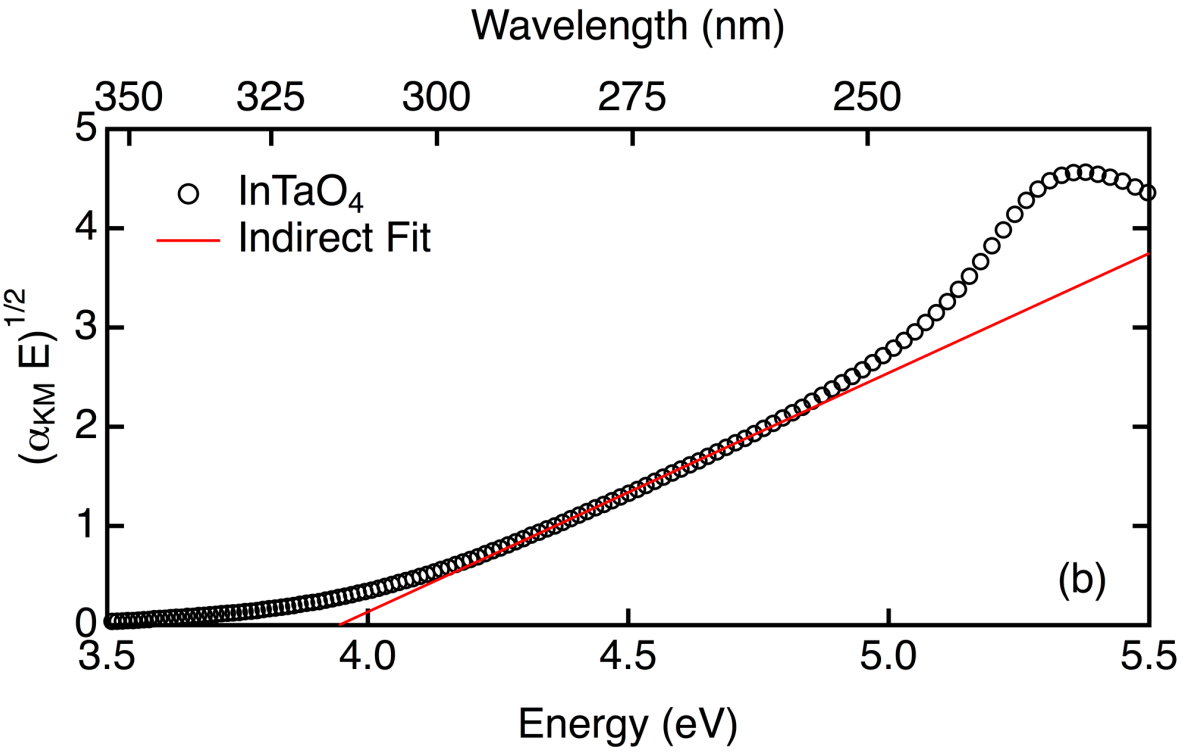

Figure 2.11 Rescaled data is shown to emphasize the regions where the absorbance follows the functional form of an indirect band-gap transition (4.2−4.7 eV).

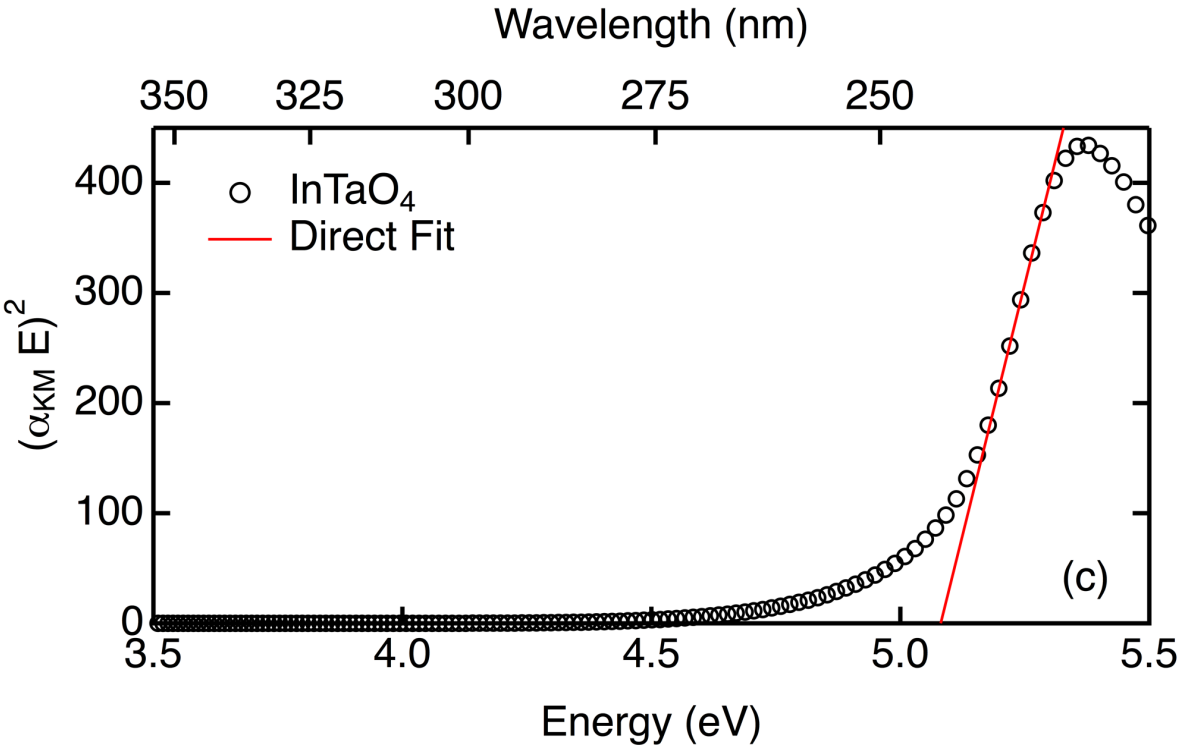

Figure 2.12 Rescaled data is shown to emphasize the regions where the absorbance follows the functional form of a direct band-gap transition (5.2−5.4 eV).

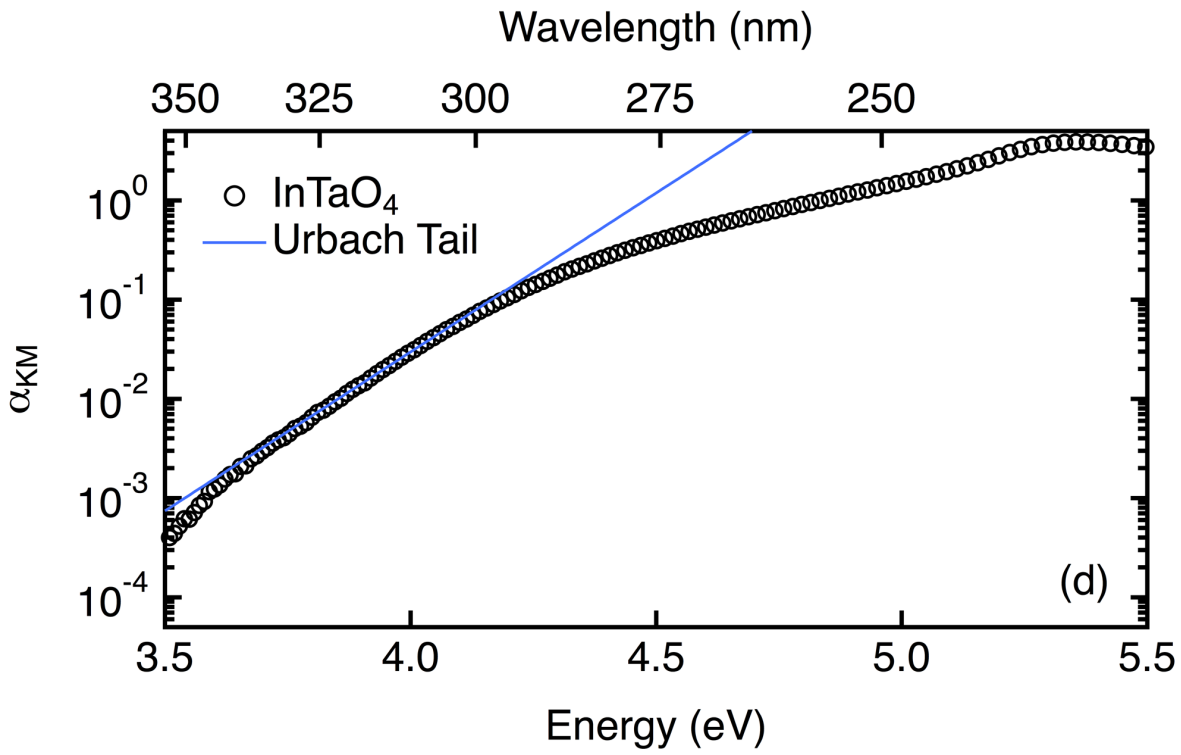

Figure 2.13 Rescaled data is shown to emphasize the regions where the absorbance follows the functional form of an Urbach tail (3.7−4.1 eV).

These studies clearly demonstrate that the previously reported visible light activity for Ni-doped $InTaO_4$ cannot be due to the intrinsic properties of this material, which has an indirect band gap of 3.7−3.9 eV depending on the Ni content. A more likely source of the previously observed activity is a secondary phase. We demonstrated that NiO is a ubiquitous impurity for samples made with an $In_{1-x}Ni_xTaO_4$ stoichiometry and that samples heated at temperatures that are too low or for times that are too short can contain both In_2O_3 and Ta_2O_5 impurities. In particular, In_2O_3 is known to have visible light absorbance (E_g = 2.62 eV) and activity for water splitting reactions[6]. Furthermore, the optical response of In_2O_3 can obscure the local nature of the transition centered at 2.7 eV in Ni-containing samples and has likely lead to the prior incorrect assignment of this feature as being representative of the optical band gap of Ni-doped $InTaO_4$.[5,

42, 54-59

2.4 Conclusions

The synthesis, structure, and properties of Ni-doped $InTaO_4$ have been reinvestigated. XANES and magnetic susceptibility studies show that these phases contain Ni^{2+}, which can substitute for In^{3+} only when charge compensation with Ta^{5+} occurs. The general stoichiometry of these phases is $(In_{1-x}Ni_{2x/3}Ta_{x/3})TaO_4$, with a maximum x value of 0.18, which corresponds to incorporation of 12% Ni on the In position. Pristine $InTaO_4$ is found to be an indirect band-gap semiconductor (3.96 eV), and Ni does not reduce the gap below 3.7 eV. Additional weak optical transitions associated with internal transitions for octahedral Ni^{2+} are observed at 2.74 eV, but these are not likely to be relevant to the photochemistry of this system.

Chapter 3

Light harvesting properties of $LaTiO_2N$ semiconductor films on $La_2Ti_2O_7$ and $La_5Ti_5O_{17}$ single crystal substrates

The optical properties of perovskite $LaTiO_2N$ were determined in a comprehensive study of both powders (diffuse reflectance measurements) and thin films (spectral ellipsometry and transmission measurements), together with those of two single crystal substrates, $La_2Ti_2O_7$ and $La_5Ti_5O_{17}$, which are good substrates for the growth of epitaxial $LaTiO_2N$ films. The major oscillators for $La_2Ti_2O_7$ and $La_5Ti_5O_{17}$ occur at high energies of 4 eV and above. The black $La_5Ti_5O_{17}$ crystals are intrinsically doped by 0.2 electrons per Ti, and exhibit a strong Drude tail at low energies. Stoichiometric $LaTiO_2N$ is found to have a direct optical band gap of 2.25 eV. There is a very rapid onset of absorption above the band gap, leading to very strong visible light absorption coefficients exceeding 10^5 cm^{-1} by 2.45 eV. This exceptionally strong visible light absorption is comparable to that of the simple classic direct semiconductor, GaAs. Oscillators corresponding to excitations out of nitrogen and oxygen valence band states can be clearly distinguished, with the N excitations occurring at energies about 1 eV lower than the corresponding O states. The spectral response is in agreement with that predicted from DFT calculations on model superstructures with partial O/N ordering.

This work is based on a paper submitted for publication.

3.1 Introduction

The position of the conduction band edge in many transition metal oxides is well placed to drive the hydrogen reduction portion photoelectrolysis reaction. The position of the valence band however tends to fall well below the potential needed to oxidize water, resulting in wide band gaps on the order of ~3 eV. Doping onto the cation site may shift the position of the conduction band slightly, but in most cases is unlikely result in a substantial narrowing of the band gap, as was found to be the case for Ni-doped $InTaO_4$. Much greater reduction of the band gap can be obtained by attempting to raise the energy of the valence band by doping onto the anionic lattice. Because of the similarity of properties such as atomic radius, electronegativity, polarizability and coordination, oxygen and nitrogen can often form solid solutions.[10] These compounds, known as oxynitrides, have been shown to be particularly well suited for driving the process of solar photoelectrolysis due to their smaller band gaps and generally more favorable band alignments (relative to the half reactions of water splitting) than their oxide counterparts.

One promising oxynitride system is perovskite-structured $LaTiO_2N$, whose photoactivity was first reported in 2002, when it was shown to be capable of both reducing H^+ to H_2 using methanol as a sacrificial electron donor and of oxidizing H_2O to O_2 in the presence of Ag^+, a sacrificial electron acceptor[13]. Photoactivity was observed using wavelengths as long as 600 nm[13]. The best photoactivty for this system occurs after loading a co-catalyst for water oxidation such as Pt, colloidal IrO_2 or CoO on the surface of $LaTiO_2N$[13, 60-63].

$LaTiO_2N$ is typically synthesized by the nitridation of a powdered lanthanum titanate precursor such as $La_2Ti_2O_7$ under flowing ammonia gas at high temperatures (~950° C). The color of the resulting product may be orange, brown, or red in different preparations, suggesting

that a perfect stoichiometric ratio is not always achieved[64]. Large single crystals of $LaTiO_2N$ have yet to be successfully prepared, and attempts to do so have generally resulted in reduced lanthanum titanium oxides[11, 65]. Crystalline thin films have been prepared by a variety of techniques, including radio frequency (rf) magnetron sputtering[66 61, 67, 68] and by the topotactic nitridation of single crystal $La_2Ti_2O_7$ substrates[61, 65-69]. Electrodes suitable for photoelectrochemical testing require a conductive substrate, and it has been shown that Nb-doped $SrTiO_3$ substrates can be used to prepare $LaTiO_2N$ films which have clearly detectable activity, but low photocurrents. Efforts to improve the performance of these films has been limited by the lack of knowledge of about both the fundamental physical properties of $LaTiO_2N$ (including its absorption spectrum and minority carrier diffusion length), as well as the dearth of knowledge about the influence of defects and non-stoichiometry on these properties.

In this context, films of $LaTiO_2N$ produced by the topotactic conversion of $La_2Ti_2O_7$ single crystals are a good starting point for investigating the fundamental properties of $LaTiO_2N$, as the La:Ti ratio is constrained to be fully stoichiometric (neither La nor Ti is volatile under reaction conditions), with non-stoichiometries in this phase being likely confined to the anion site only. The minimal lattice mismatch and very high crystallinity of these topotactic films should be ideal for photoelectrochemical applications. In practice, the wide band gap $La_2Ti_2O_7$ substrates (E_g ~ 3.8 eV) which have previously been utilized for the preparation of $LaTiO_2N$ films are too insulating to be suitable for this purpose[65, 70]. However, we demonstrate that $LaTiO_2N$ films can also be grown on top of electronically conductive $La_5Ti_5O_{17}$ single crystal substrates, which can make good back electrodes for $LaTiO_2N$ photoelectrodes.

Despite the extensive prior work on $LaTiO_2N$, the optical constants for this film have not been determined. Powders have only been studied by diffuse reflectance measurements [13, 71],

which provide relative and not absolute absorbances. Some transmission measurements have been carried out on thin films [11, 61, 65, 69], but these measurements were not combined with knowledge of film thicknesses and did not probe absolute absorption coefficients. Furthermore, this approach suffers from the difficulty of correcting for both substrate absorbance and interference effects at the substrate/film interface.

An alternative technique for determining the absorbance and optical constants of thin films is spectroscopic ellipsometry (SE). The collection of data at different angles and/or the simultaneous fitting of data of samples with different thicknesses allows the robust determination of optical constants, as well as the simultaneous determination of film thickness[72]. Data can be readily collected on commercial instruments over a wide range of energies from the infrared to ultraviolet (~0.75 - 6 eV), and the data does not suffer from some of the limitations of alternative techniques (saturation of absorbance in diffuse reflectance data, limited dynamic range in transmission data which only span about one order of magnitude in α).

The present work describes the synthesis of epitaxial thin film samples of $LaTiO_2N$ on $La_2Ti_2O_7$ and $La_5Ti_5O_{17}$ substrates. The optical properties of both $LaTiO_2N$ and these two substrates have been determined and validated through comparisons with transmission and diffuse reflectance data. Density functional theory has been used to investigate the partial ordering of anions previously reported for this phase, and to calculate the optical response of $LaTiO_2N$ using appropriate structural models to facilitate the interpretation of experimental data. Finally, the photoelectrochemical characterization of $LaTiO_2N$ films supported on conductive $La_5Ti_5O_{17}$ substrates has been carried out to give insights into the suitability of this semiconductor for solar water splitting driven by visible light.

3.2 Experimental methods

Powder samples of $La_2Ti_2O_7$ were prepared from oxide precursors. Starting materials were La_2O_3 (Alfa Aesar, 99.99%) which was dried overnight at 900° C and stored in a sealed desiccator prior to use, and TiO_2 (rutile, Alfa Aesar, 99.99%), dried overnight at 200° C. Stoichiometric mixtures of the starting materials were ground using a vibratory agate ball mill, placed in dense alumina crucibles (CoorsTek, Inc.) and reacted in air at high temperatures (>1100 °C) until single-phase products were obtained as judged by X-ray powder diffraction. $LaTiO_2N$ powders were prepared by the reaction of single phase lanthanum titanium oxides at 950° C under flowing NH_3 gas (40 mL/min) in a Lindberg/Blue M TF55035A-1 tube furnace within a 1 inch diameter quartz tube for 48-72 hours in typical syntheses. The samples were allowed to cool under flowing ammonia.

Large single crystals of $La_2Ti_2O_7$ and $La_5Ti_5O_{17}$ were grown in an optical floating zone furnace. ($La_5Ti_5O_{17}$ was grown using the Crystal Systems Corporation FZ-T-10000-H-HR-I-VPM-PC). Feed and seed rods of an approximate diameter of 6 mm and a length of 120 mm were prepared by filling a rubber latex balloon with powdered $La_2Ti_2O_7$ and then compressing it in a hydrostatic press, followed by densification at 1200° C in air for 48 hours with the rods resting in a flat tray. $La_2Ti_2O_7$ crystals were grown at a rate of approximately 2 mm/hour with counter-rotating rods (10 rpm) under an atmosphere of Ar (2 atm, 1.21 L/minute flow rate). $La_5Ti_5O_{17}$ crystals were grown at 1.5 mm per hour with counter-rotating rods (10 rpm) under flowing 4% H_2 / 96% Ar, with a 1 hour hold pause after initiating the melt (63.5% power) to allow sufficient time for the reduction of Ti^{4+} in the initial melt. Reaction products were confirmed by both single crystal diffraction studies and powder diffraction studies on ground single crystals, with no evidence for secondary phases. $LaTiO_2N$ films of varying thickness were

grown by treating single crystals of $La_2Ti_2O_7$ or $La_5Ti_5O_{17}$ (cleaved perpendicular to the 110 perovskite layers, or equivalently, the *c** axis) with ammonia gas flowing at a rate of 80 mL/min at a reaction temperature of 950 °C for 1 to 120 min in a Lindberg/Blue M TF55035A-1 tube furnace using a 1 inch diameter quartz tube. The reaction tubes were purged with NH_3 gas before the samples were ramped to reaction temperature and were cooled under NH_3 gas after the reaction time was reached. This synthesis resulted in the formation of red films of $LaTiO_2N$.

X-ray powder diffraction data were collected using a Bruker D8 Advance laboratory diffractometer (λ = 1.54059 Å) equipped with a 192-channel Lynx-Eye linear strip detector and with variable divergence slits set to 12 mm over a 2θ range of 7-140°. Single crystal X-ray diffraction data were collected on an Oxford Gemini A diffractometer fitted with a 135 mm Atlas CCD detector (48 mm pixel size) using a Mo X-ray source (λ = 0.71073 Å). The instrument was equipped with a 4-circle kappa-type goniometer. Data integration, merging, scaling and a face indexed absorption correction were done using the CrysAlis Pro [73] suite, with SIR2011 [74] used for structure solution and SHELXS-97 [75] for structure refinement.

Spectral ellipsometry data for bare substrates ($La_2Ti_2O_7$ and $La_5Ti_5O_{17}$) and for $LaTiO_2N$ films supported on these substrates were collected using a J. A. Woollam M-2000 ellipsometer over a wavelength range of 210-1692 nm (5.90-0.73 eV) with a step size of 1.6 nm below 1000 nm and 3.5 nm above 1000 nm at incident angles of 50, 55, 60, 65, 70, 75 and 80° and a polarizer angle of 45°. The bottom surfaces of the nitrided $La_2Ti_2O_7$ samples were sanded to a coarse finish with 300 grit abrasive paper to suppress backside reflection artifacts in the ellipsometry data[76]. The software package WVASE32 [77] was used to determine optical constants and film thickness by fitting test models to the experimental data. Bare substrates were only measured normal to the *ab* cleavage plane, with the *a*-axis aligned in the plane of the detector.

The same substrate orientation was maintained when $LaTiO_2N$ films were measured on these substrates, avoiding complications caused by the anisotropy of the substrates. For $LaTiO_2N$ films, optical constants were obtained by simultaneously fitting data collected with a 65° incident angle for four films of different thickness over the entire measured wavelength range.

Diffuse reflectance data were collected for vertically mounted powder samples over a range of 200-1000 nm (6.20 - 1.24 eV) using a Perkin-Elmer Lambda 950 spectrophotometer with a 60 mm diameter Spectralon-coated integrating sphere. Powdered samples were placed in a container and packed against a 0.5 inch diameter quartz window to a depth of 5-10 mm. $BaSO_4$ (Alfa Aesar, 97%) was used as a 100% reflectance standard[78, 79]. In case of thin films, the transmission data were collected using the same Perkin Elmer UV-Vis Lambda 950 in 200-1000 nm range. Since a $LaTiO_2N$ film forms on all available crystal surfaces during ammonolysis reactions, the total thickness of the film (top and bottom) was used for the determination of the absorption coefficients, $\alpha(E)$. A cross-sectional specimen for the calibration of thickness using transmission electron microscopy (TEM) was prepared by conventional lift-out technique using a FEI focused ion-beam (FIB) scanning electron microscope. The bright-field TEM analysis was done using a FEI Titan 80/300 microscope operating at 300 kV.

DFT calculations were carried out using the projector augmented wave method[80] as implemented in VASP[81, 82] using the local density approximation for the exchange-correlation functional. The chosen pseudopotentials explicitly include semicore electrons for Ti (3*s* and 3*p*) and for La (5*s* and 5*p*). While the simplest experimental descriptions of $LaTiO_2N$ are in a small unit cell (two formula units, f.u.)[83], these descriptions involve O/N disorder on the anion sites. In order to understand the influence of the anion distribution on the band gap and optical response

of this system, a multiscale approach is required. We defer a complete description to separate publication[84]. The following is an outline of the main steps.

Fundamentally, a sampling of the disorder requires larger superstructures, but on a scale that can still support microscopic calculations. We first performed DFT calculations on a variety of anion configurations within the same 2 formula unit (f.u.) primitive unit cell reported by Clarke[83], but with inversion symmetry removed to reduce the symmetry from *P-1* to *P1*, allowing 6 inequivalent anion sites about each Ti ion rather than the 3 pairs of equivalent sites in each octahedron in the original Clarke model. This database was used to construct and test a real space cluster expansion model of $LaTiO_2N$ for its total energy as a function of anion configuration, based on established techniques and the ATAT package[85-88].

Monte Carlo simulations for this cluster model on a large superlattice as a function of temperature indicated an ordered phase at low temperature and the onset of disorder in the anion sublattice at approximately 200 K. At elevated temperature, near 1100 K, distinguishable site occupancies in the Clarke structure are calculated (oxide fraction from 0.62 to 0.73) that are close to the estimates deduced from the original neutron diffraction[83]. This suggests that lack of anion mobility freezes in the disorder from relatively high temperature. Then Monte Carlo simulations were then run for a smaller superlattice consisting of 16 f.u. $LaTiO_2N$ cells and at 1100 K in order to develop sample structures incorporating anion disorder that could be used for subsequent, detailed study by DFT.

Four snapshots were selected and relaxed based on DFT, with the constraint that unit cells dimensions were fixed to the experimental values to maintain the appropriate anisotropy of this nearly cubic triclinic phase. Full convergence of the electronic structure required a large

planewave cut-off, with a value of E_{cut}=600 eV. The force criterion in the relaxation was 0.02 eV/A. For these structures, the density of states and optical response functions were calculated using the linear tetrahedron method, with a sampling corresponding to 64 *k*-points in the full Brilloiun zone for the 16 f.u. supercell. The influence of lattice relaxation was explicitly tested for some trial structures, but no significant changes were found for the relative energies and optical properties.

Limitations of DFT for treating optical spectra in semiconductors, particularly the systematic underestimation of the band gap, can be addressed directly through many-body perturbation theory (GW and Bethe-Salpeter) methodologies that are computationally demanding, but now well established for optical spectra in a wide range of materials[89]. We have previously utilized these methods for the chemically related compounds of anatase and rutile TiO_2[90]. We used the same methods to assess the influence of nitrogen in the oxynitride under study here by performing calculations on 2 f.u. ordered cells. We find that the corrections to the LDA can be captured by relative shift of the conduction bands (a "scissor operator") with the same magnitude as found for the pure TiO_2 crystals. In addition, based on our earlier detailed studies of TiO_2, strong coupling with phonons may reduce the band gap, an effect not explicitly considered in microscopic calculations to date. In the present study, we take all these factors into consideration and modify the LDA calculated optical absorption using a scissor-operator[91]; this opens the gap by 0.7 eV.

3.3 Results and discussion

3.3.1 Oxide crystal substrate optical properties

Knowledge of the absorption coefficients, $\alpha(E)$, of $LaTiO_2N$ is essential for the rational design of water splitting systems based on this material and for more generally understanding the influence of nitrogen on the optical response of oxynitride semiconductors. Although the optical properties of $LaTiO_2N$ have been measured in numerous prior UV-Vis diffuse reflectance studies, measurements of this type return relative rather than absolute absorbances. We have therefore pursued spectral ellipsometry (SE) studies of epitaxial $LaTiO_2N$ films prepared on lanthanum titanate single crystals in order to obtain information about absolute optical constants and layer thicknesses of these films.

Large single crystals of $La_2Ti_2O_7$ and $La_5Ti_5O_{17}$ were grown in an optical floating zone furnace to serve as substrates for the growth of $LaTiO_2N$. These two compounds consist of slabs of either 4 layers ($La_2Ti_2O_7$) or 5 layers ($La_5Ti_5O_{17}$) of perovskite blocks, and can be readily cleaved perpendicular to the *c*-axis (Fig. 3.1) to give flat surfaces with large areas of 0.25 – 1.0 cm^2. When reacted with flowing ammonia at elevated temperatures (950 °C), orange/red epitaxial films of $LaTiO_2N$ form on the surface of both materials as shown in Fig. 3.1. $LaTiO_2N$ epitaxial films have previously been prepared on top of wide band gap transparent $La_2Ti_2O_7$ single crystals (E_g ~ 3.7 eV). However, conductive black $La_5Ti_5O_{17}$ single crystals have not previously been investigated.

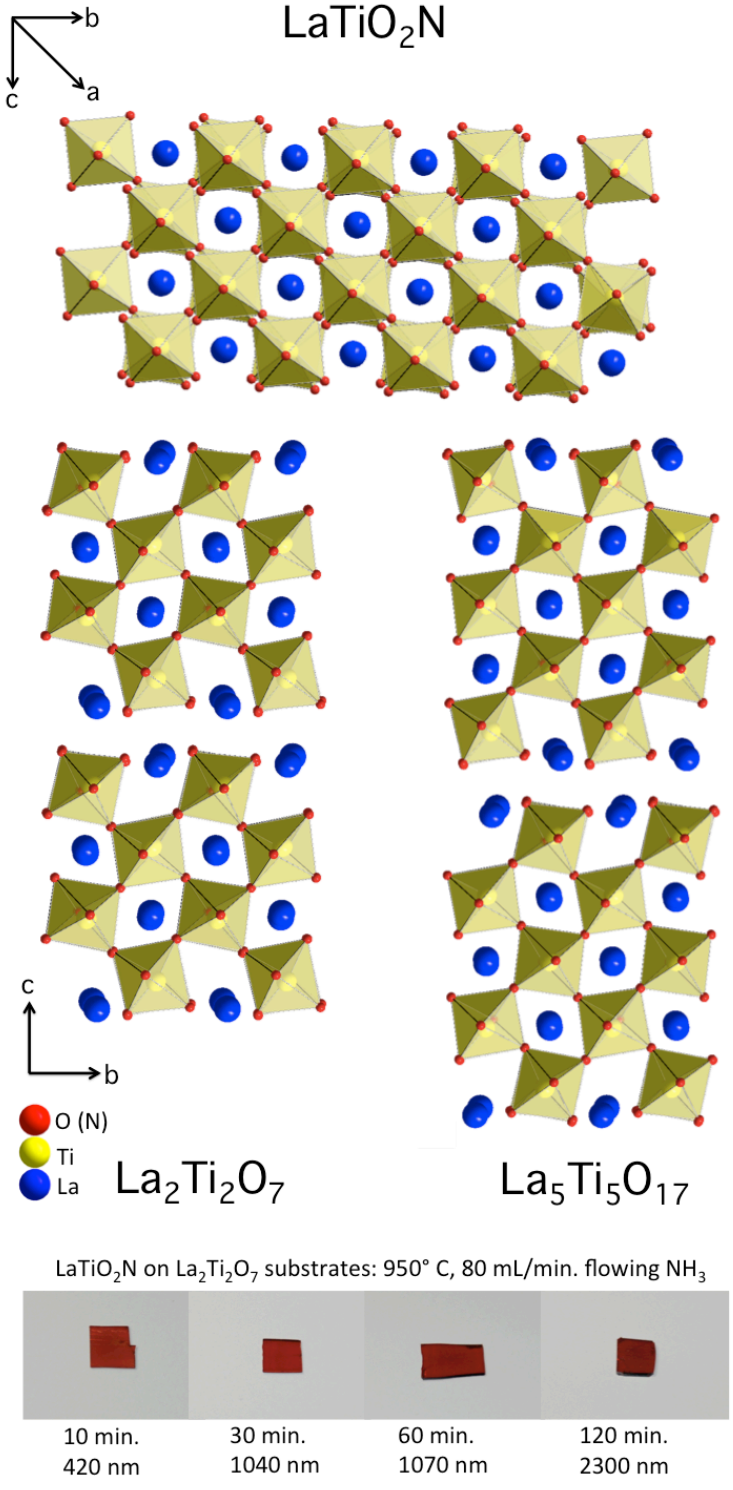

Figure 3.1 The perovskite structure of $LaTiO_2N$ and the perovskite-related crystal structures of the $La_2Ti_2O_7$ and $La_5Ti_5O_{17}$ substrates, shown together with photographs of films resulting from $LaTiO_2N$ growths.

Since the optical coefficients of neither the $LaTiO_2N$ thin film nor its substrates ($La_2Ti_2O_7$ and $La_5Ti_5O_{17}$) are known, it was necessary to characterize the optical properties of the bare substrates before determining the optical properties of the supported $LaTiO_2N$ films, as the net optical response of these samples reflects the properties of both the $LaTiO_2N$ film and its substrate[92, 93]. Since these bare substrates are single-component samples, it is possible to directly estimate their dielectric constants from the raw ellipsometric data (Ψ and Δ, Fig. S3)[94]. The real (ε_1) and imaginary (ε_2) parts of the complex dielectric constant (ε) of both $La_2Ti_2O_7$ and $La_5Ti_5O_{17}$ substrates obtained in this manner have been determined (Figures 3.2 and S2.1-S2.2), and provide sufficient information to move forward in extracting the $LaTiO_2N$ optical properties.

Given that the $La_2Ti_2O_7$ and $La_5Ti_5O_{17}$ structures are closely related to that of $LaTiO_2N$, efforts were made to model the optical response of these systems in order to understand the origin of the optical features within the general class of layered titanates, a family of compounds which have been extensively studied for their water splitting activity. The absolute absorption coefficient, $\alpha(E)$, of the two oxides (Figure. 3.2 top) can be directly calculated[93] from the real and imaginary dielectric coefficients (ε_1 and ε_2) through the equations below:

$$\alpha = \frac{4\pi k}{\lambda}, \text{where } k = \sqrt{\tfrac{1}{2}(\varepsilon_1^2 + \varepsilon_2^2)^{\frac{1}{2}} - \varepsilon_1}$$

Despite their very different colors, the absorption spectra of the two lanthanum titanate samples are quite similar with very strong absorption at energies above 4 eV (310 nm) associated with O $2p \rightarrow$ Ti $3d$ transitions. The black color of $La_5Ti_5O_{17}$ arises from a Drude tail associated with the free carriers in this compound. Very weak visible light absorption is observed for $La_2Ti_2O_7$ single crystals, which are pale orange in color, presumably due to weakly absorbing color centers

whose origin could be structural defects or low levels (<1%) of impurities such as Fe, as previously suggested[65].

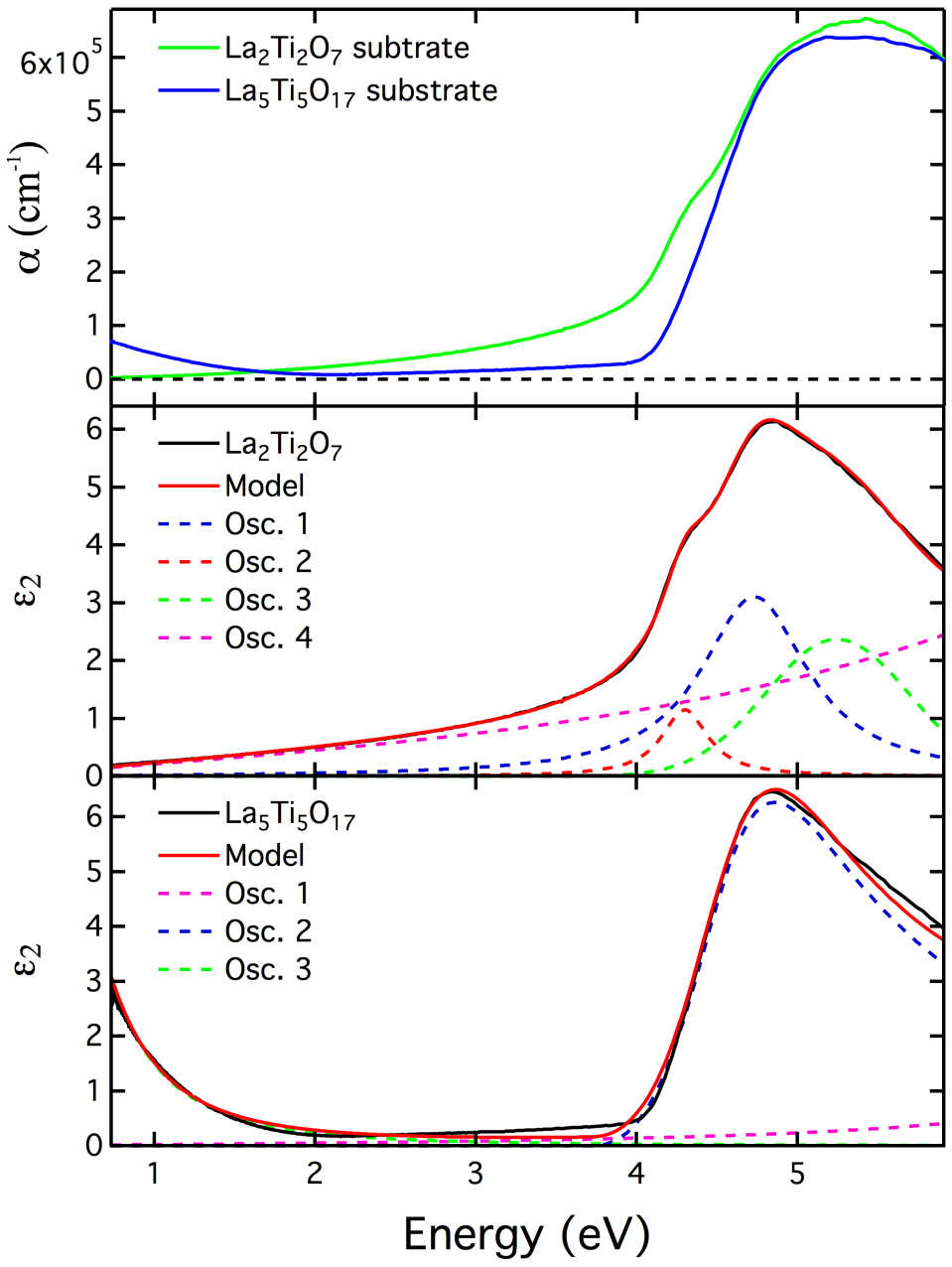

Figure 3.2 Top: Absorption (α) of $La_2Ti_2O_7$ (green) and $La_5Ti_5O_{17}$ (blue) obtained from spectral ellipsometry data collected at a 65° incident angle and a 45° polarizer angle. Measured (black) and modeled (red) imaginary dielectric coefficients (ε_2) of $La_2Ti_2O_7$ (center) and $La_5Ti_5O_{17}$ (bottom) are shown together with the contributions of the different oscillators (dashed lines) used to model the data.

The strong optical response above 4 eV associated with the band gap of $La_2Ti_2O_7$ was modeled as a total of three Lorentz oscillators and one Gaussian oscillator centered above the band gap energy (Fig. 3.2, Table 3.1).[92] These oscillators are associated with O $2p \rightarrow$ Ti $3d$ transitions, which for the present compounds give rise to a band gap 0.5 – 0.75 eV higher in energy than corresponding 3D titanate analogues such as TiO_2 (3.0 eV for rutile[95]; 3.2 eV for anatase[96]) and $SrTiO_3$ (3.1 eV)[71] due to the band narrowing associated with the two dimensional structure of $La_2Ti_2O_7$. The high-energy response of $La_5Ti_5O_{17}$ (Figure 3.2) shows fewer features and can for the most part be modeled with a single Tauc-Lorentz (TL) oscillator, perhaps reflecting the higher symmetry of the layers within this phase. The close homology of the dielectric response of $La_5Ti_5O_{17}$ to that of $La_2Ti_2O_7$ again reflects the influence of dimensionality in shaping the optical response.

3.3.2 $LaTiO_2N$ film optical properties

The determination of the full optical constants of $LaTiO_2N$ using composite samples of $LaTiO_2N/La_2Ti_2O_7$ and $LaTiO_2N/La_5Ti_5O_{17}$ becomes possible once the substrate optical constants have been resolved. The composite samples have a complex optical response that includes interference fringes at energies where the incident photons are weakly absorbed by the film and are therefore able to interact with both the substrate and film before reaching the detector. As can be seen for $LaTiO_2N/La_2Ti_2O_7$ composites (Figure 3.3), the periodicity of the oscillations in the interference fringes increases with increasing film thickness, allowing the film thickness to be very precisely quantified (Table 3.2), though a correction involving adjustment of the film density appears necessary to obtain accurate results, as will be discussed more later. Since these fringes occur when light is incompletely absorbed, ellipsometry studies are unable to effectively probe weak absorption at energies near or below the band gap in thin films. A

comparison of samples of different thickness shows that the onset threshold for oscillations varies from 2.5 eV for the thinnest sample (420 nm) to 1.9 eV for the thickest sample (2300 nm).

The optical response of $LaTiO_2N$ was modeled using a simultaneous fit to data collected for samples of four different thicknesses of $La_2Ti_2O_7$-supported $LaTiO_2N$ films, with the results summarized in Table 3.1. The combined fit is justified by the close similarity of the pseudodielectric constant ε_2 extracted for these composite samples. For the thickest sample, only the data above the band edge (2.5 eV) was fit. This is because of apparent extra absorption near the band edge that may correspond to a different surface roughness effect or a different strength of absorption from a conductive Drude surface layer. The optical response from 2-6 eV could be modeled with three slightly asymmetric Tauc-Lorenz oscillators with energies of 2.49, 3.49, and 5.43 eV. These transitions are ascribed to optical transitions of N $2p \rightarrow$Ti $3d$ t_{2g}, O $2p \rightarrow$ Ti $3d$ t_{2g}, and N 2p $\rightarrow$ Ti 3d e_g orbital states, respectively. From this data, it is possible to clearly resolve the contributions from the two different anions in the structure, and to see that the states associated with N^{3-} are integrated into a broad, well-defined band which has an intensity comparable to that associated with the O states when the differences in concentration and energy are accounted for. It is not known how well dilute N ions within an oxide lattice (such as those in $TiO_{2-x}N_{2x/3}$) will maintain this coherence, but this is a testable hypothesis if solid solution films of oxide and oxynitride analogues such as $(LaTiO_2N)_{1-x}(CaTiO_3)_x$ are prepared and studied by the techniques that we have demonstrated.

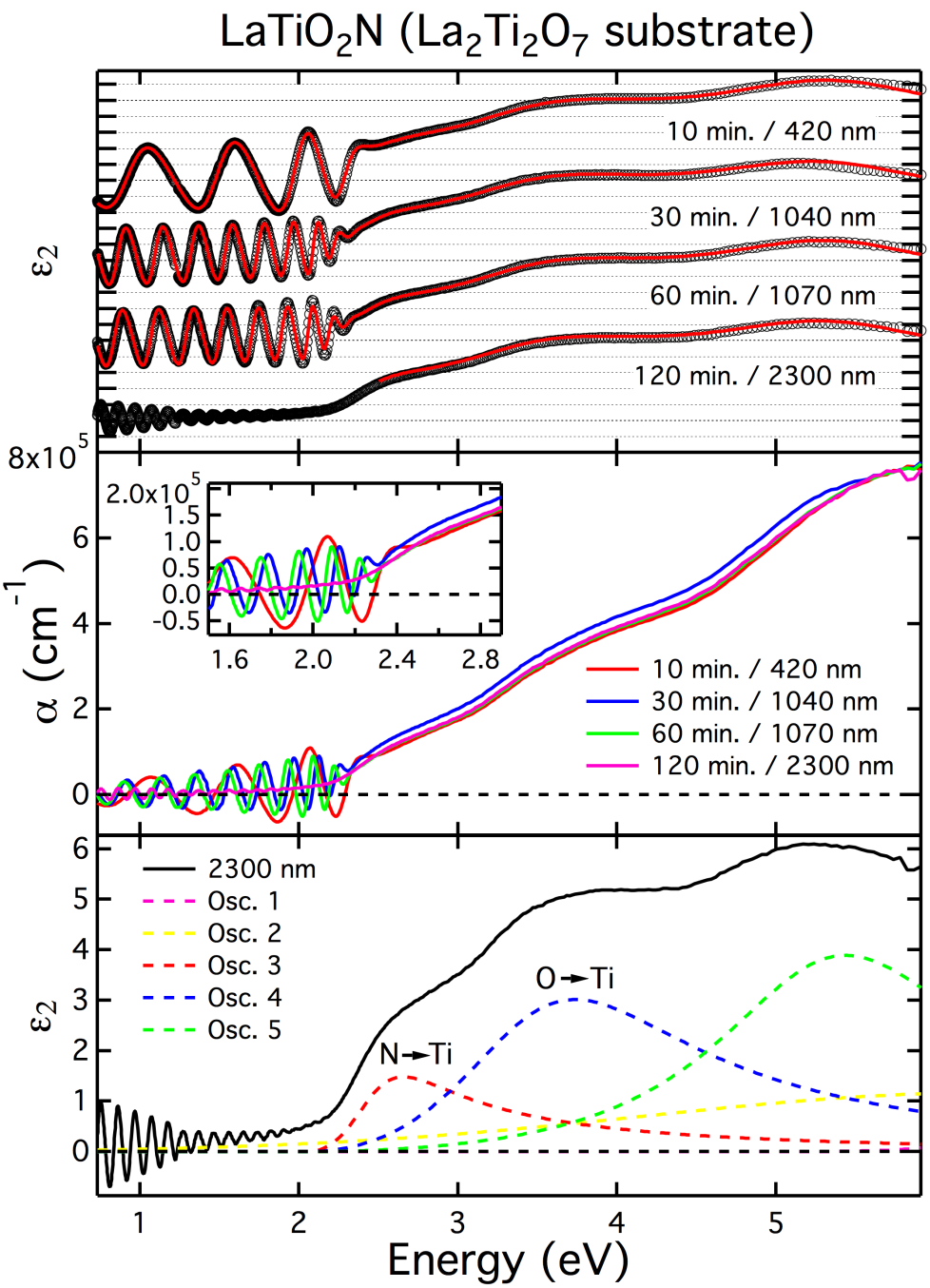

Figure 3.3 Top: Comparison of the pseudodielectric constant ε_2 for different thickness $LaTiO_2N$ films grown on $La_2Ti_2O_7$ substrates at 950° C for 10-120 min. Data are shown in black, and the model obtained by global fitting of these films in red. Center: Overlay of absorption coefficients calculated from the pseudodielectric constants of these same four films. Inset highlights the visible light regime. Bottom: Oscillators used to model the optical response of $LaTiO_2N$ and the orbital assignment of visible light absorption transitions. These oscillators have been rescaled by a factor of 0.65 to compensate for the effective medium approximation used in the model.

While it was initially anticipated that the $LaTiO_2N/La_2Ti_2O_7$ samples could be described using a two-layer model, TEM experiments indicated a higher degree of sample complexity. Film thicknesses calculated from SE data based on a simple two-layer model were only 64% of the thickness directly measured in TEM measurements. This inconsistency could be attributed in real density or compositional variations in the sample. The $LaTiO_2N$ layer was therefore modeled using a Bruggeman effective medium approximation (EMA) with 35% void space[77, 92, 97]. Two other unexpected features were observed in the TEM experiments: an amorphous surface layer with a width of 1 – 30 nm thick, depending on the cooling protocol, and a 2 – 5 nm thick interfacial layer at the $LaTiO_2N/La_2Ti_2O_7$ interface corresponding to lamellar intergrowths of the oxide and oxynitride phases. These features will be described in more detail elsewhere[98]. Since it was observed from XPS measurements that the surface of $LaTiO_2N$films is reduced[98], a surface Drude layer[77, 92] , detailed in Table 3.1, in the SE model was tested and found to substantially decrease the intensity of the oscillation fringes associated with the film thickness, thus improving the fits. The thin interfacial layer was not included in the final model, as its inclusion did not result in substantial improvements to the fit. The final co-refinements used to determine the $LaTiO_2N$ optical coefficients from the 65° incident angle data therefore included three layers: (1) a surface Drude layer with identical parameters other than its thickness, which was allowed to refine independently for each sample, (2) a 64% dense $LaTiO_2N$ layer with common optical properties but variable thicknesses for the four samples, and (3) an infinitely thick substrate of $La_2Ti_2O_7$.

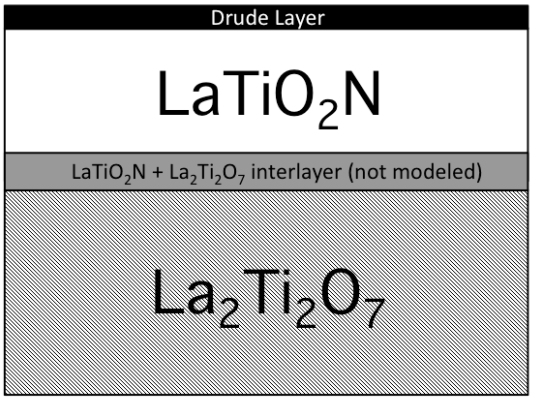

Figure 3.4 A Schematic representation of the model used to fit the optical properties of $LaTiO_2N/La_2Ti_2O_7$ samples.

Table 3.1 Oscillators used to fit ε_1 and ε_2 of $LaTiO_2N$ on $La_2Ti_2O_7$ (950 °C, 80 mL/min. NH_3)

Amorphous Surface Layers

Nitridation Time (min.)	Thickness (Å)	Drude Oscillator Parameters	
10	3.36(6)	N ($1/cm^3$)	$1.5811x10^{22}$
30	7.71(7)	μ	0.38(2)
60	4.20(7)	m*	1 (fixed)
120	4.64(9)	ρ (Ω•cm)	0.0010341
		τ (fs)	0.21705

$LaTiO_2N$ Film on $La_2Ti_2O_7$ Substrate Oscillator Parameters

Type	Amplitude	Center (eV)	Broadening (eV)	Gap (eV)
TL	62(2)	2.456(4)	0.66(2)	2.05
TL	82(4)	3.57(1)	2.06(7)	2.05
TL	40(7)	5.29(4)	1.8(1)	2.05
Gaussian	0.41(3)	2.7(1)	2.0(1)	N/A
Gaussian	22(2)	7.94(6)	2.4(3)	N/A

$La_2Ti_2O_7$ Substrate Oscillator Parameters

Type	Amplitude	Center (eV)	Broadening (eV)
Lorentz	5.23(2)	9.27(3)	5.63(4)
Lorentz	3.10(5)	4.749(3)	0.81(1)
Lorentz	1.15(3)	4.304(3)	0.35(1)
Gaussian	2.37(2)	5.246(8)	1.05(2)

Table 3.2 Substrate reaction time (950° C, 80 mL/min NH_3) and resulting film thickness by ellipsometry / TEM

Time (min.)	Thickness (Å) -SE (w/ and w/o correction)	Thickness (Å) -TEM	Substrate
10	2722	4187(2)	N/A	$La_2Ti_2O_7$
30	6756	10394(4)	N/A	$La_2Ti_2O_7$
60	6928	10659(4)	6600	$La_2Ti_2O_7$
120	14903	22927(5)	N/A	$La_2Ti_2O_7$
60	8960	13790(20)	N/A	$La_5Ti_5O_{17}$

The absolute $LaTiO_2N$ absorption coefficient, $\alpha(E)$, can be readily determined from the spectral ellipsometry data, and is found to be remarkably high. In addition to having a small band gap of about 2.25 eV, $LaTiO_2N$ has a very rapid onset of absorption leading to an absorption coefficient of 10^5 cm^{-1} at energies only 0.2 eV above the band gap. This corresponds to an optical depth of 100 nm, suggesting that films of twice that thickness can completely harvest visible light for electrochemical applications. This very strong visible light absorption at these energies is comparable in magnitude to that of GaAs, a classic direct band gap semiconductor with a much simpler crystal structure[99].

In order to confirm the unusually strong absorption coefficients observed for $LaTiO_2N$ thin films, transmission measurements were also performed. Although spectral ellipsometry is a very sensitive technique, this sensitivity makes it potentially less robust in determining absorption coefficients than the classical technique of transmission measurements that are far less sensitive to surface roughness and other sample inhomogeneities. One limitation of transmission measurements is the small range of absorption coefficients than can be measured, as instruments that can effectively measure intensities over four orders of magnitude can only sample one order of magnitude in absorption coefficient due to the exponential decay of transmission with increasing absorption coefficient. Transmission measurements were therefore

carried out on three $LaTiO_2N/La_2Ti_2O_7$ samples of different thickness in order to broaden the energy range over which $\alpha(E)$ could be determined. It can be seen that when the raw transmission data (Figure. S2.14) are corrected for surface reflectance and are normalized to the film thickness, the absorption coefficients for the films directly overlay with those measured by spectral ellipsometry (Figure 3.5 and S2.15). Furthermore, the relative absorbance data obtained through diffuse reflectance measurements on powders of orange $LaTiO_2N$ ($LaTiO_2N$-O) are also in complete agreement with the spectral ellipsometry results after adjustment by a multiplicative factor of 10^4, which corresponds to $1/s$, where s is the scattering factor in the Kubleka-Munk transform. As can be seen from the data overlay, the diffuse reflectance data both offer the best sensitivity to the weakly absorbing regime below the band gap and offer the greatest dynamic range, though it should be noted that the diffuse reflectance response of this sample in our instrument does saturate by an absorption of $\alpha/s = 13$, corresponding to an energy of 3.6 eV. The optical data from these three methods are therefore fully in agreement, and confirm that $LaTiO_2N$ has exceptionally strong visible light absorption.

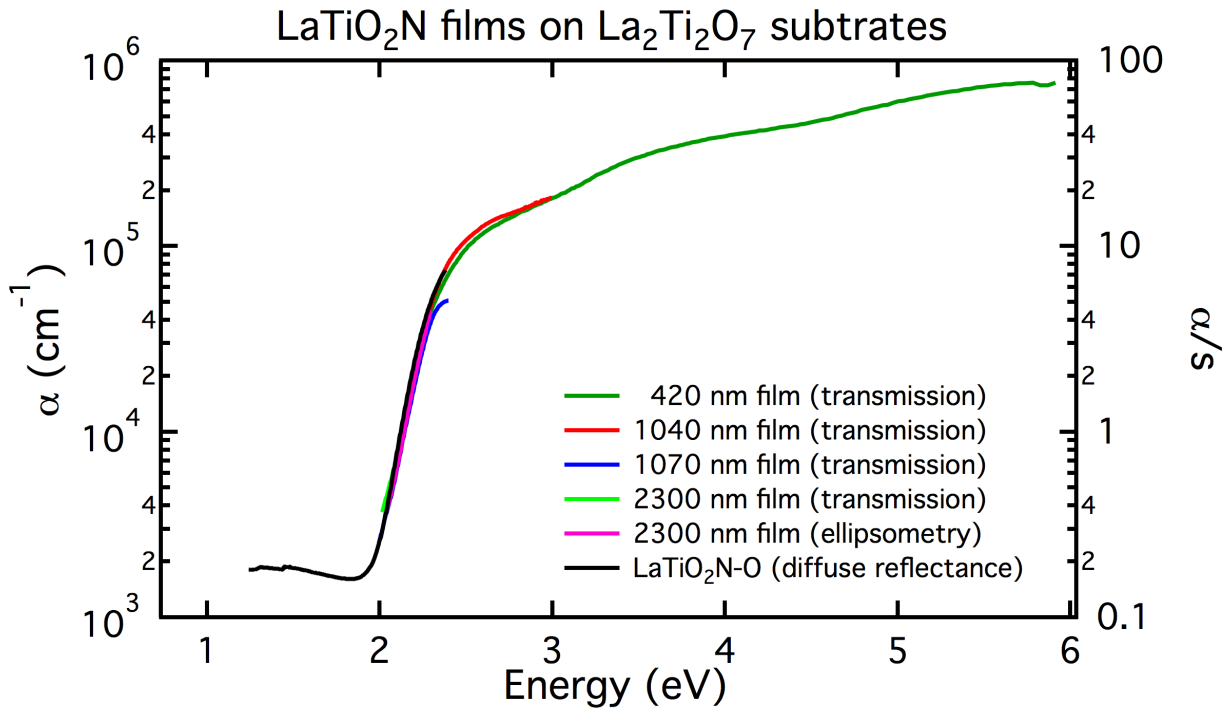

Figure 3.5 Absorption spectra of $LaTiO_2N$ powder measured by diffuse reflectance (right axis) and $LaTiO_2N$ films grown by nitriding $La_2Ti_2O_7$ for 10, 30 and 60 minutes (data collected by transmission, left axis) and ellipsometry measurements of the film made by nitriding for 60 minutes (left axis) give a consistent and comprehensive picture of the absorption characteristics of $LaTiO_2N$ when assembled together.

3.3.3 $LaTiO_2N$ optical properties by DFT

The origin of the unusually strong visible light absorption in $LaTiO_2N$ is not known. It is speculated that the presence of polar building blocks, (namely TiO_4N_2 octahedra with nitrogen anions in a *cis* configuration) rather than more symmetric TiO_6 or TiN_6 environments, enhances the dipole that can be stimulated in optical transitions, and results in stronger absorption in this mixed-anion framework than in related homogenous oxide or nitride analogues. Density functional theory (DFT) calculations were therefore utilized to better understand the influence of structural motifs on the electronic and optical properties of $LaTiO_2N$. As discussed in the methods section, we explicitly model the role of anion disorder with a multiscale approach.

The simplest starting point for understanding the structure of $LaTiO_2N$ is the anion-disordered unit cell determined from synchrotron and time-of-flight neutron diffraction data[83]. The Z=2 primitive unit cell associated with this structure is the simplest cell that can be used to generate trial structures when treated in the *P1* space group. DFT calculations were performed for all possible O/N distributions around a central Ti atom. The lowest energy arrangements of TiO_4N_2 octahedra were those in which the two N anions were arranged in a *cis* configuration. Those in a *trans* configuration were at least 0.1 eV per f.u. higher in energy. Long range ordered crystal structures were analyzed in which every octahedron was stoichiometric (TiO_4N_2) with a *cis* configuration. So long as the N-N sides of the octahedral are aligned, the energy is essentially indistinguishable.

Based on our Monte Carlo simulations for the cluster expansion model at higher temperature (above 200 K), fluctuations readily form and the degree of long-range order is substantially reduced. Such configurations always include local octahedra with one and three N atoms, in addition to those that are stoichiometric. At typical synthesis temperatures for this system, the Monte Carlo simulations show anion site preferences for the three different anion sites that were identified in the original experimental structure determination, in accord with the occupancies obtained from this neutron diffraction experiment[83]. This suggests an intuitively reasonable result: anion mobility in oxides generally freezes out at sufficiently high temperatures (~700 K) to prevent the development of full, long range anion ordering. Therefore disordered superstructures represent the most appropriate structures for comparison with experimental data. Four different Z = 16 Monte Carlo snapshots were generated at 1000 K and then subsequently relaxed through DFT calculations as described in the methods section. Overall, the O:N ratio was fixed at the ideal stoichiometric ratio of 2:1. The excess energy above the DFT results for the

fully ordered ground state structures ranges from 0.016 to 0.060 eV/f.u., fully consistent with sampling at 1000 K. Further details of these structures are given in appendix 2. Since the density of states and optical response did not vary significantly, we show results from one configuration here. Among the 16 Ti octahedra in this structure (Figure 3.6), there are four octahedra with 1 N atom and four octahedra with 3 N atoms, with the remaining octahedra having the ideal environment with 2 N atoms. Simple chemical intuition is in accord with the partial density of states projected on atomic sites (Figure 3.6). The lowest energy empty conduction band states are dominated by the Ti *d*-states. Near top of the valence band, the most prevalent contributions are from N *p*-states but there is a crossover about 1.5 eV lower in energy to predominant O *p*-states, with the relative energies of N and O states reflecting the lower electronegativity of N. Both anions contribute throughout the valence band, suggesting a high degree of hybridization that may be conducive to the effective transport of minority carriers (holes) within these delocalized states.

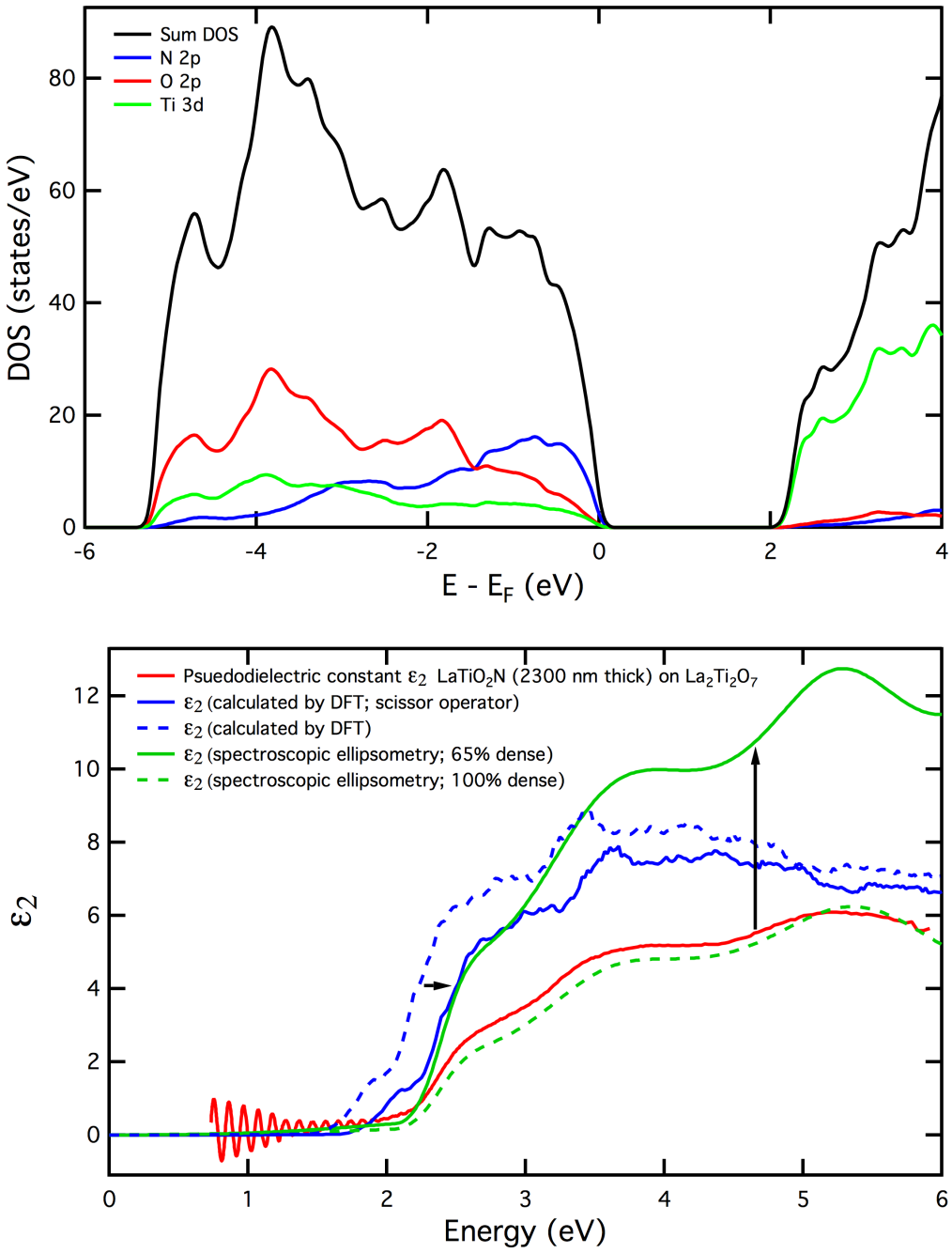

Figure 3.6 Density of states (top) and optical properties (bottom) of a 16 f.u. $LaTiO_2N$ superstructure (inset) constructed with Monte Carlo methods. The projected densities of states are colored as follows: total (black), Ti-*d* (green), O-p (red), N-*p* (blue). Bottom: Trace of the ε_2 tensor as calculated (blue), the trace of the ε_2 tensor shifted by +0.2 eV using scissor operator, ε_2 collected by spectroscopic ellipsometry (solid red, 2300 nm film), sum of the modelled oscillators (dashed green) and the sum of the oscillators of the $LaTiO_2N$ film component used in effective media approximation fit model. (green dashes).

The optical response, $\varepsilon_2(\omega)$, calculated for this superstructure using the LDA approach shows a robust onset near 1.6 eV. This is only slightly larger than the minimum calculated band gap for this structure of 1.47 eV. As noted in the methods section, for Fig. 3.6 and discussion below, we include a rigid, 0.7 eV shift of the conduction bands to account for the estimated error in the LDA band gap. Despite the disorder in the structure, there are three broad features evident in the response function. The lowest energy feature, peaking near 2 eV must come from the N-*p* to Ti-*d* transitions. The second feature, roughly 1 eV higher in energy derives from the O-*p* states that dominate more deeply in the valence band. The third feature near 4 eV likely comes from several sources, including N *p* to higher lying Ti *d* states, as well as the increasing strength of the O *p* states deeper in the valence band. Absorption at each wavelength can be determined from the real and imaginary components of the complex dielectric constant as described above.

3.3.4 Photoelectrochemical activity of $LaTiO_2N$ films

Conductive $La_5Ti_5O_{17}$ substrates can serve a back-electrode for $LaTiO_2N$ devices, allowing the suitability of $LaTiO_2N$ for visible light driven water splitting to be evaluated using an architecture that is suitable for technological applications. The activity of $LaTiO_2N/La_5Ti_5O_{17}$ for water oxidation under simulated solar illumination (AM 1.5) was tested as a function of applied bias (Figure 3.7, top). The observed photocurrent of about 70 mA/cm^2 at 1 V *vs.* Ag/AgCl, with a very large difference between the light and dark current indicate that $LaTiO_2N$ films have modest activity for water oxidation, in accord with prior results on films prepared by other methods[61]. While large photocurrents cannot be obtained without substantial optimization that is beyond the scope of the present report, the excellent performance of $LaTiO_2N$ as a visible light absorber can be clearly seen from this preliminary data.

Importantly, the photocurrent of the $LaTiO_2N$ film does not substantially change when ultraviolet photons are filtered out (blue curve) from the original simulated solar illumination (red curve) using a 400 nm cutoff filter, indicating that the majority of the photoresponse of this material is generate by photons within the visible light spectrum, in contrast to many other semiconductor systems being considered for solar water splitting applications. This can be seen more quantitatively in the photocurrent action spectrum (Figure 3.7), which shows that the photocurrents can be measured all the way out to the band gap of 2.25 eV (~550 nm) when measurements are carried out under a strong positive bias. The external quantum efficiency (EQE) for water oxidation under these conditions is about 20% in the ultraviolet and 5% in the visible portions of the spectrum, with good stability observed during chronoamperometry measurements (inset). This is superb performance for an unoptimized film whose estimated thickness of 2 microns is about ten times larger than the optical depth of light at these wavelengths and a variety of strategies to further improve the performance of this system are currently being investigated.

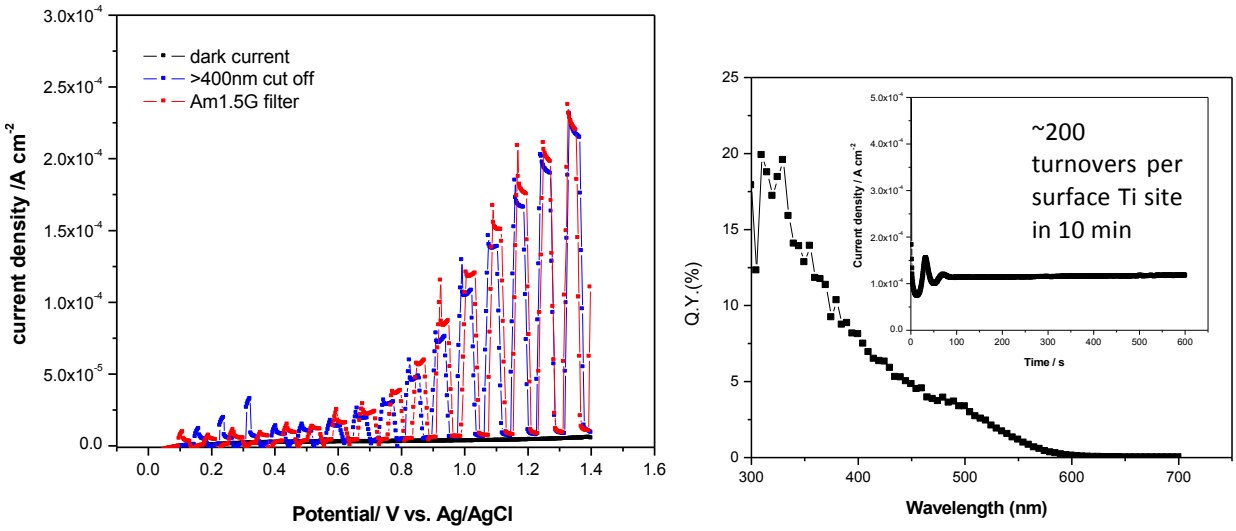

Figure 3.7 Photoelectrochemical activity of $LaTiO_2N/La_5Ti_5O_{17}$ electrode measured as a function of applied bias (right), photon energy (left), and time (inset).

3.4 Conclusions

These results unambiguously demonstrate that $LaTiO_2N$ is a very promising next-generation photoanode for solar water splitting due to a relatively small band gap (2.25 eV, relative to 2.45 eV for $BiVO_4$ or 2.7 eV for WO_3), a sharp onset of extremely strong light absorption just above the band gap, and sufficiently facile charge carrier transport to enable the observation of photocurrents even in the absence of functionalization with a water oxidation co-catalyst. The unexpected observation of exceptionally strong visible light absorption of $LaTiO_2N$ is comparable in strength to that of the classic direct band gap semiconductor GaAs. This is hypothesized to be related to the highly asymmetric octahedral environment of Ti, and suggests that similarly strong absorption may be generally found in other mixed anion semiconductors. Oxynitride perovskites therefore represent a promising pathway to achieving 10% solar-to-fuel efficiencies.

Chapter 4

The structure and light absorption properties of $LaTiO_2N$ variants

4.1 Introduction

Powdered $LaTiO_2N$ is synthesized by heating a powdered lanthanum titanium oxide precursor material under flowing ammonia gas. The color of the resulting oxynitride can vary from bright orange to red to brown depending on the phase of the lanthanum oxide starting material used. Regardless of the lanthanum oxide precursor used however, the nominal formula of the resulting oxynitride is the same. The reason for the variety of color is unknown.

In this work three samples of the nominal composition $LaTiO_2N$ was synthesized using one of three starting materials with different La:Ti ratios: $La_2Ti_2O_7$, La_2TiO_5, or $La_4Ti_3O_{12}$ Attempts were made to establish a connection between the structures and compositions of the different colored samples and their light absorption properties. The light absorption of the resulting oxynitrides was determined from diffuse reflectance measurements. Oxygen and nitrogen contents were determined using thermogravimetric analysis and structures were examined using X-ray and neutron powder diffraction. X-ray and neutron PDF analysis was used to investigate if there was local ordering of the anionic lattice.

4.2 Synthesis

Perovskite oxynitride materials were synthesized by nitridation of three different lanthanum oxide precursors: $La_2Ti_2O_7$, La_2TiO_5 and $La_4Ti_3O_{12}$. The $La_2Ti_2O_7$ and $La_4Ti_3O_{12}$ precursors were prepared by heating stoichiometric amounts of La_2O_3 (Alfa Aesar, 99.99%) and

TiO_2 (Alfa Aesar 99.9%) in air. The $La_2Ti_2O_7$ sample was obtained after heating for 24 hours at 1250° C with intermittent grinding to ensure sample homogeneity. $La_4Ti_3O_{12}$ was obtained by first heating the sample at 1350° C for 216 hours then at 1550° C for 176 hours. The sample was then ground in a vibratory ball mill for 14 hours and heated again at 1350° C for 48 hours. La_2TiO_5 was synthesized using a NaCl flux. La_2O_3, TiO_2 and NaCl were mixed in a 1:1:2 ratio by mass and heated at 1000° C in air for 66 hours. After heating, the flux was dissolved using DI water.

To make the perovskite oxynitride phases, precursors were nitrided by heating at 950° C in a Lindberg/Blue M TF55035A-1 tube furnace using a 1 inch diameter quartz tube under 40 mL/min. flowing NH_3 gas. Nitridation time depended on sample size and varied from 24-72 hours. $LaTiO_2N$ samples made from starting materials that had an La:Ti ratio exceeding 1:1 (La_2TiO_5 and $La_4Ti_3O_{12}$) contained La_2O_3 as an impurity phase. The excess La_2O_3 removed by washing the sample several times with ~2M nitric acid.

X-ray powder diffraction data was collected on beamline 11-BM at the Advanced Photon Source (APS) located at Argonne National Lab. Data was collected at a temperature of 300 K. The X-ray wavelength used was $\lambda = 0.413025$ Å over a range of 0.5-50° 2θ and a 0.001 Å step size. 11-BM is equipped with a Si(111) double crystal monochrometer and 12 independent analyzer sets with 2θ separation of ~2°, Si(111) analyzer crystals and $LaCl_3$ scintillation detectors. The resolution is $\Delta Q/Q \approx 2\text{x}10^{-4}$.

Time-of-flight (TOF) neutron diffraction and PDF data were collected on the NOMAD instrument in the Spallation Neutron Source (SNS) located at Oak Ridge National Laboratory. Data was collected at a temperature of 300 K. The wavelength range is 0.1-3 Å. The flux on the

samples was ~1x10^8 neutron cm^{-2} sec^{-1}. Collection times were 60 minutes per sample. 4 detector banks were used at 31°, 67°, 122° and 154° with ranges in *d* of 0.25−6.85, 0.13−3.76, 0.13−2.10, and 0.13−1.57 respectively. Rietveld refinement of the diffraction data was done using the program Topas[100]. PDF data was processed using the Mantid software suite and the data was modeled using the program PDFgui[27].

Thermogravimetric analysis (TGA) data were collected using a TA instruments TGA Q 5000. The samples were loaded in to alumina pans and reacted under 25 mL/minute flowing oxygen while the mass was recorded. N_2 was used as the balance and purge gas. The mass was measured in 0.125 second intervals. All samples were rested at room temperature for 2 hours to allow the gas flow to stabilize. This helped remove artifacts due to variations in the measured weight due to buoyancy effects. After the data was collected a buoyancy correction was applied across data collected at all temperatures, but was found to have no significant effect on the results of the analysis. Powder XRD data were collected on both the as-prepared and oxidized samples using a Bruker D8 Advance laboratory diffractometer (λ = 1.54059 Å, 12 mm variable slits and a 192-channel Lynx-Eye linear strip detector) and was used to determine their initial phase content and the phase content after oxidation.

4.3 Results and discussion

4.3.1 Optical properties

Three samples of the nominal composition $LaTiO_2N$ were made by nitridation of three different lanthanum oxide precursor phases, La_2TiO_5, $La_2Ti_2O_7$ and $La_4Ti_3O_{12}$. The resulting compounds were colored orange, brown and red respectively. Diffuse reflectance data were collected on each of the samples to quantitatively investigate their visible light absorption and

determine their band gaps. Three features are apparent when the data collected on the different $LaTiO_2N$ samples are compared, the main absorption edge that appears just above 2 eV, a broad peak below the main absorption edge that sits at approximately 1.4 eV (in the brown and red samples, but absent from the orange sample) and absorption due to free carriers. (Figures 4.1 and 4.2)

The band gap values were determined by fitting the main absorption edge using the model for a direct transition:

$$\alpha(E) = A\frac{\left(E - E_g\right)^2}{E}$$

where A is a scale factor and E_g is the band gap energy[25]. $LaTiO_2N$-B and $LaTiO_2N$-O samples have similar direct optical band gaps of 2.20 and 2.24 eV respectively. $LaTiO_2N$-R has a substantially smaller band gap of 2.06 eV, reduced by approximately 0.2 eV. (Figures 4.1)

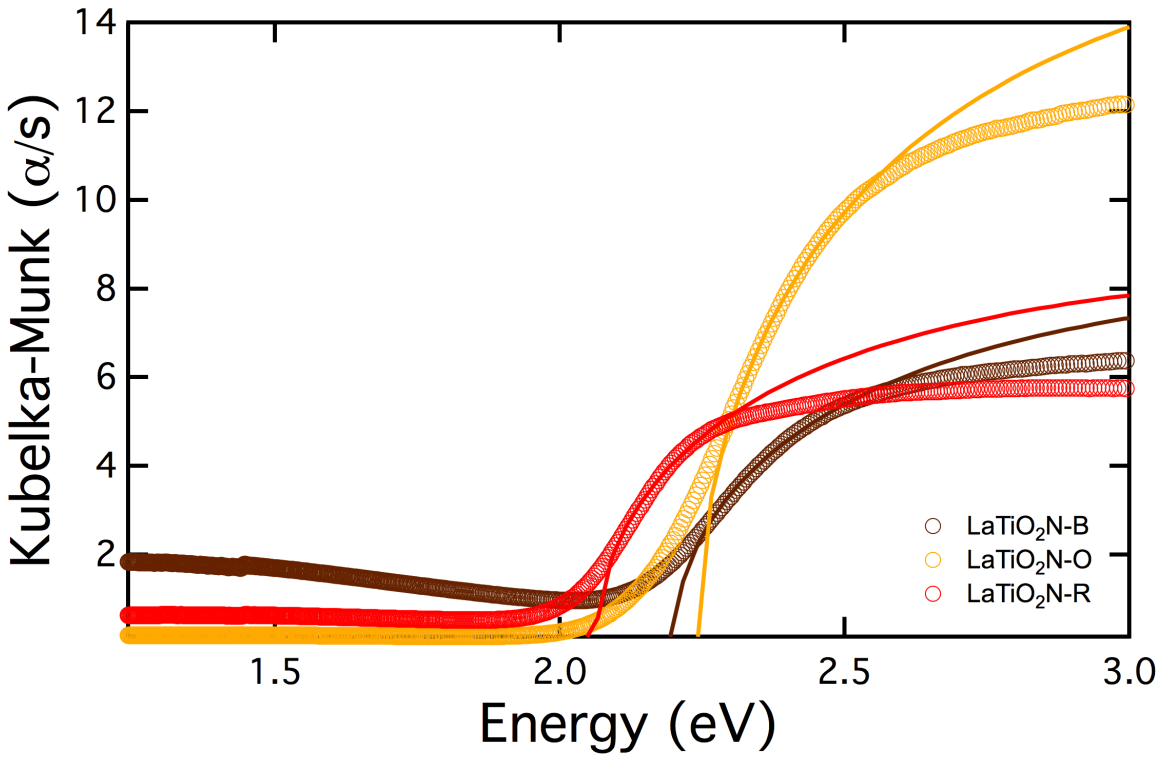

Figure 4.1 The absorption behavior of $LaTiO_2N$-R (red), $LaTiO_2N$-O (orange) and $LaTiO_2N$-B (brown). The data was fitted to the model for a direct band gap transition (black). The E_g of $LaTiO_2N$-O (2.24 eV) and $LaTiO_2N$-B (2.20 eV) are nearly identical while the value of E_g of $LaTiO_2N$-R is 2.06 eV.

Table 4.1 Band edge fit parameters of $LaTiO_2N$-O, $LaTiO_2N$-B and $LaTiO_2N$-R

	$LaTiO_2N$-O	$LaTiO_2N$-B	$LaTiO_2N$-R
E_g	2.24	2.20	2.06
A	48	25	24

The absorption feature appearing at approximately 1.4 eV decreases in intensity as the La:Ti ratio of the precursor oxide increases. (Figure 4.2.) $LaTiO_2N$-B has the most absorption below the band gap, $LaTiO_2N$-O has almost none and $LaTiO_2N$-R falls between. This feature appears at the same energy in each of the samples indicating that this lower energy peak is likely

due to absorption by Ti^{3+} species and not differences in the O:N ratio[101]. The formation of these defects appears to be suppressed by excess La in the precursor oxide and is the source of the color difference between the $LaTiO_2N$-B and $LaTiO_2N$-O samples. It is expected then that if the Ti^{3+} in the brown compound were oxidized to 4+ then this sample would appear orange as well. The lower position of the main absorption edge of $LaTiO_2N$-R indicates more significant structural or compositional differences between it and the other two samples.

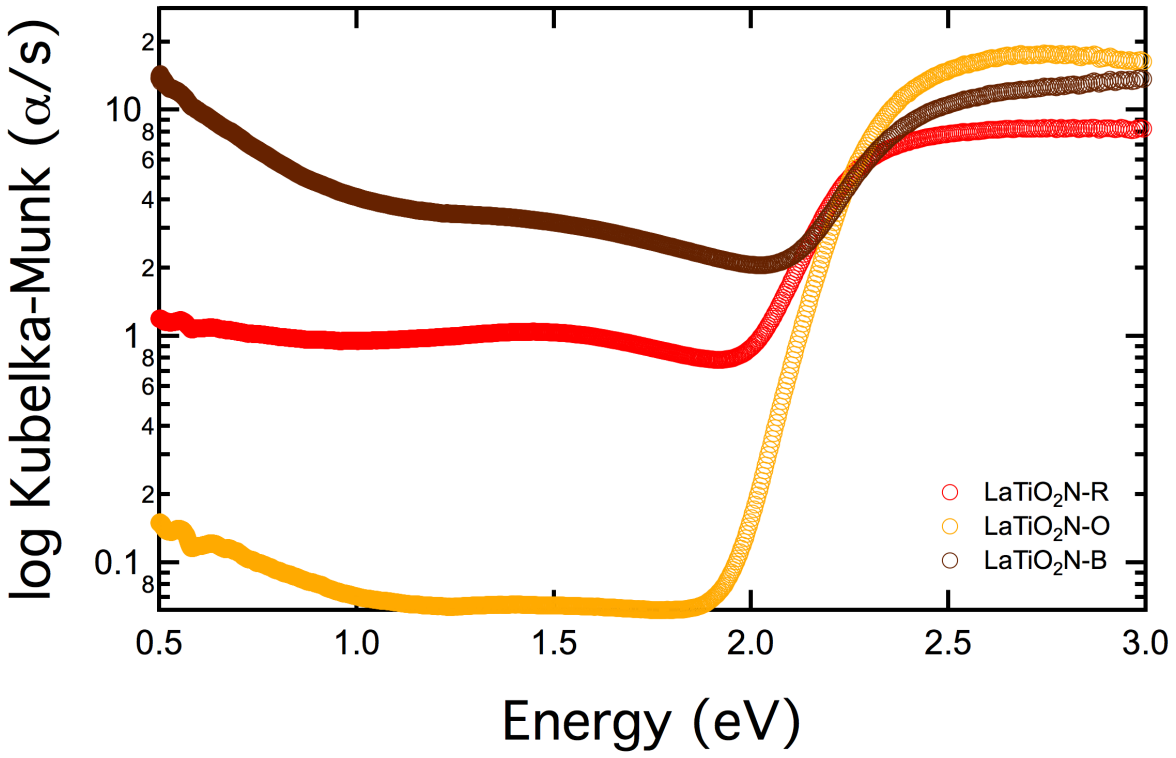

Figure 4.2 The bidirectional reflectance data for the $LaTiO_2N$ samples. The $LaTiO_2N$-B sample has the greatest absorption below the band edge, the $LaTiO_2N$-O sample the least and the $LaTiO_2N$-R sample falls between the two.

4.3.2 Thermogravimetric analysis

Thermogravimetric analysis was used to clarify the stoichiometry of the $LaTiO_2N$ samples examined in this work. As the oxynitride $LaTiO_2N$ is oxidized, the nitrogen in the

sample is replaced with oxygen so that the mass gain follows the formula is $LaTiO_{2+1.5x}N_{1-x}$. Assuming that there are no cation or anion vacancies in the structure this would lead to a net mass gain of 4.29% between the stoichiometric $LaTiO_2N$ and the fully oxidized lanthanum titanate product, $La_2Ti_2O_7$. The results of the TGA experiment performed on the $LaTiO_2N$ samples are shown in Figure 4.3. In the figure the mass change behavior during oxidation is indicated by a solid line and the temperature of reaction as a function of time is indicated by a dashed line. Each sample showed a similar pattern of mass change when oxidized. First, when the samples were initially heated to 250° C where there is a small mass loss, presumably due to water evaporation. Then, as the temperature approached 250° C, the samples began to show a mass increase that begins between 200 and 300° C. This is presumably the point where nitrogen begins to leave the lattice and is replaced by oxygen. The rate of this mass increase climbs until it peaks at approximately 480° C. The mass of the samples increases until they stabilize. When the sample is heated to higher temperatures, the mass drops again until the mass stabilizes and the sample is fully oxidized. The mass change (%) between the mass after the initial water loss (M1) and the mass at 450° C (M2) and the mass change between M1 and the mass of the fully oxidized sample (M3) are tabulated in table 4.3. M1 for the $LaTiO_2N$-R sample was corrected for the presence of the Ti^{4+} containing impurities by subtracting the masses of the impurity phases, determined by Rietveld refinement of the oxynitride XRD data from the mass of the as synthesized oxynitride sample. The impurities in the other samples were minor enough not to affect the outcome of the analysis.

The sample mass increase by 480° C are ~2% greater than expected for the fully oxidized compound. This is believed to be due to nitrogen trapped in the crystal as N_2. We suspect that starting at around 200° C oxygen begins to replace nitrogen in the compound. Some nitrogen

near the surface of the $LaTiO_2N$ particles leaves, but most remains trapped in the crystal as neutral N_2 since the mobility is too low at these temperatures for the large N_2 molecules to diffuse to the surface. At 950° C the lattice mobility is large enough to allow the excess nitrogen to be completely driven off, which results in the pure lanthanum titanium oxide phases. This type of behavior is typical for many oxynitride compounds[102, 103].

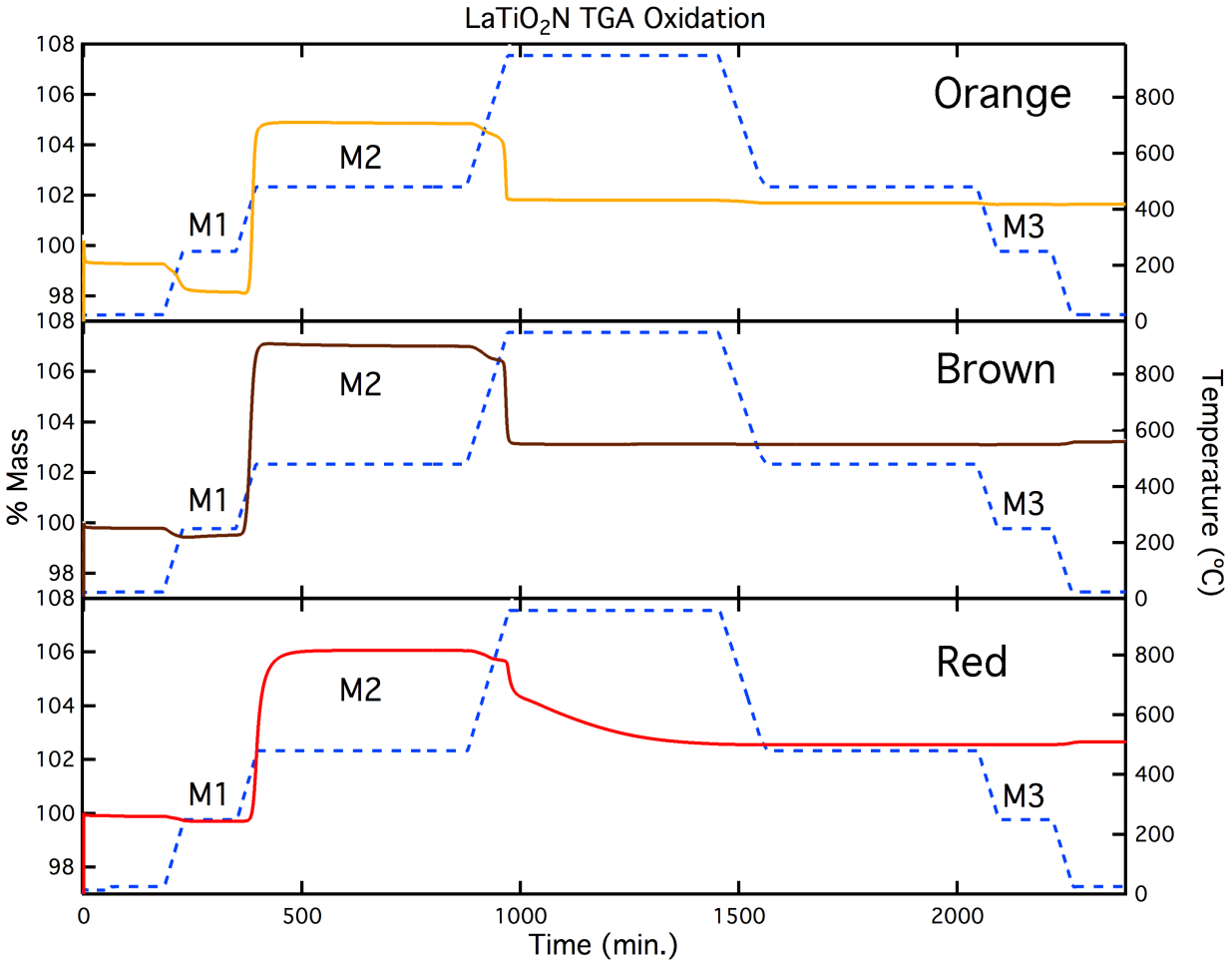

Figure 4.3 Thermogravimetric analysis data of $LaTiO_2N$–orange (top), $LaTiO_2N$–brown (middle), and $LaTiO_2N$–red (bottom) along with the temperature profile for the reactions (blue dotted). The increase in mass beyond what is expected for the fully oxidized lanthanum titanate is caused by N-N dimers trapped in the crystal structure. At higher temperatures this nitrogen is driven off and the mass drops to that expected for the pure oxide. This behavior is common for similar oxynitride materials.

Table 4.2 Masses and mass change (%) during oxidation of $LaTiO_2N$ between select temperatures

	M1	M2	M3	M1→M2	M1→M3
$LaTiO_2N$-O	12.324	13.170	12.776	6.865%	3.668%
$LaTiO_2N$-B	43.542	46.893	45.147	7.696%	3.686%
$LaTiO_2N$-R	40.803	43.803	42.146	7.352%	3.291%

The measured mass changes between M1 and M3 were 3.68% and 3.69% for the $LaTiO_2N$-O and $LaTiO_2N$-B compounds respectively and 3.29% for the $LaTiO_2N$-R compound. These mass change values are lower than the expected value of 4.29%. This suggests that each sample had a O:N ratio > 1 and/or contained anionic vacancies.

The cation stoichiometry was investigated using Rietveld analysis of the fully oxidized samples. Since neither La nor Ti are expected to evaporate under the reaction conditions of the TGA experiment the metal content of the sample before and after oxidation will remain unchanged. After the measurement the samples are fully oxidized and the amount of La and Ti can be determined since the stoichiometry of the oxides phases are unambiguously known. This allows the oxidation state of the Ti cation (the only cation likely to exist in a reduced state) to be calculated via charge balance once the O:N ratio of the samples has been determined from the mass change.

The oxidized products of $LaTiO_2N$-O and $LaTiO_2N$-B were found to be pure $La_2Ti_2O_7$ while the oxidized $LaTiO_2N$-R sample consisted of approximately 72 mol % $La_2Ti_2O_7$, 13 mol % La_2TiO_5 and 15 mol % $La_4Ti_3O_{12}$. After correcting for the oxide impurities in the oxynitride

samples the La:Ti ratio of the $LaTiO_2N$ phase in each sample was determined to be 1:1 to within the detection limit of the X-ray diffraction experiment.

The oxygen and nitrogen content of the samples were calculated from the difference between the M1 and M3 values. This mass difference depends on both the O:N ratio and the Ti valence state of the oxynitride material, so the assumption was made that there were no anionic vacancies and the total mass change during oxidation is attributed to oxygen replacing nitrogen in the compound, which is likely true to a first approximation. In this case, for a given valence of Ti there is only one possible O:N ratio for a given mass change when it is oxidized can be calculated. Upon oxidation each nitrogen atom in the as synthesized lanthanum nitrides is replaced with 1.5 oxygen atoms until the sample is completely oxidized. The O:N ratio was calculated assuming a La valence of 3+, an oxygen valence state of 2+, a nitrogen valence state of 3+. To determine the O:N ratio of the samples the value the Ti valence was adjusted until the mass difference between the theoretical oxynitride compound and the fully oxidized compound equaled the difference of M3 and M1.

The mass change associated with $LaTiO_2N$-O and $LaTiO_2N$-B indicates a stoichiometry of $LaTiO_{2.14}N_{0.86}$ and a +3.86 oxidation state of Ti. The mass change of the $LaTiO_2N$-R sample during oxidation indicates a $LaTiO_{2.23}N_{0.77}$ stoichiometry and a Ti oxidation state of +3.77. If there are La vacancies then the Ti oxidation state would approach 4+ as the concentration of La vacancies increased, but both the X-ray and neutron diffraction data indicated that the La:Ti ratio was 1:1, so the fully occupied model was used.

Table 4.3 Reduced stoichiometry and Ti valence for $LaTiO_2N$

	Deduced formula	Ti Valence
$LaTiO_2N$-O	$LaTiO_{2.14}N_{0.86}$	+3.86
$LaTiO_2N$-B	$LaTiO_{2.14}N_{0.86}$	+3.86
$LaTiO_2N$-R	$LaTiO_{2.23}N_{0.77}$	+3.75

These results are surprising given that the $LaTiO_2$-R sample, which has a narrower band gap than the other two samples, also was found to have the least nitrogen among the three samples examined. Additionally, the valence state of the Ti atoms seem unusually low. At least for $LaTiO_2N$-O, the lack of light absorption below the band gap would indicate that, the valence is very close to 4+. To account for this seeming discrepancy, a model that included anion vacancies and a model with an O:N ratio < 1 were applied, but each resulted in an even further reduced value of the Ti valence. The possibility that the observed mass change is due to a hydroxide or other species absorbed on the surface was considered, but rejected as unlikely given the magnitude of the difference between the observed and expected mass changes. It could be that the initial mass of the samples was over estimated making the value of the mass change between the pristine and fully oxidized sample seem smaller than it actually is, but there is no obvious reason why the initial mass would appear heavier than it actually is. As of now this remains an open question.

Despite these inconstancies, it can be seen that the $LaTiO_2$-O and $LaTiO_2$-B compounds have nearly identical stoichiometries. The color difference between these two samples is likely due to a small number of Ti^{3+} defects that are present in the brown sample, but are below the detection limit of our experiments. The $LaTiO_2N$-R has a slightly O:N ratio, which likely accounts for the shift of its band edge. These results indicate that the absorption behavior of

compounds with the nominal stoichiometry $LaTiO_2N$ depend greatly on the presence of defects such as reduced Ti and on the O/N ratio.

4.3.3 Structural studies

Powder diffraction data was used to determine if there were any structural differences between the different variants of $LaTiO_2N$. There has been a previous investigation of $LaTiO_2N$ by Clarke *et al.* using powder neutron diffraction data[83]. $LaTiO_2N$ was found to have a triclinic, distorted perovskite structure, however the deviations are slight and the compound is nearly cubic. Also, no significant long-range ordering of the oxygen and nitrogen on the anionic sites was found.

The Clarke model was used as a starting point for our structure refinements. Preliminary Rietveld refinements of the X-ray diffraction data collected for this work show that the $LaTiO_2N$-O and $LaTiO_2N$-B samples are well described by the Clarke model, while the $LaTiO_2N$-R sample is much less so. In addition to the main phase, all nitride samples show minor impurity phases. $LaTiO_2N$-O has a La_2TiO_5 (*Pnma*) phase impurity, $LaTiO_2N$-B has an unknown phase impurity and $LaTiO_2N$-R has La_2TiO_5, rutile and La_2O_3 impurity phases. The presence of some impurities is not surprising given that with the exception of $La_2Ti_2O_7$ the starting materials were La-rich. The impurities were modeled as separate phases in all refinements excepting the unknown phase, however the results of the analysis appeared to be unaffected by its presence.

The raw powder XRD patterns of the $LaTiO_2N$ samples are shown in Figure 4.4. By comparing the data collected on the $LaTiO_2N$-R sample with the other two samples it can be seen that the peaks of the $LaTiO_2N$-R phase are shifted to lower positions in 2θ than their counterparts

in the $LaTiO_2N$-O and $LaTiO_2N$-B samples, indicating a slightly larger unit cell than $LaTiO_2N$-O and $LaTiO_2N$-B.

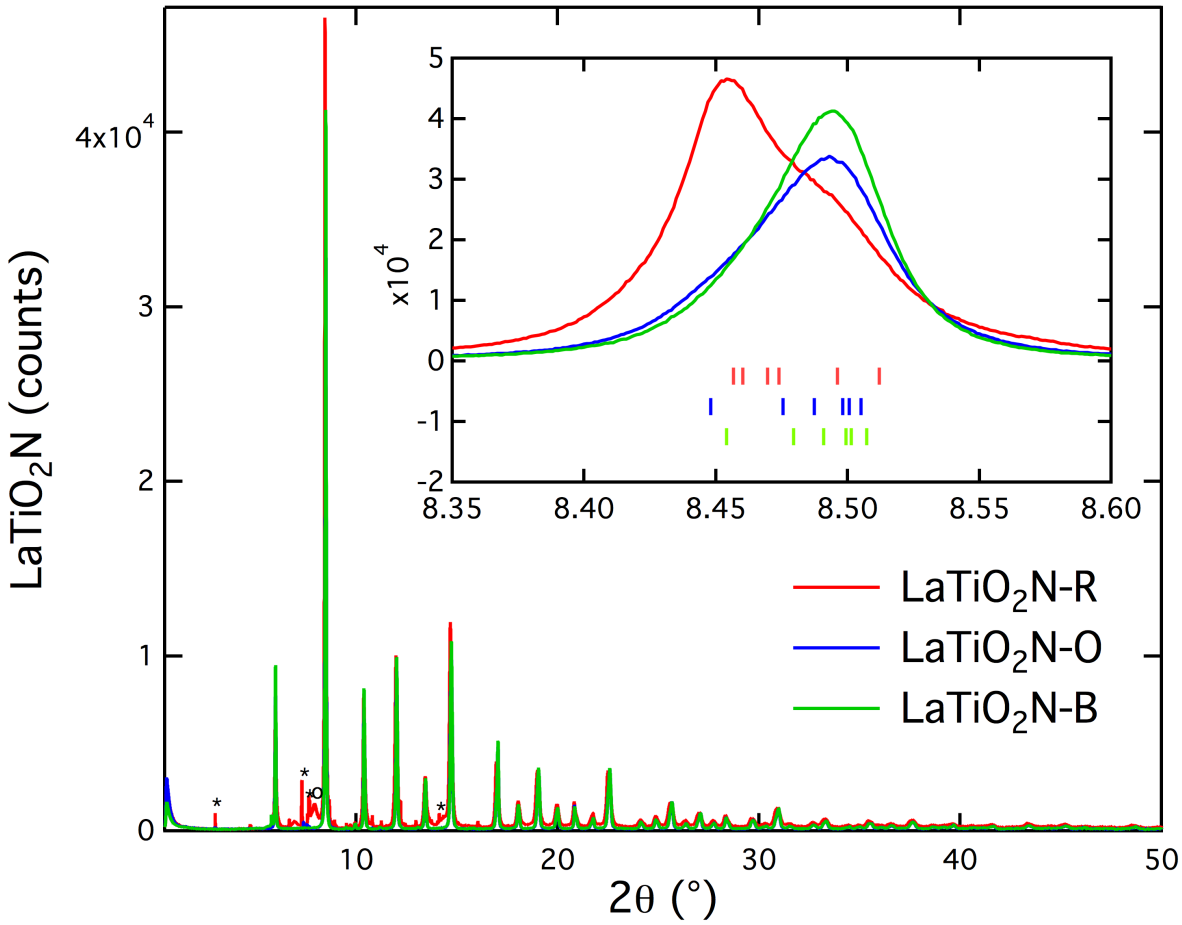

Figure 4.4 An overlay of the x-ray powder diffraction patterns of $LaTiO_2N$-O, $LaTiO_2N$-B and $LaTiO_2N$-R. $LaTiO_2N$-O and $LaTiO_2N$-B overlay well, but the peaks in the $LaTiO_2N$-R pattern are shifted to lower 2θ, indicating a larger unit cell (inset). La_2TiO_5 (*) and La_2O_3 (o) impurity phases present in $LaTiO_2N$-R are marked.

Neutron powder diffraction data was also collected on samples of the three different colors of $LaTiO_2N$. Neutron diffraction is much more sensitive to oxygen and nitrogen than X-ray diffraction and can be used to examine structural features in the anionic lattice such as vacancies and oxygen/nitrogen occupancies.

The neutron and X-ray data were co-refined. Although, the unit cell parameters were determined separately using only the X-ray data and not allowed to refine until the last stages of the refinement. The refined unit cell parameter values and the values reported by Clarke *et al.* are shown in Table 4.4.

Table 4.4 The unit cell parameters of $LaTiO_2N$ samples made with different phases of lanthanum titanate precursors

	Clarke *et al.*	$LaTiO_2N$-O	$LaTiO_2N$-B	$LaTiO_2N$-R
a Å	5.582	5.589(3)	5.5854(3)	5.582(5)
b Å	5.5752	5.572(3)	5.5725(3)	5.574(2)
c Å	5.5904	5.580(4)	5.5798(3)	5.590(4)
α °	59.839	59.98(3)	59.98(2)	59.88(6)
β °	60.278	60.25(2)	60.24(2)	60.24(4)
γ °	59.968	59.88(3)	59.90(3)	59.90(8)
V Å^3	123.1	122.9	122.8	123.0

Initially the structures were modeled with fully occupied anion sites and fully disordered O/N occupancies (2/3 O and 1/3 N on each anion site). The isotropic displacement parameters of the anion sites were constrained to be equal and allowed to refine along with the La and Ti isotropic displacement parameters and the positions of all atoms. When anisotropic displacement parameters were used the parameters refined to unreasonable values. This model fit the $LaTiO_2N$-O data and the $LaTiO_2N$-B data well. Allowing the occupancies to refine did not reproducibly improve the fit indicating that there was no significant site preference among the oxygen and nitrogen atoms, although this does not preclude the presence of local ordering, to which diffraction is insensitive. Refining the occupancies of the La and Ti atoms did not

significantly improve the fit to the data collected on either the $LaTiO_2N$-O or $LaTiO_2N$-B indicating a 1:1 lanthanum to titanium ratio.

Table 4.5 Atomic parameters of $LaTiO_2N$-B determined by X-ray/neutron co-refinement

Atom	*x*	*y*	*z*	S.O.F.	B_{eq}
La	0.245(1)	0.254(2)	0.250(1)		0.44(1)
Ti1	0	0	0		0.25(1)
Ti2	1/2	1/2	1/2		0.25(1)
O1/N1	0.304(3)	0.749(4)	0.196(3)	0.66/0.33	1.33(1)
O2/N2	0.237(3)	0.266(4)	0.701(3)	0.66/0.33	1.33(1)
O3/N3	0.793(3)	0.228(4)	0.270(3)	0.66/0.33	1.33(1)

Table 4.6 Atomic parameters of $LaTiO_2N$-O determined by X-ray/neutron co-refinement

Atom	*x*	*y*	*z*	S.O.F.	B_{eq}
La	0.2447(5)	0.2586(8)	0.2353(4)		0.234(6)
Ti1	0	0	0		0.822(9)
Ti2	1/2	1/2	1/2		0.822(9)
O1/N1	0.308(1)	0.746(2)	0.193(1)	0.66/0.33	1.510(6)
O2/N2	0.247(2)	0.256(2)	0.705(1)	0.66/0.33	1.510(6)
O3/N3	0.796(1)	0.232(1)	0.265(1)	0.66/0.33	1.510(6)

Table 4.7 Atomic parameters of $LaTiO_2N$-R determined by X-ray/neutron co-refinement

Atom	*x*	*y*	*z*	S.O.F	B_{eq}
La	0.61(1)	0.2665(7)	0.2465(6)		0.61(1)
Ti1	0	0	0		0.16(2)
Ti2	1/2	1/2	1/2		0.16(2)
O1/N1	0.3023(6)	0.753(1)	0.1877(5)	0.66/0.33	1.162(8)
O2/N2	0.233(1)	0.275(1)	0.705(1)	0.66/0.33	1.162(8)
O3/N3	0.780(1)	0.233(1)	0.2778(8)	0.66/0.33	1.162(8)

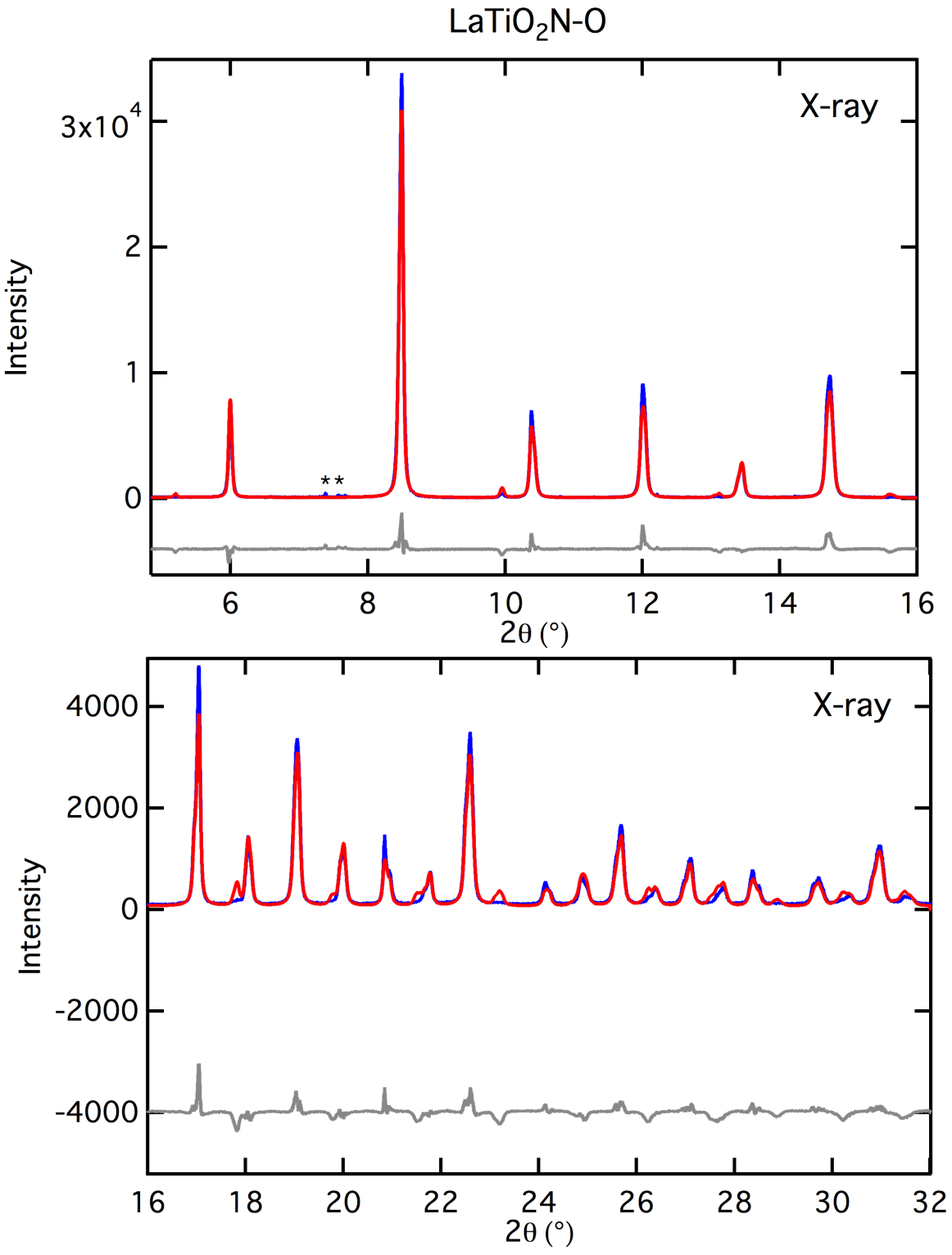

Figure 4.5 The fit to the X-ray data collected on the $LaTiO_2N$-O sample. A La_2TiO_5 (*) impurity phase present is marked.

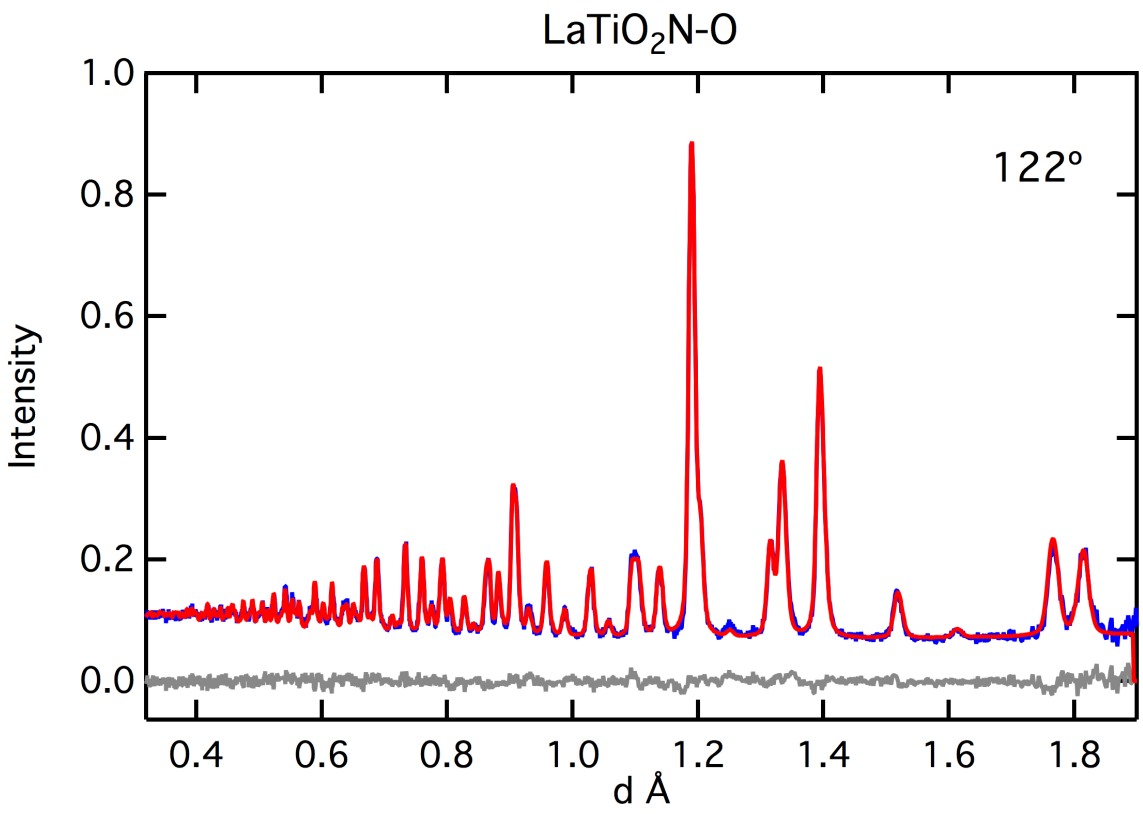

Figure 4.6 The fit to the TOF neutron data collected on $LaTiO_2N$-O (122° detector bank)

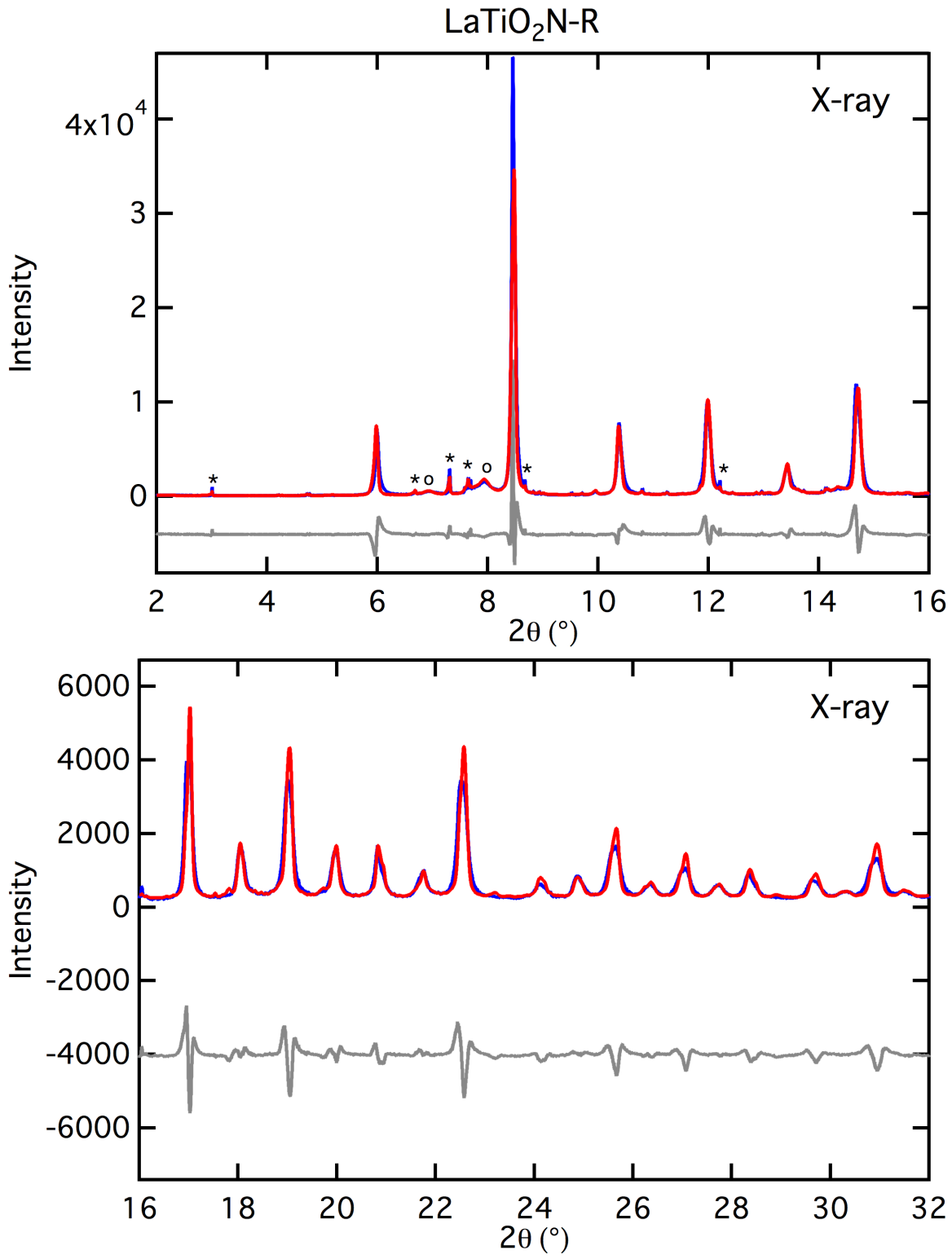

Figure 4.7 The fit to the X-ray data collected on the $LaTiO_2N$-R sample. La_2TiO_5 (*) and La_2O_3 (o) impurity phases present in $LaTiO_2N$-R are marked.

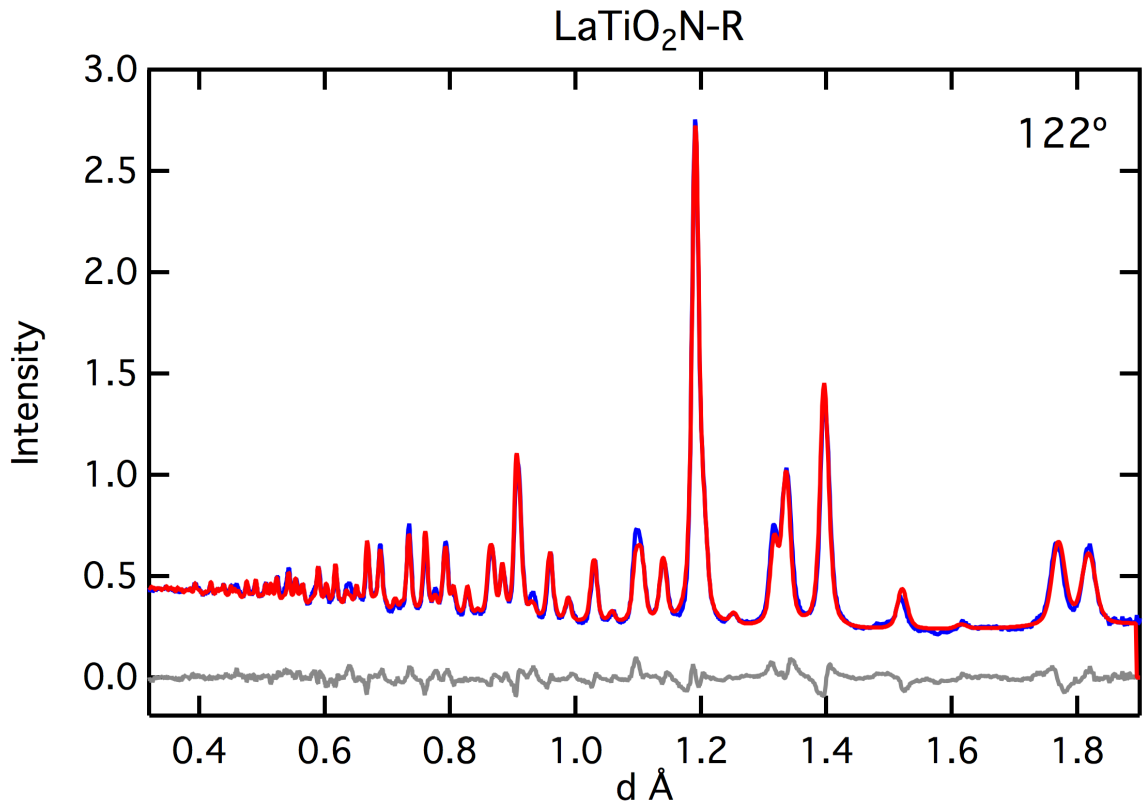

Figure 4.8 The fit to the TOF neutron data collected on $LaTiO_2N$-R (122° detector bank)

The data collected on the $LaTiO_2N$-R sample is much less well described by this disordered model than the other two samples. The peaks in the $LaTiO_2N$-R sample have a very different shape than those in the other two samples. Attempts to use anisotropic strain broadening to fit the peaks shape did not significantly improve the fit. Also, a two-phase fit was also attempted, however the fit was significantly worse than the single-phase model. This suggests that the peak asymmetry is likely due to $LaTiO_2N$-R having a different distribution of unit cell parameters than the other samples. Because of the very slight deviations from cubic symmetry shown by this material there is significant peak overlap making determination of exact unit cell parameters difficult and a set of unit cell parameters that fits the $LaTiO_2N$-R well is yet to be found.

The presence of local ordering in the O/N lattice of $LaTiO_2N$ was examined using X-ray and neutron PDF. The data was fit to the Clarke model and although ordered O/N models were tried, significant improvements to the fit to the data was not seen. This does not preclude the presence of local order however. A more care full analysis needs to be done to determine the local structure of lanthanum titanium oxynitride compounds.

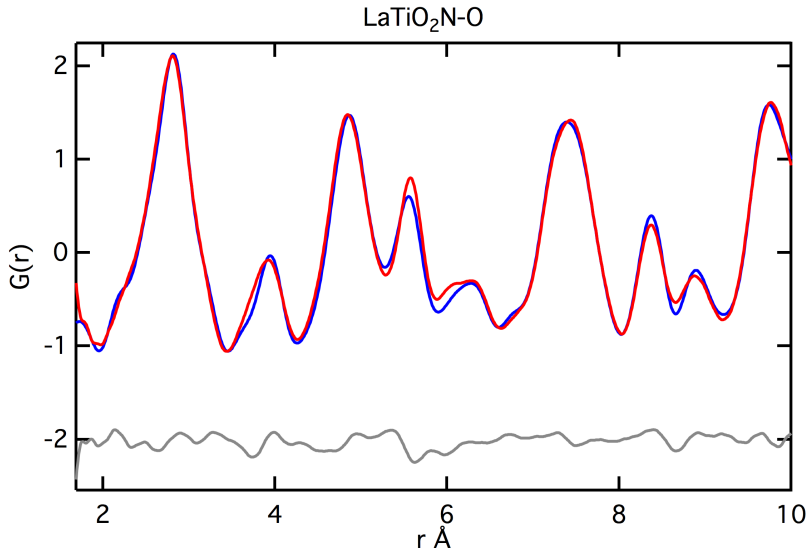

Figure 4.9 The neutron PDF data collected on the $LaTiO_2N$-O sample fit to 10 Å using a model without O/N order.

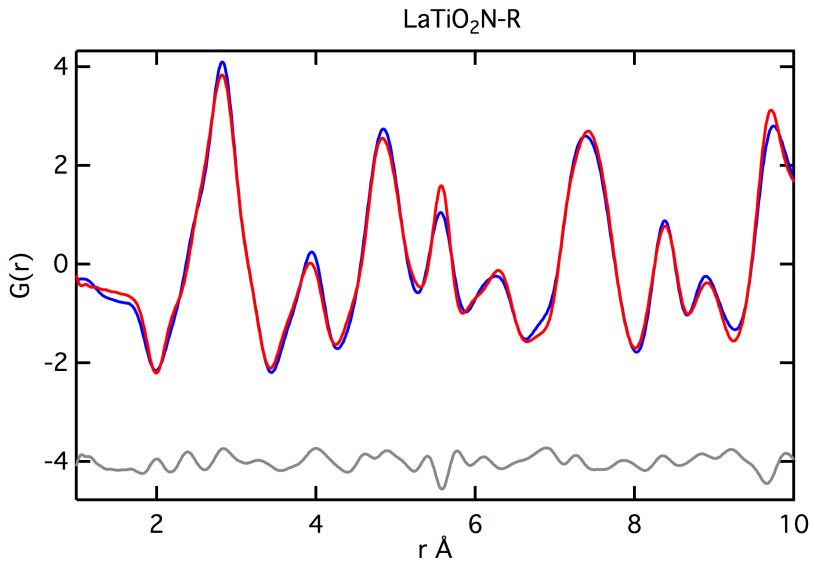

Figure 4.10 The neutron PDF data collected on the $LaTiO_2N$-R sample fit to 10 Å using a model without O/N order.

4.4 Conclusions

Three samples of $LaTiO_2N$ powder were synthesized by nitridation of the lanthanum oxide precursors, $La_2Ti_2O_7$, $La_4Ti_3O_{12}$ and La_2TiO_5 resulting in brown ($LaTiO_2N$-B), red ($LaTiO_2N$-R) and orange ($LaTiO_2N$-O) powders respectively. The direct gaps determined by diffuse reflectance were around 2.20 eV for the brown and orange sample, but were about 0.15 eV smaller for for $LaTiO_2N$-R. Our optical measurements indicate that the orange and brown samples are essentially identical and differ only in their doping level, as can be seen be following the intensity of features related to Ti^{3+} and to free carriers. However, a similar analysis indicates that the red sample has a doping level intermediate to that of the orange and brown phases, and that red compound must correspond to a distinct chemical phase which is different from the phase associated with the orange and brown samples. This is confirmed by X-ray and neutron diffraction measurements, which indicate a small but significant difference in the diffraction pattern of the red sample relative to the other phase. The differences between the two phases are

subtle, and could result from either a difference in chemical composition or from polymorphism (for example, the presence or absence of ordering between O and N anions).

Although further work is required to definitively identify the origin of the different behavior of the red phase, it is encouraging that the band gap of $LaTiO_2N$ can be substantially reduced through this phase change. A number of different oxynitride perovskite phases have been previously identified as promising candidates for the photoelectrochemical production of solar fuels, and a general method for enhancing their visible light absorption will be of great importance. Analogous transition-metal oxide precursor phases general exist for these different chemical systems, and might also be used to tune the properties of the oxynitride products produced by ammonolysis reactions. Additionally, it is fully expected that the methods of analyzing the below-gap absorption of oxynitride semiconductors can be extended to these other perovskite phases, and that comparative studies will provide important insights into the relative ability of these phases to be doped in a controlled fashion, and in the relative mobility of the free carriers that doping produces. Studies of this type are critical to optimizing the performance of these materials for light harvesting applications, as the properties of dopants play a critical role in determining the functionality of semiconductors.

Appendix 1

Chapter 2 supplemental information

Figure S1.1

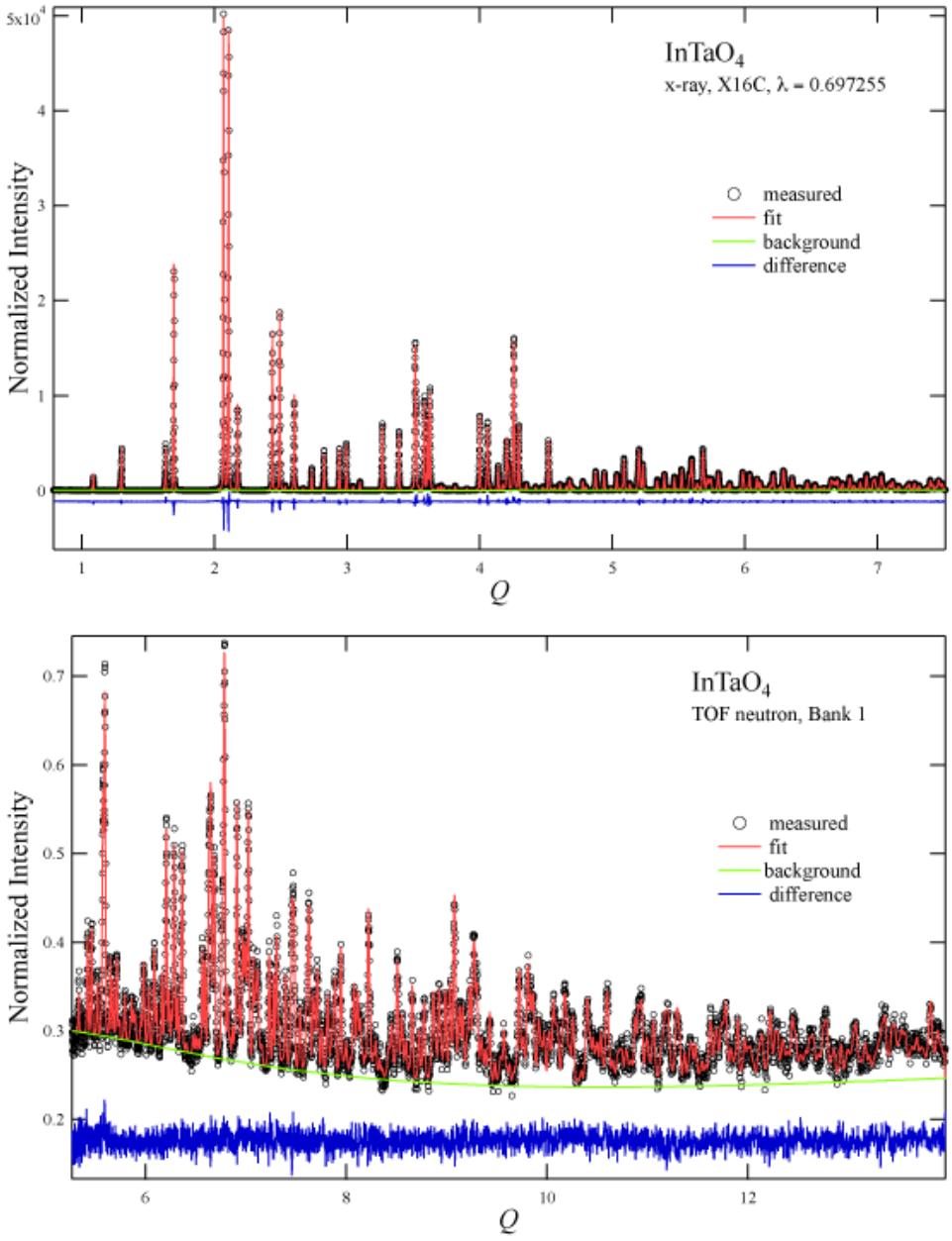

Figure S1.2

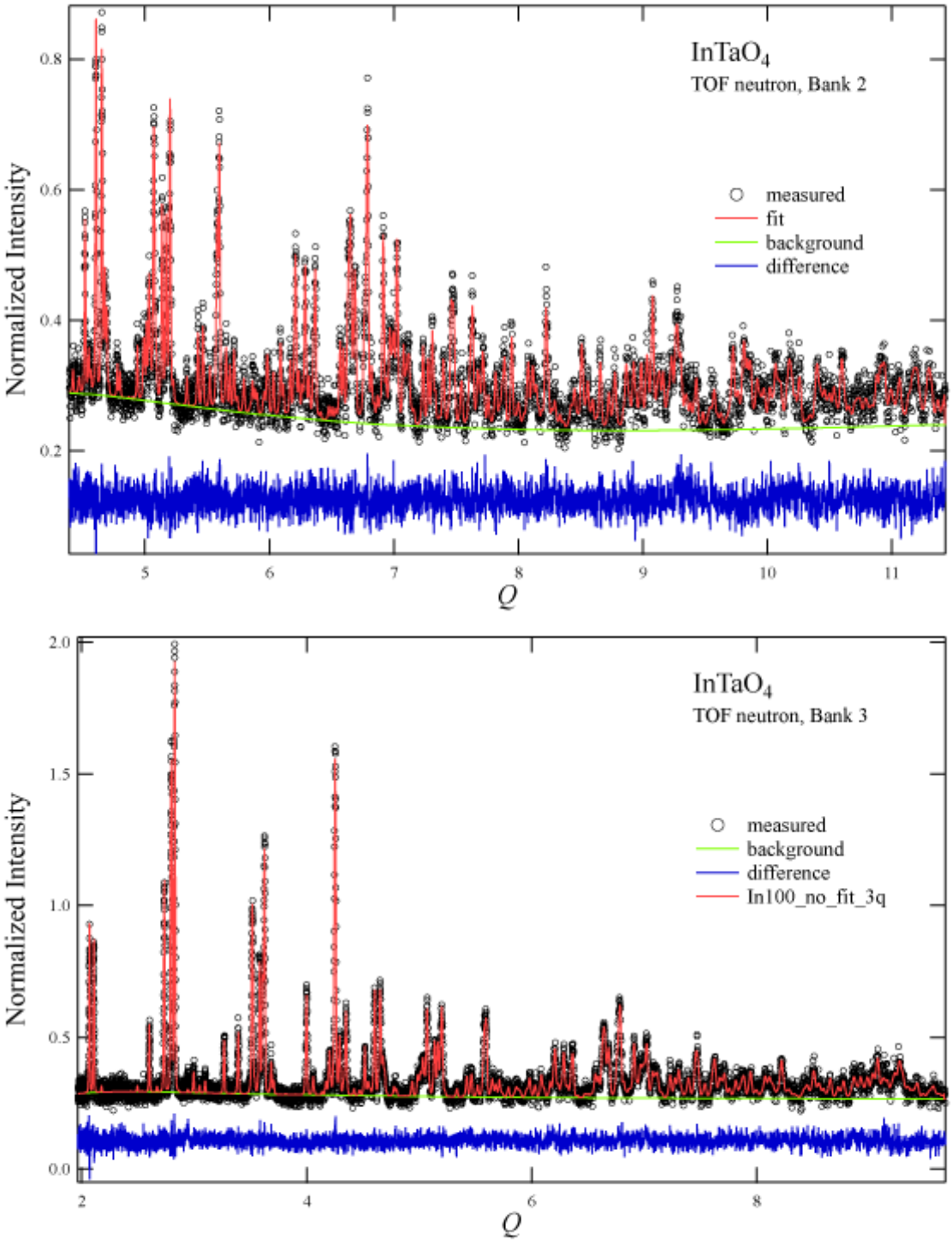
InTaO4
TOF neutron, Bank 2
measured
fit
background
difference
Normalized Intensity
Q
InTaO4
TOF neutron, Bank 3
measured
background
difference
In100_no_fit_3q
Normalized Intensity
Q

Figure S1.3

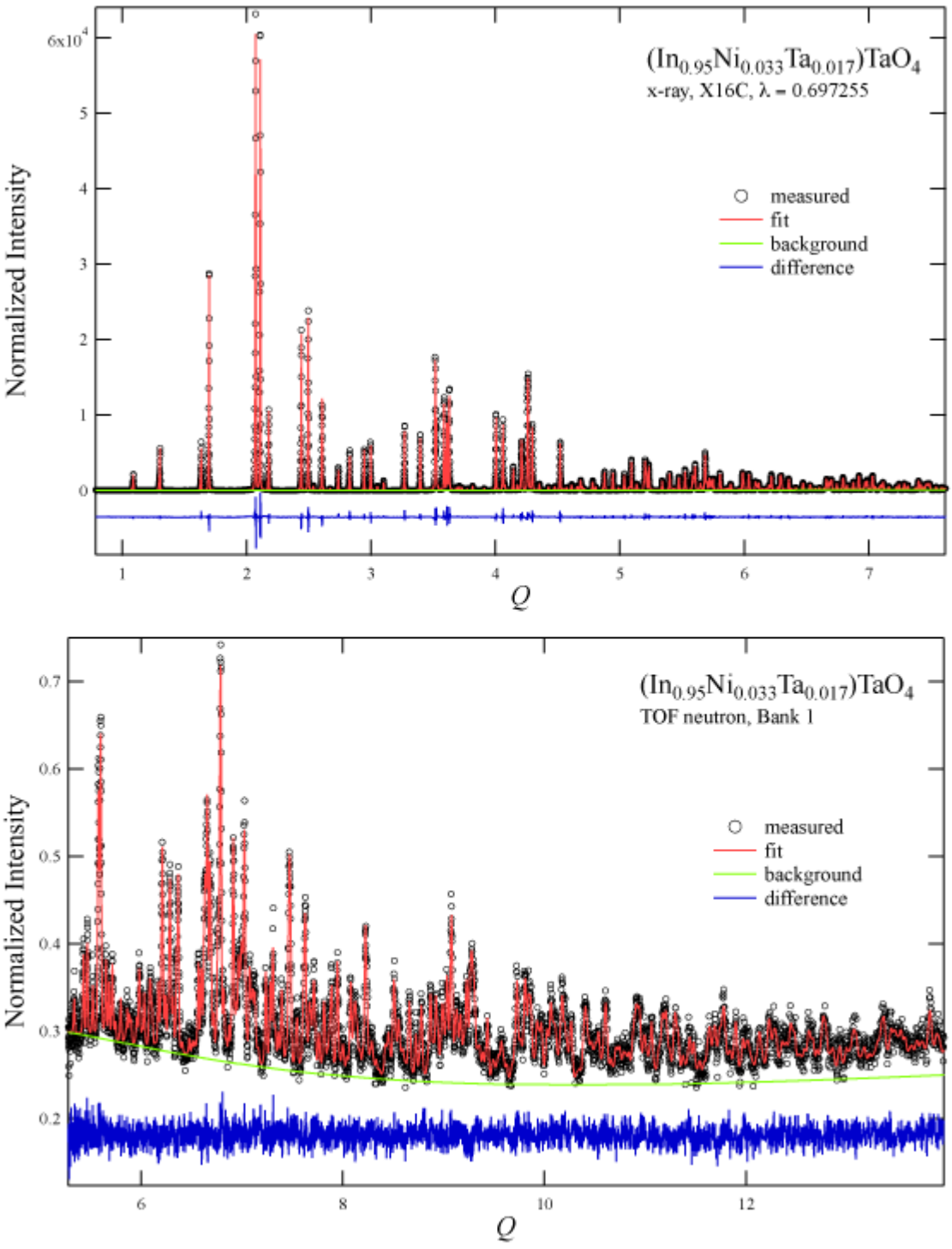
6x10^4
5
4
3
2
1
0
Normalized Intensity
(In0.95Ni0.033Ta0.017)TaO4
x-ray, X16C, λ = 0.697255
measured
fit
background
difference
1
2
3
4
5
6
7
Q
0.7
0.6
0.5
0.4
0.3
0.2
Normalized Intensity
(In0.95Ni0.033Ta0.017)TaO4
TOF neutron, Bank 1
measured
fit
background
difference
6
8
10
12
Q

Figure S1.4

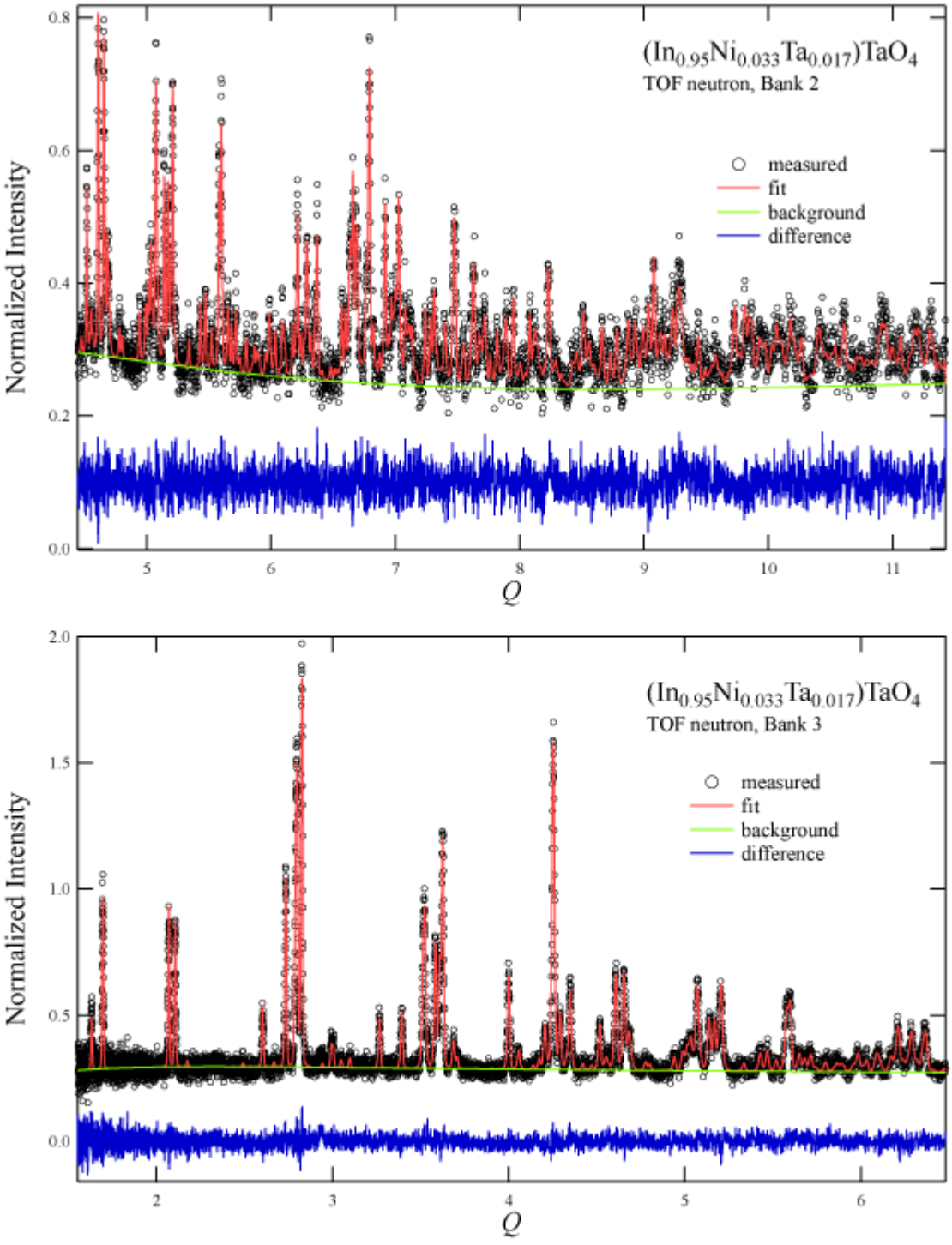
(In0.95Ni0.033Ta0.017)TaO4
TOF neutron, Bank 2
measured
fit
background
difference
Normalized Intensity
Q
(In0.95Ni0.033Ta0.017)TaO4
TOF neutron, Bank 3
measured
fit
background
difference
Normalized Intensity
Q

Figure S1.5

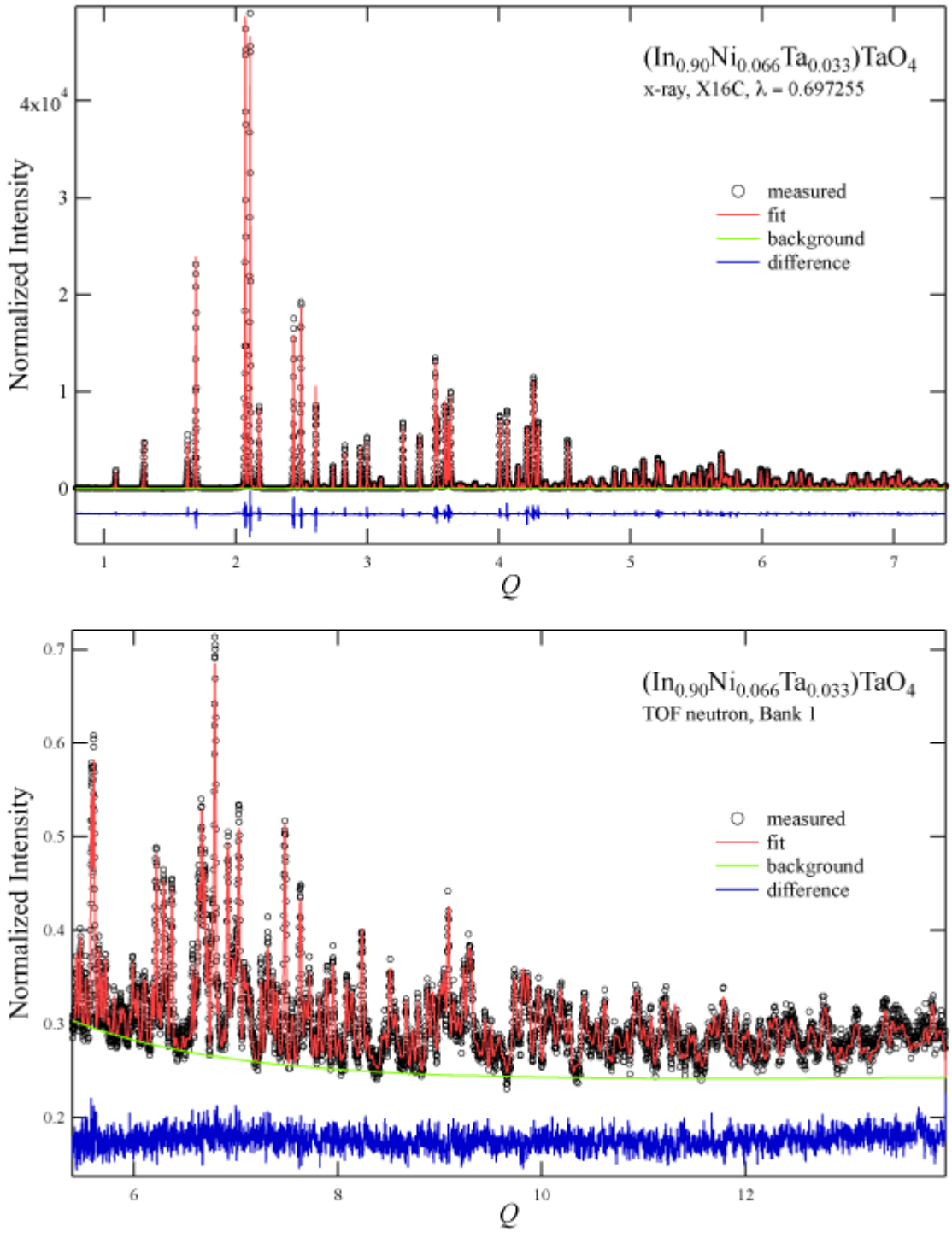
(In0.90Ni0.066Ta0.033)TaO4
x-ray, X16C, λ = 0.697255
measured
fit
background
difference
Normalized Intensity
4x10^4
3
2
1
0
1
2
3
4
5
6
7
Q
(In0.90Ni0.066Ta0.033)TaO4
TOF neutron, Bank 1
measured
fit
background
difference
Normalized Intensity
0.7
0.6
0.5
0.4
0.3
0.2
6
8
10
12
Q

Figure S1.6

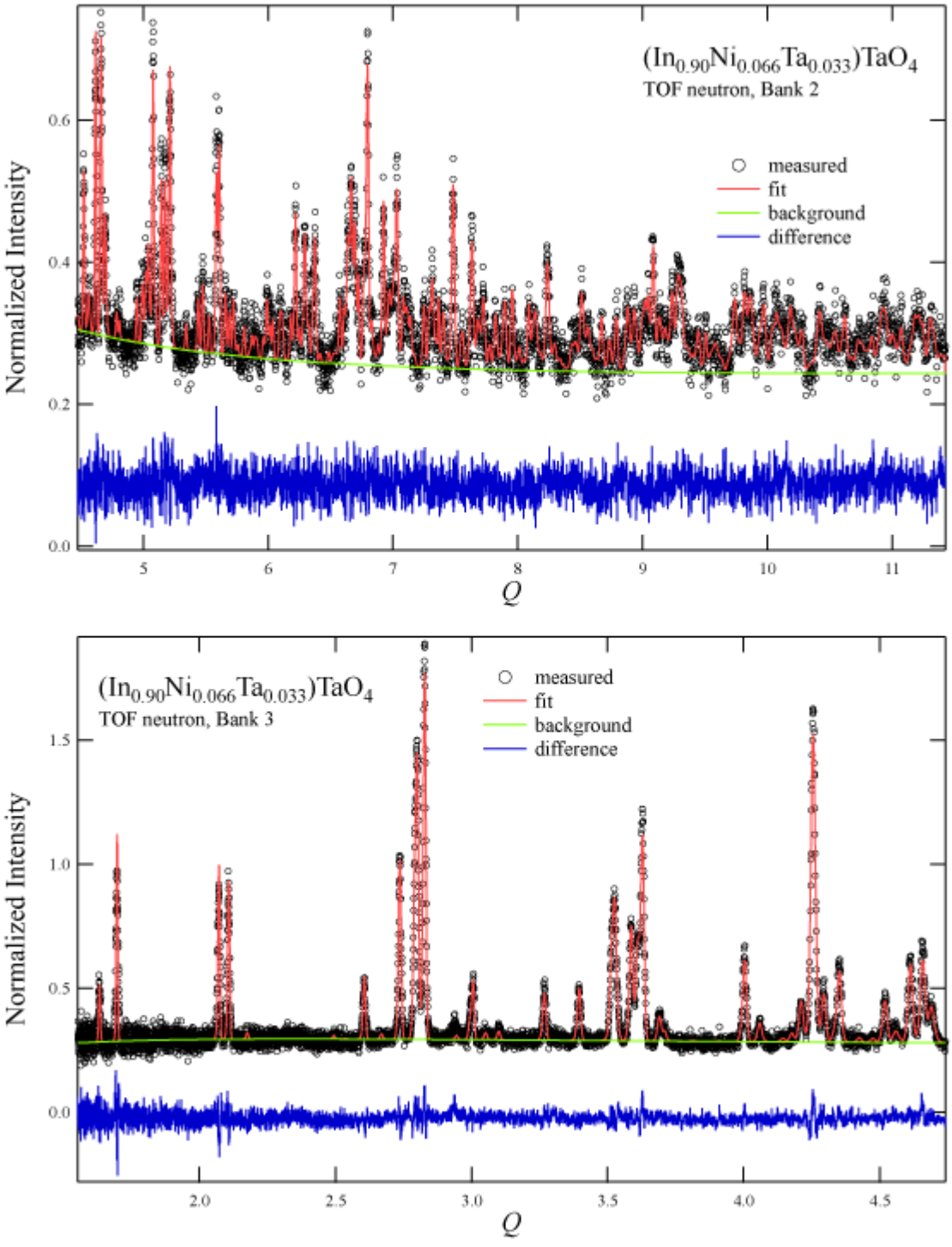
(In0.90Ni0.066Ta0.033)TaO4
TOF neutron, Bank 2
measured
fit
background
difference
Normalized Intensity
Q
(In0.90Ni0.066Ta0.033)TaO4
TOF neutron, Bank 3
measured
fit
background
difference
Normalized Intensity
Q

Appendix 2

Chapter 3 supplemental information

Spectral ellipsometry data for all film samples were collected using a J. A. Woollam M-2000 ellipsometer over a wavelength range of 210-1692 nm (5.90-0.73 eV) with a step size of 1.6 nm below 1000 nm and 3.5 nm above 1000 nm at incident angles of 50, 55, 60, 65, 70, 75 and 80° and a polarizer angle of 45°. The software package WVASE32 was used to determine optical constants and film thicknesses. Only the data collected at a 65° incident angle was used for the final fit because of artifacts in the data measured below the materials band edge believed to be caused by slight anisotropy in the $LaTiO_2N$ film. It was decided to select one incident angle for fitting since we were primarily interested in the films optical behavior above the band edge and precise modeling of the anisotropy of the film is beyond the scope of this paper. Data was also collected using a 20° polarizer angle at all incident angles and wavelengths, but was not found to be significantly different.

Data were fit to both the real (ε_1) and imaginary (ε_2) parts of the pseudodielectric constant ($\varepsilon=\varepsilon_1+i\varepsilon_2$). The final model of each layer is a linear sum of the real and imaginary parts of the total dielectric function of each individual oscillator (n) used in the model and an (ε_1) offset term, constrained in this case to equal 1. The types of oscillators used were defined as follows by reference 61.

Gaussian:

$$\varepsilon_n = (\varepsilon_{n1} + i\varepsilon_{n2})$$

$$\varepsilon_{n2} = A_n \exp{-\left(\frac{E - E_n}{\sigma}\right)^2}$$

$$\sigma = \frac{Br_n}{2\sqrt{\ln(2)}}$$

where E is energy (eV), E_n is the energy center (eV), Br_n is the broadening parameter (eV) and A_n is the dimensionless amplitude parameter. ε_{n1} is the Kramers-Kronig transformation of ε_{n2} as defined in reference 61.

Lorentzian:

$$\varepsilon_n = \frac{A_n Br_n E_n}{E_n^2 - E^2 - iBr_n E}$$

where E is energy (eV), E_n is the energy center (eV), Br_n is the broadening parameter (eV) and A_n is the dimensionless amplitude parameter.

Tauc-Lorentz:

$$\varepsilon_{n2} = \left[\frac{A_n E_{0n} C_n \left(E - E_{gn}^2 \right)}{\left(E^2 - E_{0n}^2 \right)^2 - C_n^2 E^2} \cdot \frac{1}{E} \right] \qquad E > E_{gn}$$

$$\varepsilon_{n2} = 0 \qquad E \leq E_{gn}$$

where E is energy (eV), E_{0n} is the energy center (eV), C_n is the broadening parameter (eV), A_n is the dimensionless amplitude parameter and E_{gn} is the band gap (eV). In certain cases E_{gn} for all Tauc-Lorentz oscillators in the same layer were constrained to be equal in order to improve the stability of the fit. ε_{n1} is the Kramers-Kronig transformation of ε_{n2} as defined in reference 61

Drude:

$$\varepsilon_n = \frac{-\hbar^2}{\varepsilon_0 \rho_n \left(\tau_n E^2 + i\hbar E \right)}$$

$$\rho_n = \frac{1}{q\mu N}$$

where E is energy (eV), ρ_n is the resistivity (Ω-cm), τ is the scattering time (fs), μ is the mobility ($cm^2V^{-1}s^{-1}$), and N is the carrier concentration (cm^{-3}). The constants are Plank's constant/π ($\hbar$), the vacuum dielectric constant (ε_0), and the single electron charge (q = 1.6x10^{-19} C). N was constrained to be equal to 1.5811x10^{22} cm^{-3} giving each Ti in the Drude layer an oxidation state of +3.8 assuming as opposed to +4 assumed for the rest of the $LaTiO_2N$ film.

The $LaTiO_2N$ layers of the films were fit using 2 models. One where the $LaTiO_2N$ layer was fully dense and one where it was comprised of 35% void space using the effective media approximation defined in reference 61. The following figures include fits of ε_1, ε_2, n, k, Ψ, Δ resulting from both models as well as fits to the data collected on the bare $La_2Ti_2O_7$ and $La_5Ti_5O_{17}$ substrates.

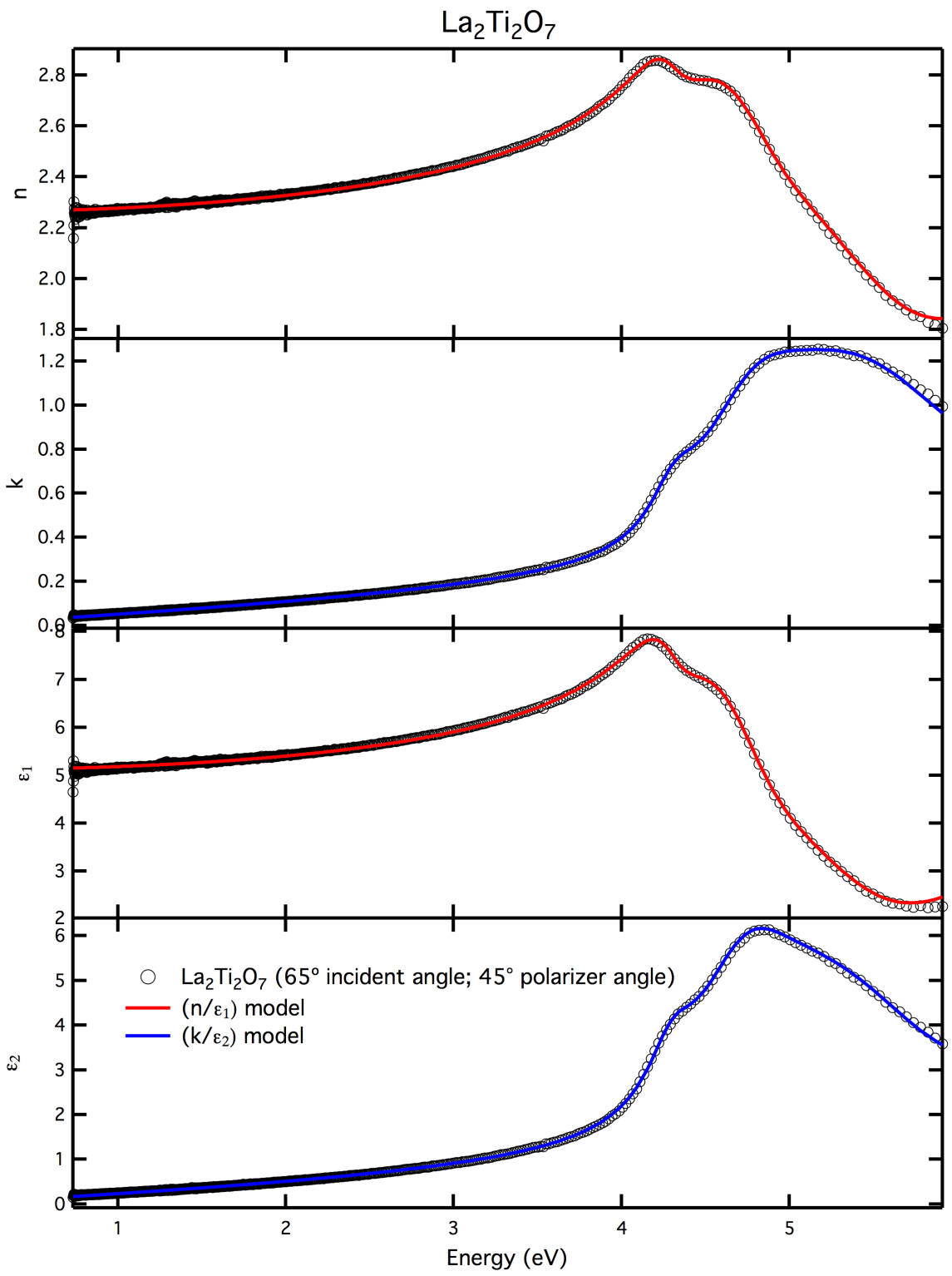

Figure S2.1 Optical constants (*n, k*) and dielectric constants (ε_1, ε_2) of $La_2Ti_2O_7$ substrate.

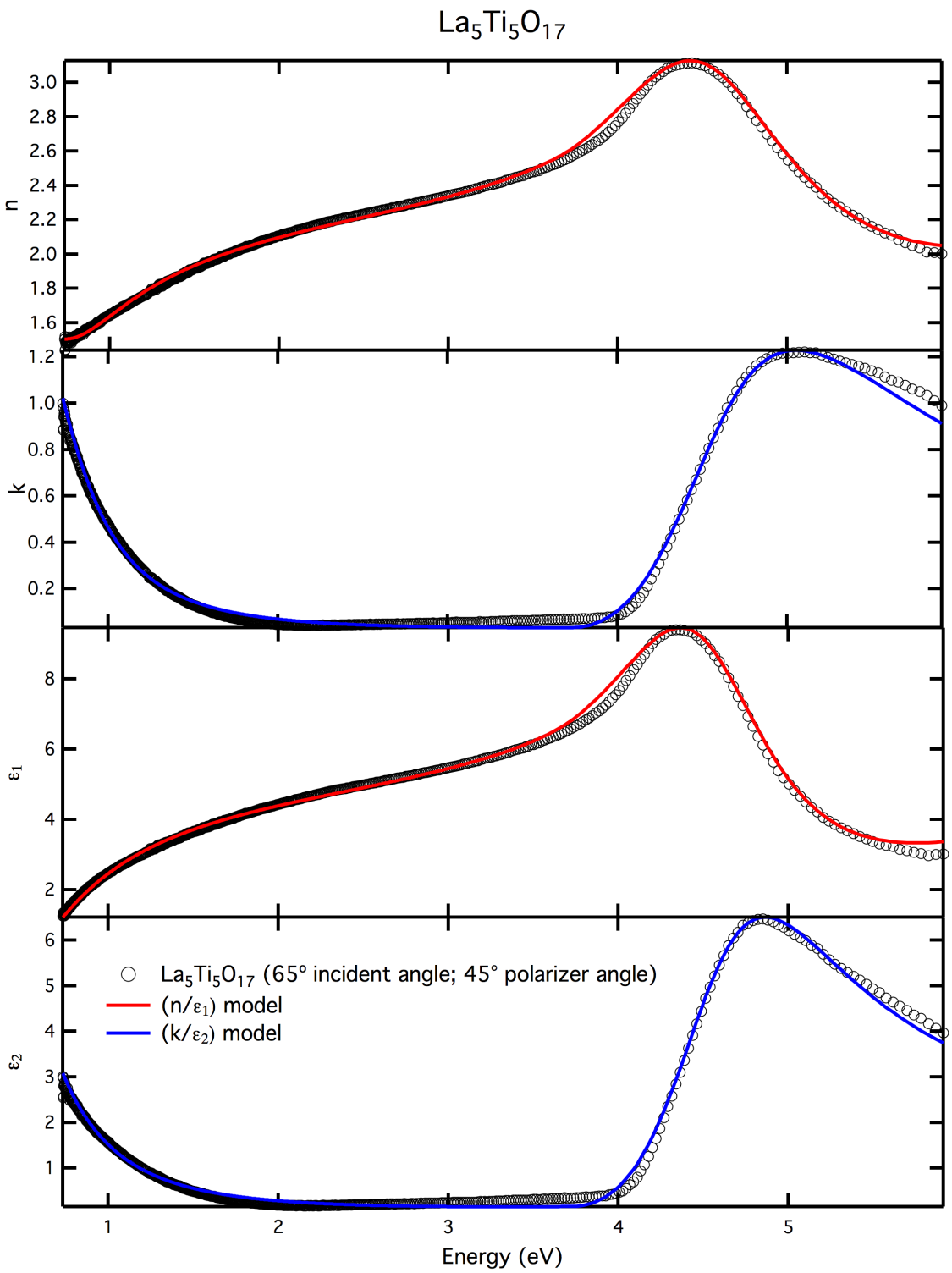

Figure S2.2 Optical constants (*n, k*) and dielectric constants (ε_1, ε_2) of $La_5Ti_5O_{17}$ substrate.

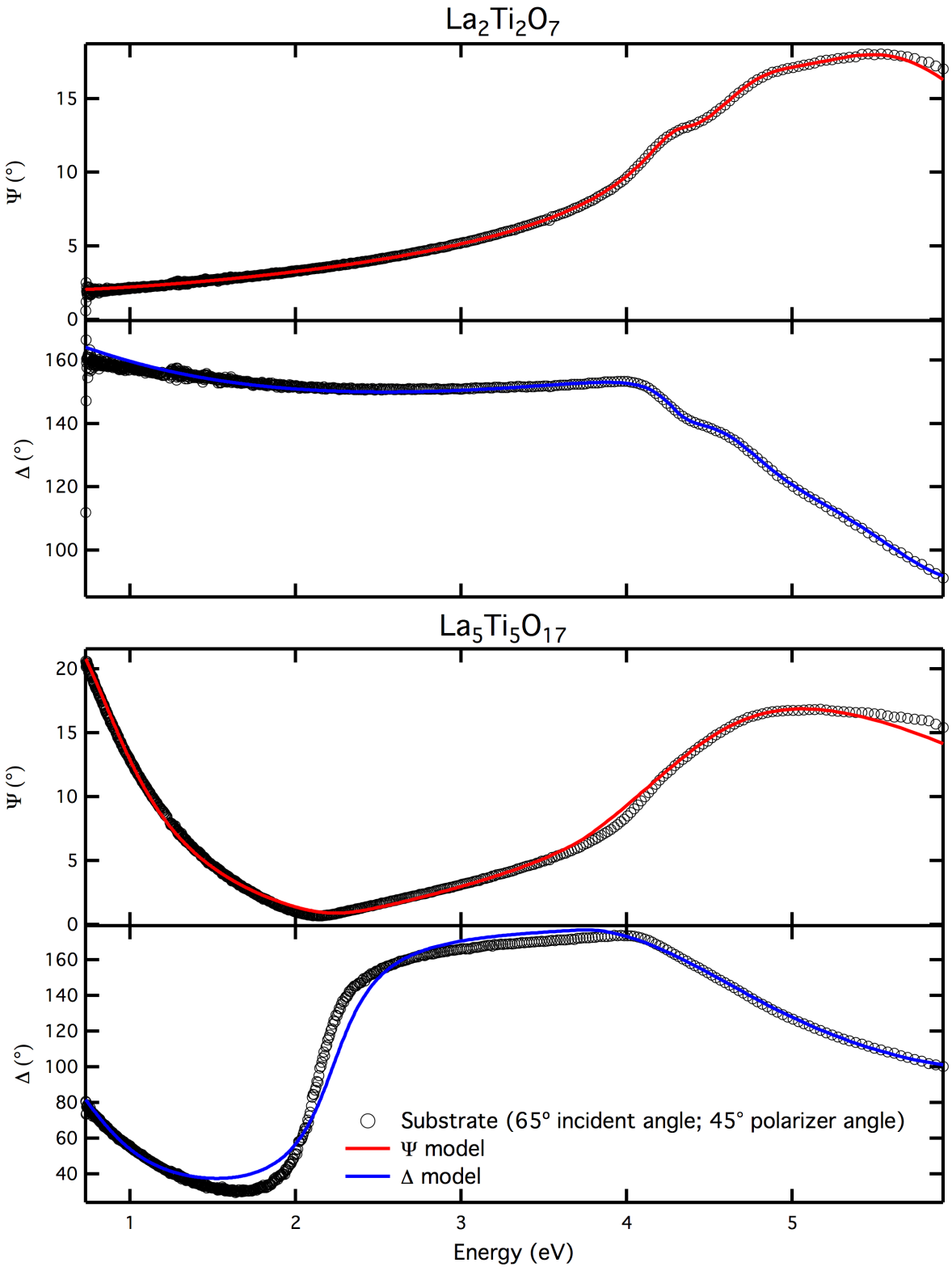

Figure S2.3 The quantities Ψ (°) and Δ (°) measured for the bare substrates $La_2Ti_2O_7$ and $La_5Ti_5O_{17}$.

Table S2.1

$La_5Ti_5O_{17}$ substrate fit parameters

Type	Amplitude	Center (eV)	Broadening (eV)	Gap (eV)
Lorentzian	21(2)	9.0(2)	0.88(8)	-
Tauc-Lorentz	180(14)	4.57(2)	1.2(3)	3.7(3)
Drude	5.36(4)	-	0.622(4)	-

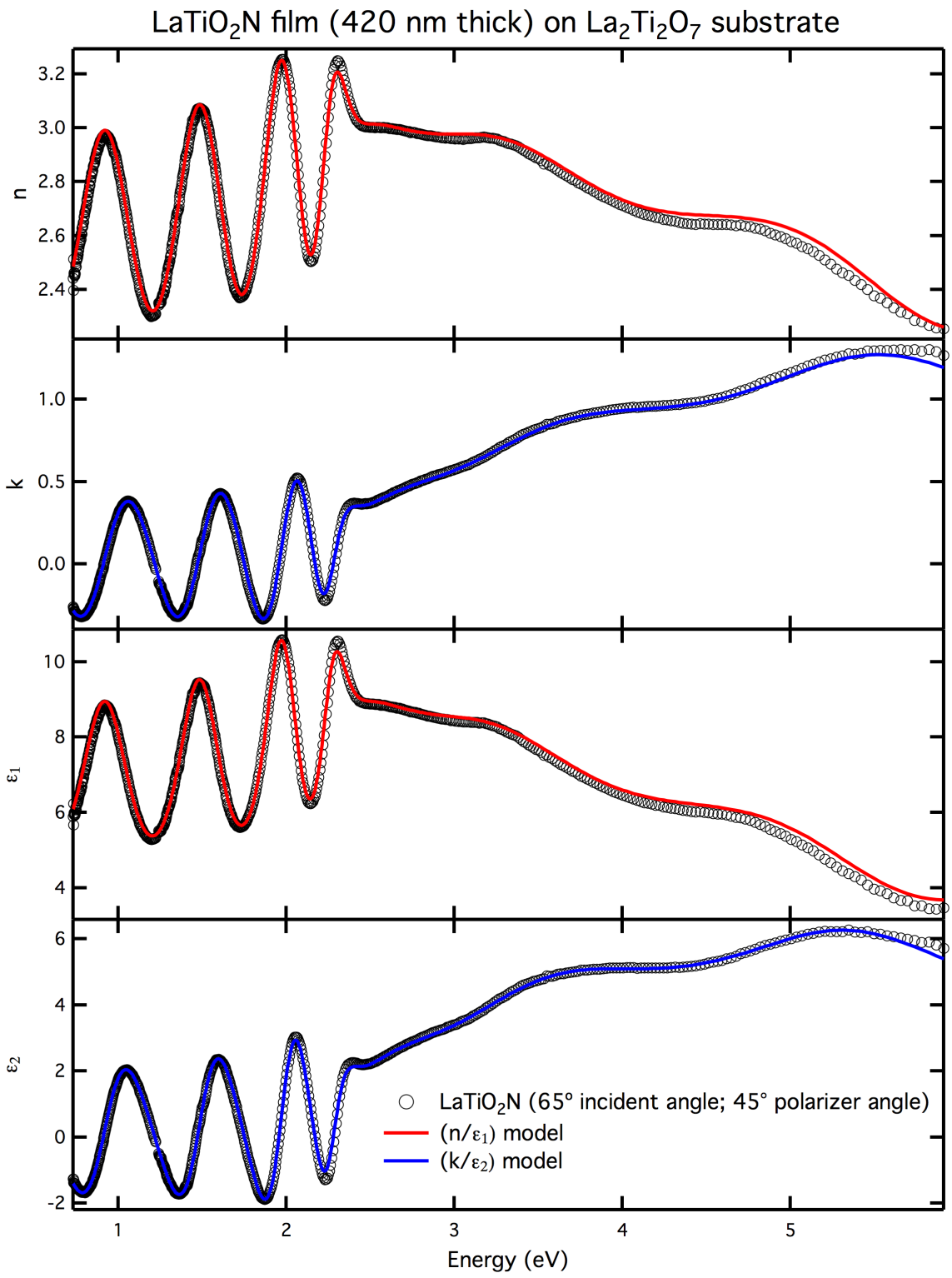
LaTiO2N film (420 nm thick) on La2Ti2O7 substrate
n
k
ε1
ε2
Energy (eV)
LaTiO2N (65° incident angle; 45° polarizer angle)
(n/ε1) model
(k/ε2) model

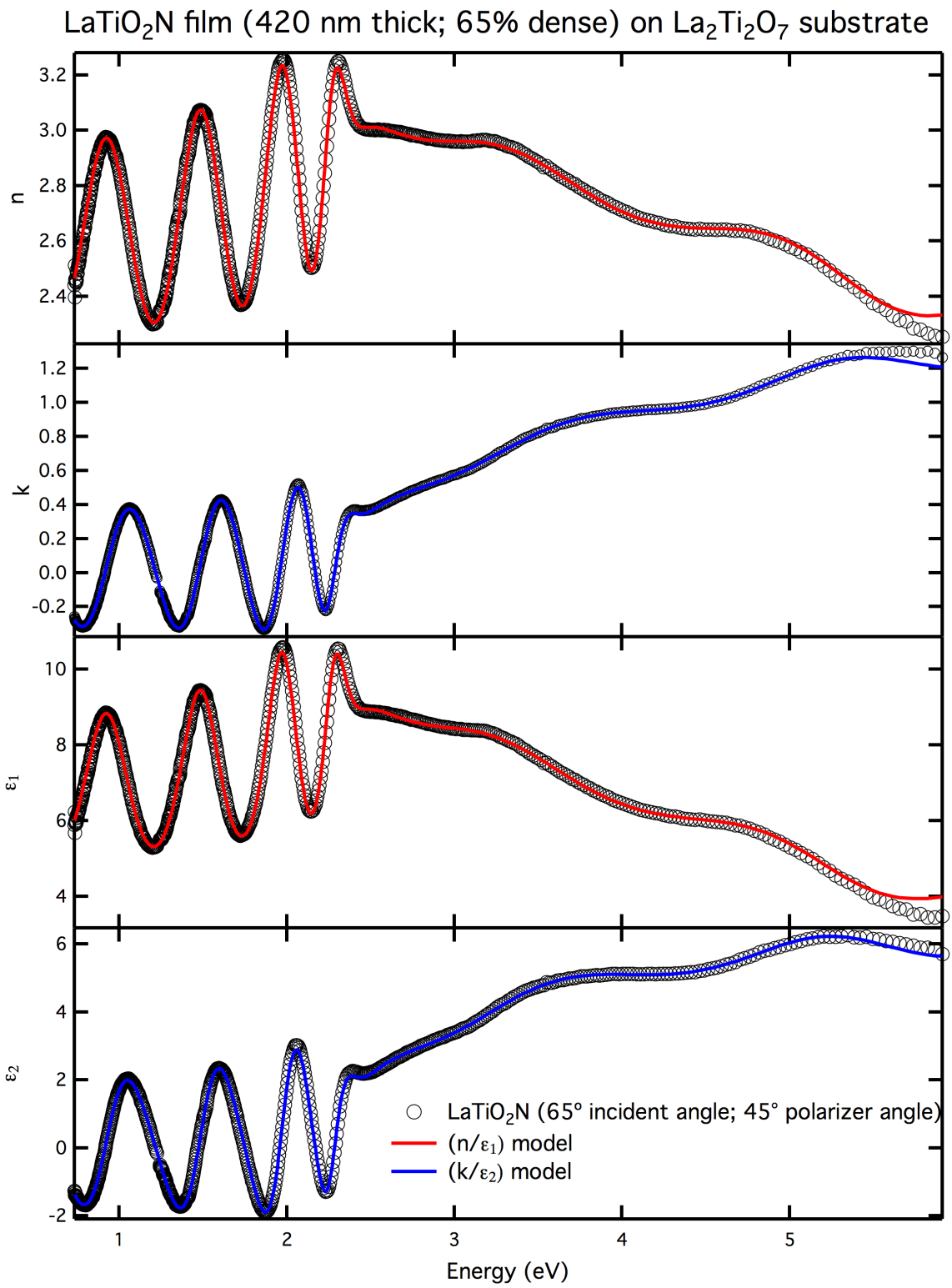

Figure S2.4 Optical constants (n,k) and the dielectric constants (ε_1, ε_2) of $LaTiO_2N$ on $La_2Ti_2O_7$ nitrided for 10 minutes under 80 mL/minute flowing NH_3 gas at 950° C. The data was fit using a fully dense model (top) and a 65% dense model (bottom).

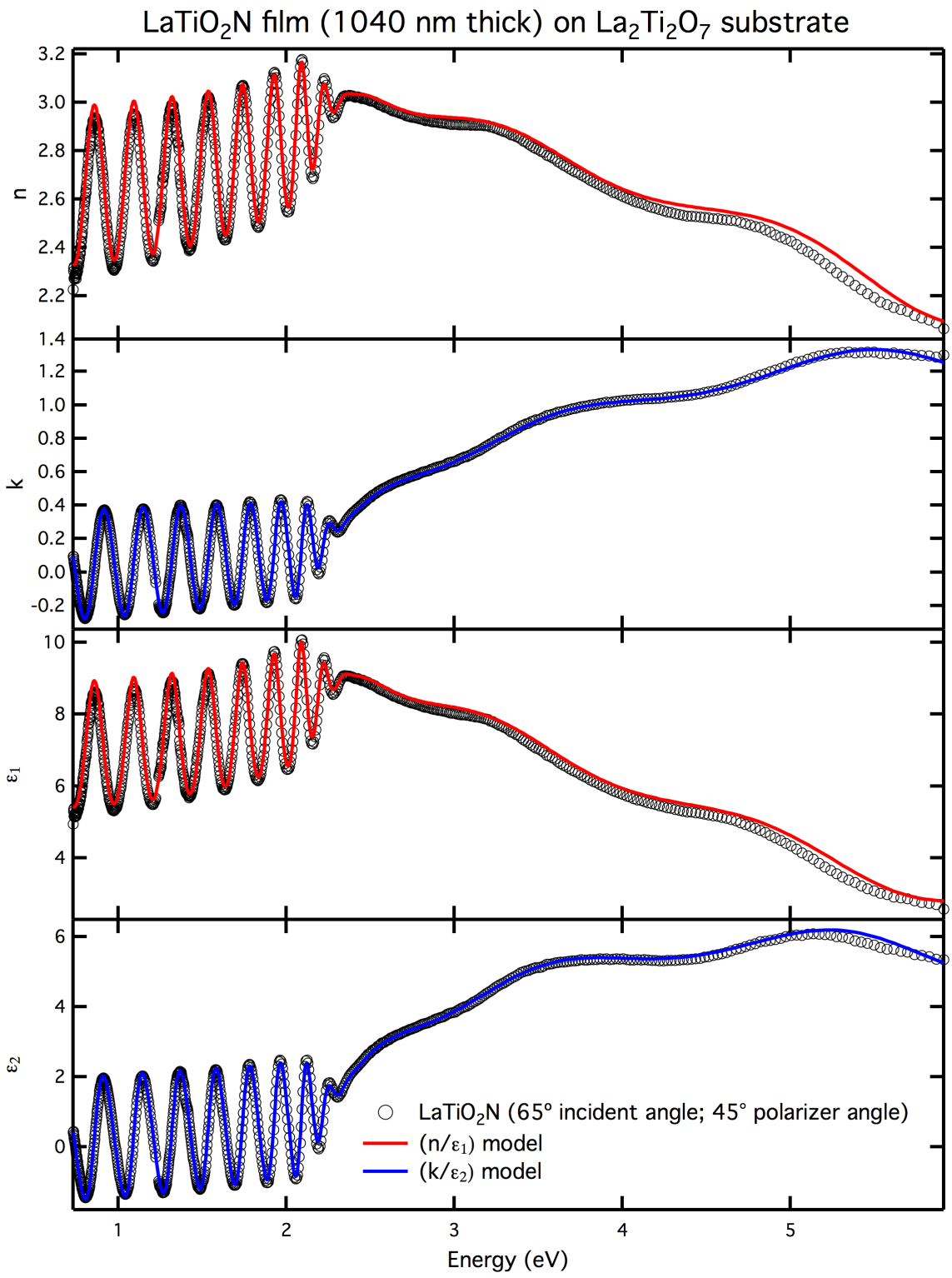
LaTiO2N film (1040 nm thick) on La2Ti2O7 substrate
n
k
ε1
ε2
LaTiO2N (65° incident angle; 45° polarizer angle)
(n/ε1) model
(k/ε2) model
Energy (eV)

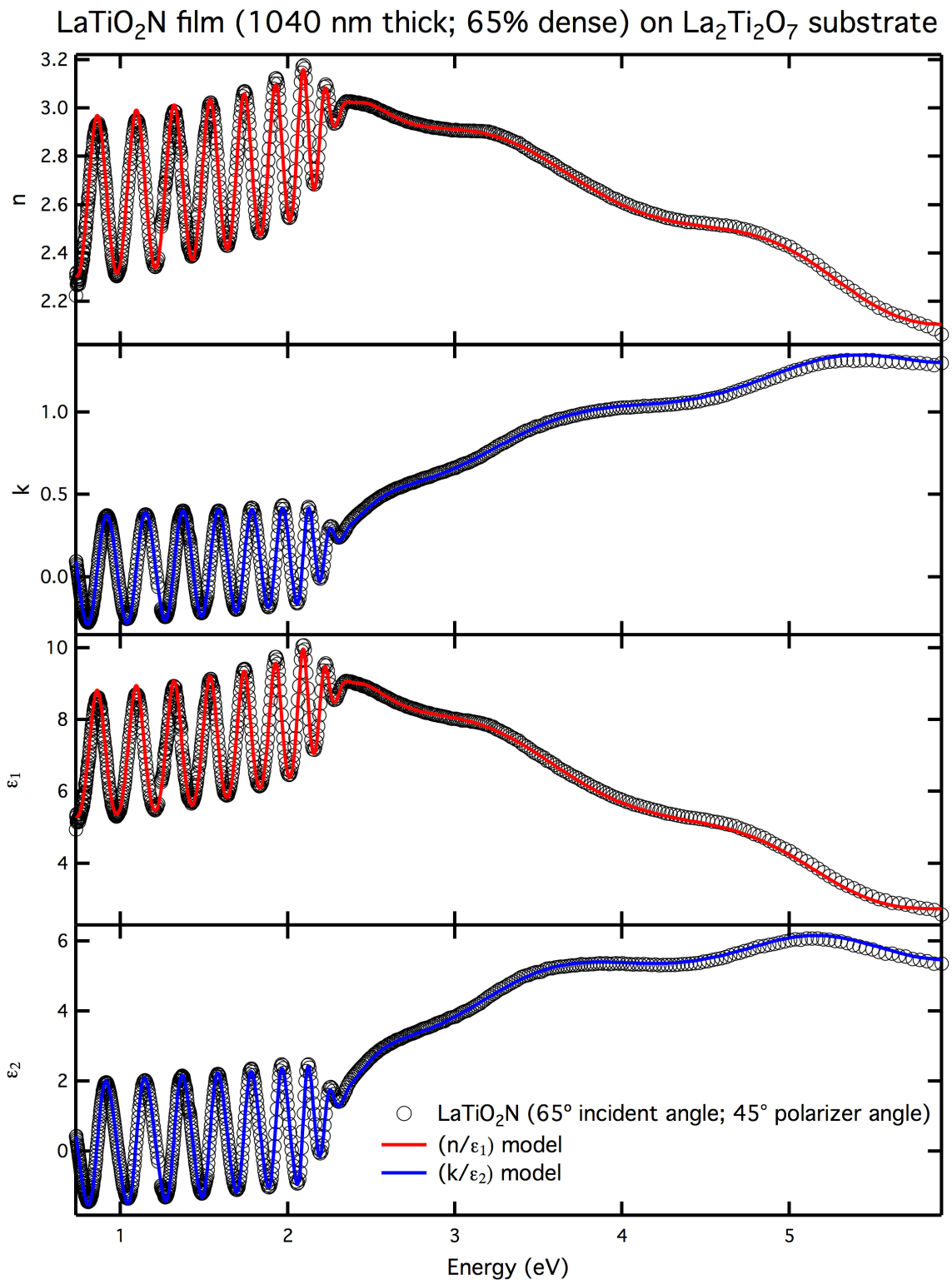

Figure S2.5 Optical constants (n,k) and the dielectric constants (ε_1, ε_2) of $LaTiO_2N$ on $La_2Ti_2O_7$ nitrided for 30 minutes under 80 mL/minute flowing NH_3 gas at 950° C. The data was fit using a fully dense model (top) and a 65% dense model (bottom).

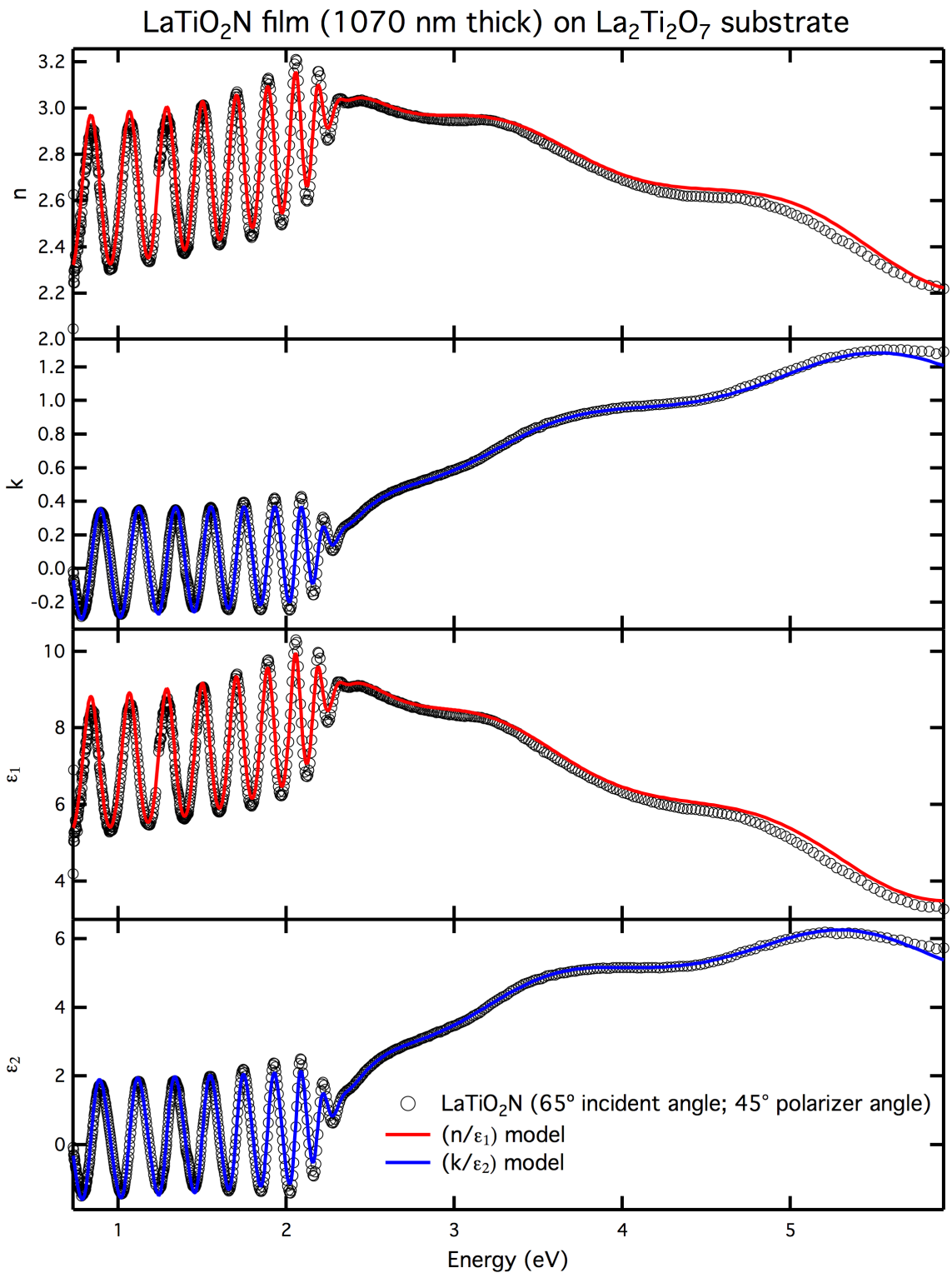
LaTiO2N film (1070 nm thick) on La2Ti2O7 substrate
n
k
ε1
ε2
Energy (eV)
LaTiO2N (65° incident angle; 45° polarizer angle)
(n/ε1) model
(k/ε2) model

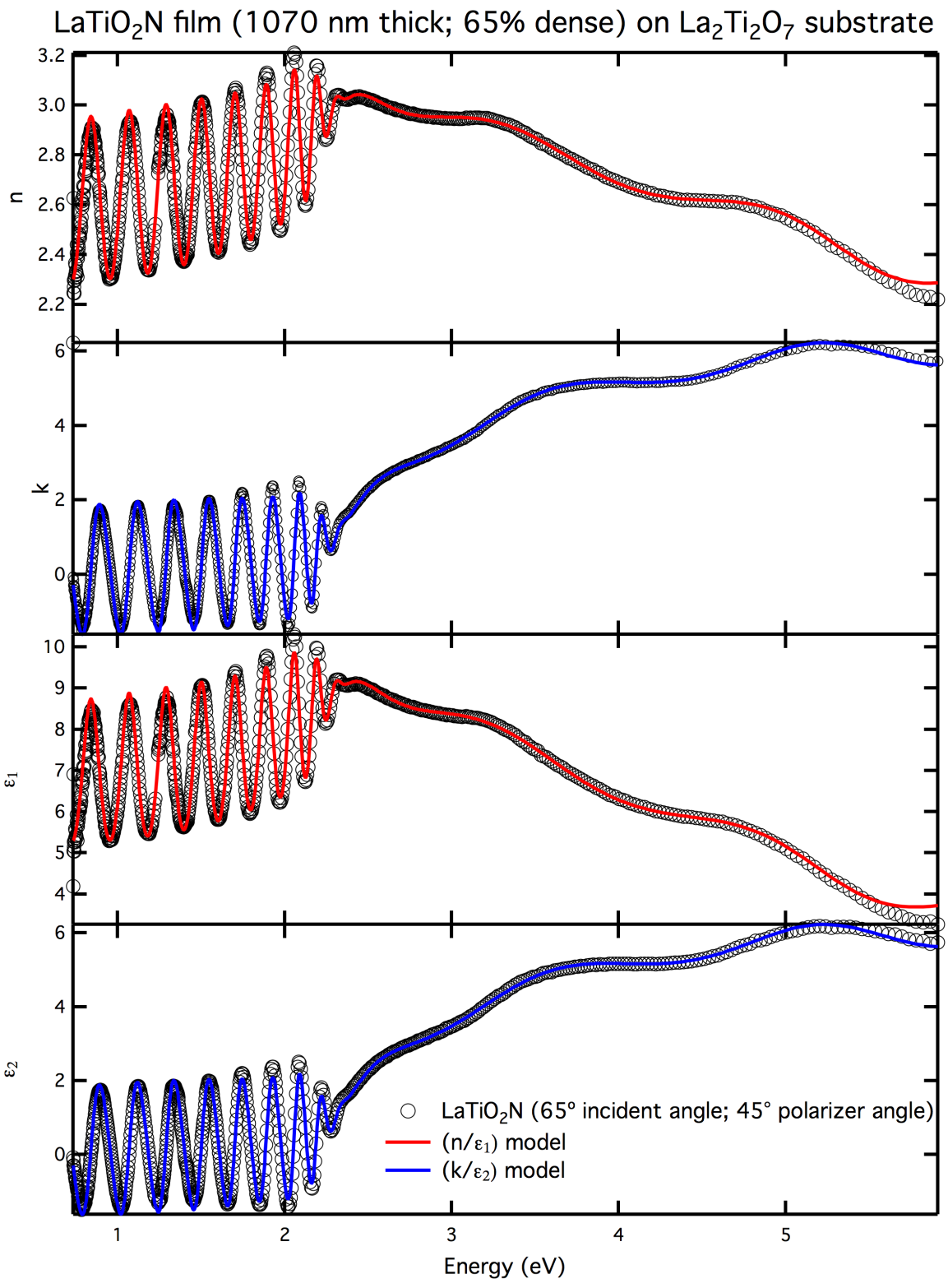

Figure S2.6 Optical constants (n,k) and the dielectric constants (ε_1, ε_2) of $LaTiO_2N$ on $La_2Ti_2O_7$ nitrided for 60 minutes under 80 mL/minute flowing NH_3 gas at 950° C. The data was fit using a fully dense model (top) and a 65% dense model (bottom).

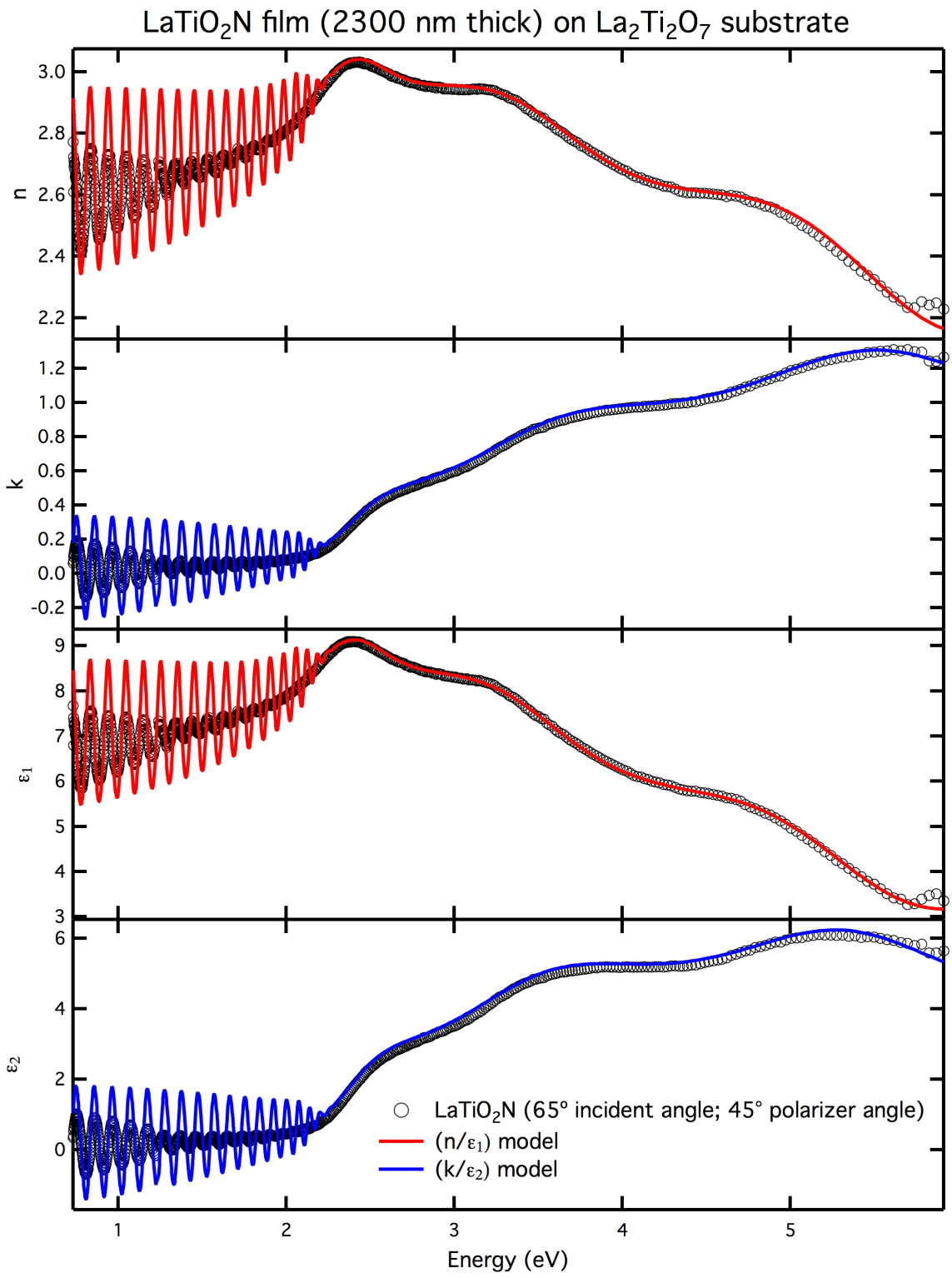
LaTiO2N film (2300 nm thick) on La2Ti2O7 substrate
n
k
ε1
ε2
LaTiO2N (65° incident angle; 45° polarizer angle)
(n/ε1) model
(k/ε2) model
Energy (eV)

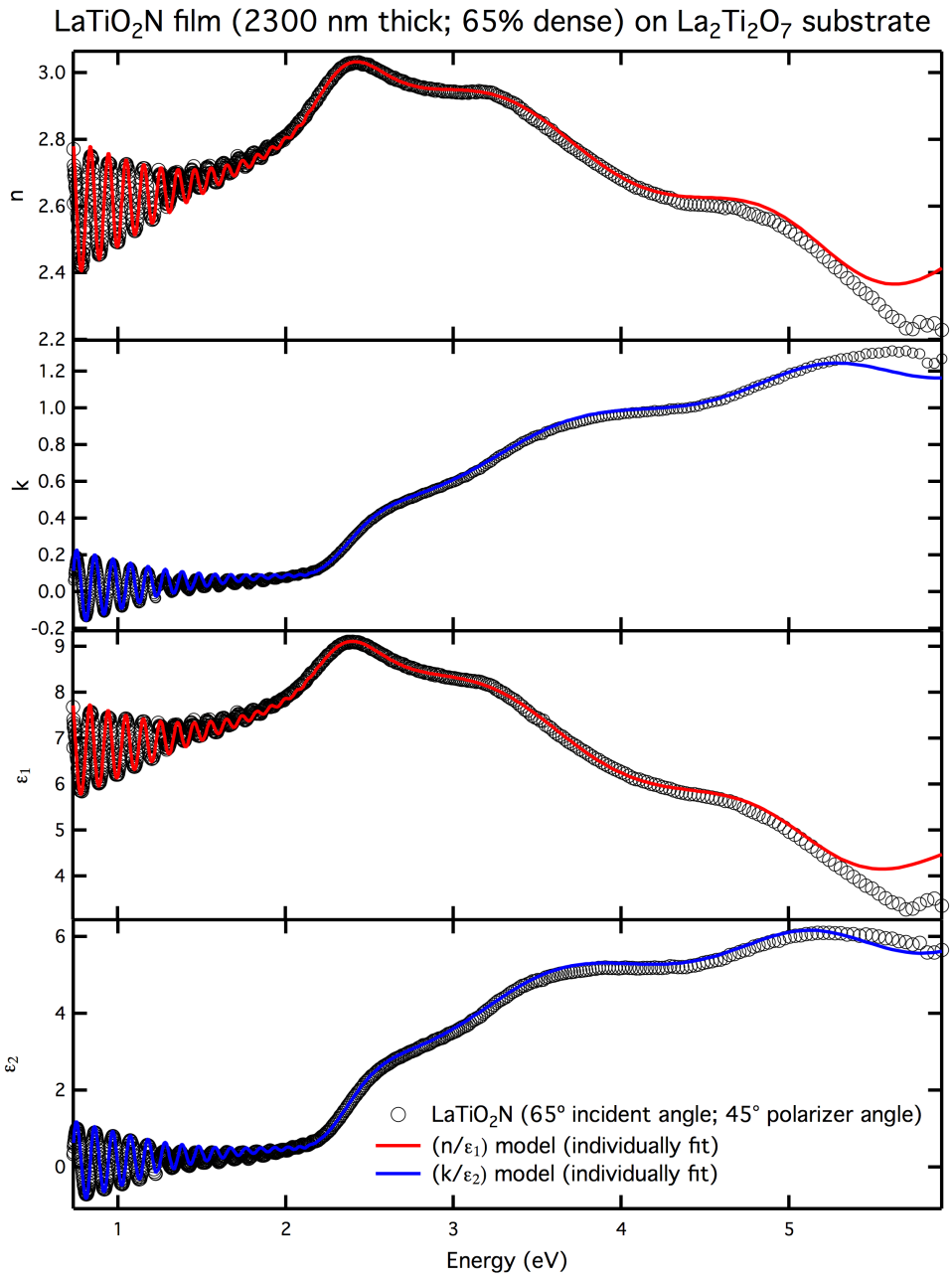

Figure S2.7 Optical constants (n,k) and the dielectric constants (ε_1, ε_2) of $LaTiO_2N$ on $La_2Ti_2O_7$ nitrided for 120 minutes under 80 mL/minute flowing NH_3 gas at 950° C. The data was fit using a fully dense model (top) and a 65% dense model (bottom). These figures were made by simultaneously fitting the data collected on this sample above 2.5 eV and all the other data collected on the other samples, then plotting the fit over the entire data range. This was done because an absorption artifact near the band edge of the thickest sample, believed to be due to surface effects was unduly affecting the fit. A separate fit was done using only the thickest sample for comparison.

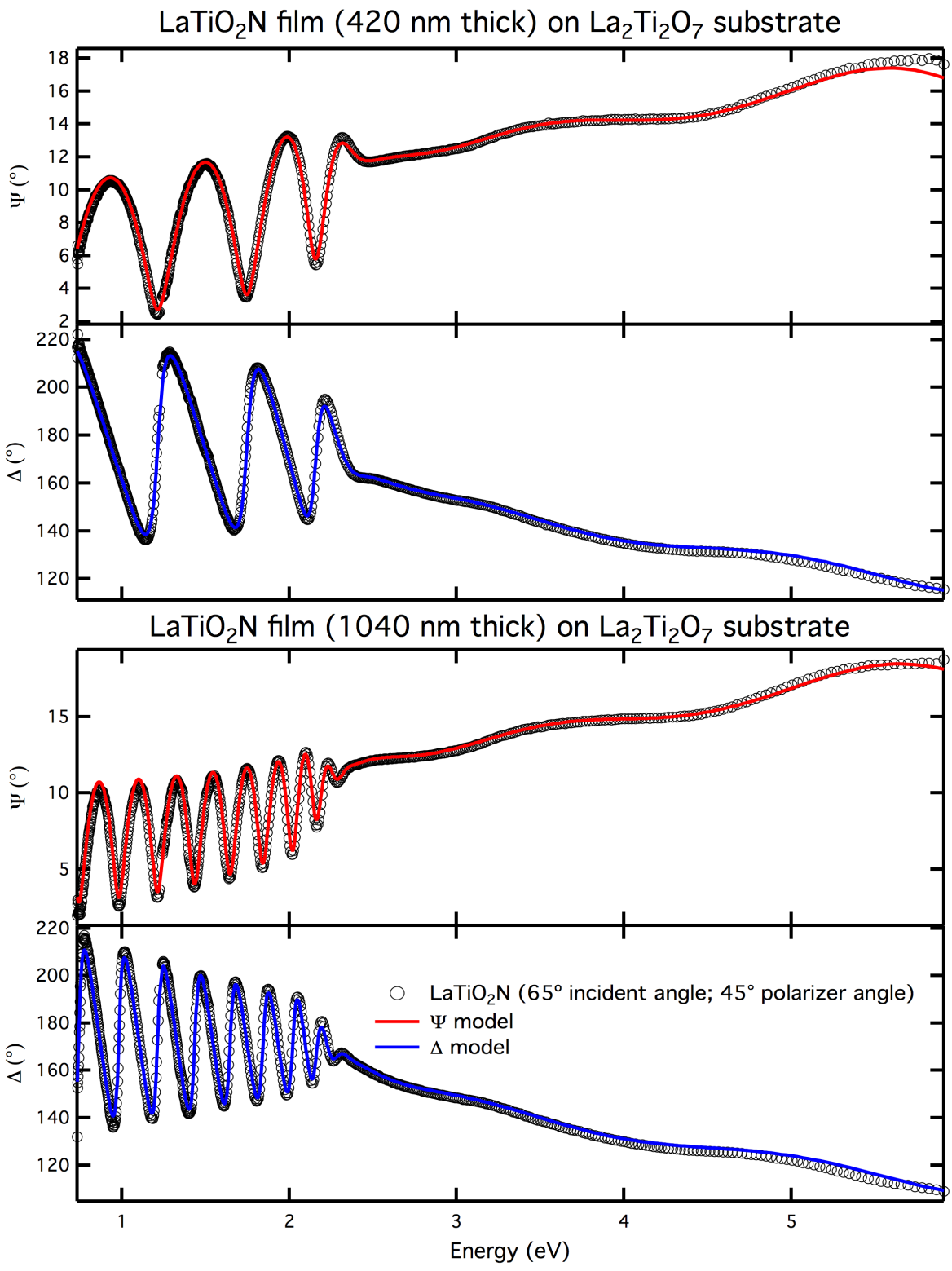
LaTiO2N film (420 nm thick) on La2Ti2O7 substrate
Ψ (°)
Δ (°)
LaTiO2N film (1040 nm thick) on La2Ti2O7 substrate
LaTiO2N (65° incident angle; 45° polarizer angle)
Ψ model
Δ model
Energy (eV)

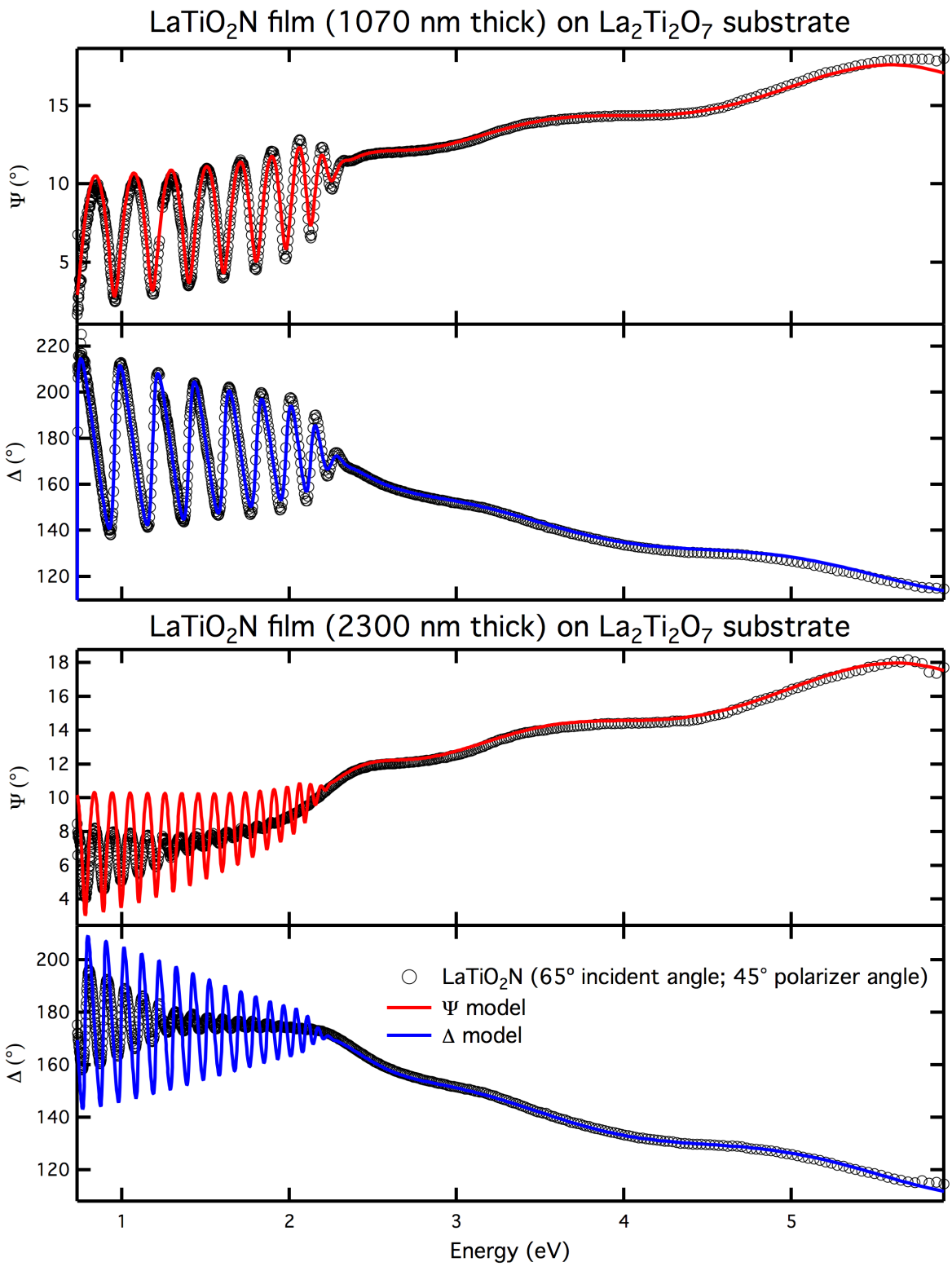
LaTiO2N film (1070 nm thick) on La2Ti2O7 substrate
Ψ (°)
Δ (°)
LaTiO2N film (2300 nm thick) on La2Ti2O7 substrate
LaTiO2N (65° incident angle; 45° polarizer angle)
Ψ model
Δ model
Energy (eV)

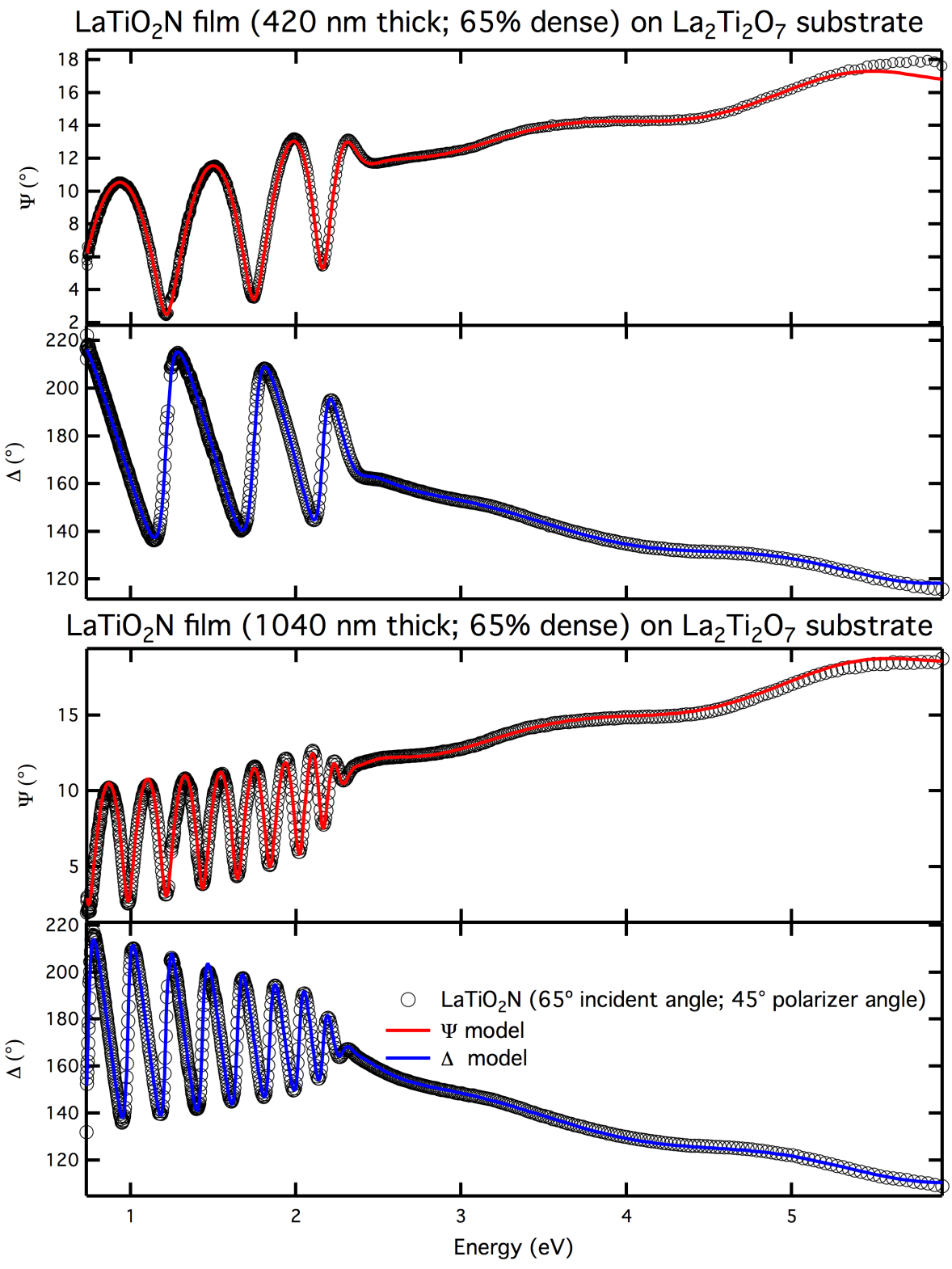
LaTiO2N film (420 nm thick; 65% dense) on La2Ti2O7 substrate
Ψ (°)
Δ (°)
LaTiO2N film (1040 nm thick; 65% dense) on La2Ti2O7 substrate
Ψ (°)
Δ (°)
LaTiO2N (65° incident angle; 45° polarizer angle)
Ψ model
Δ model
Energy (eV)

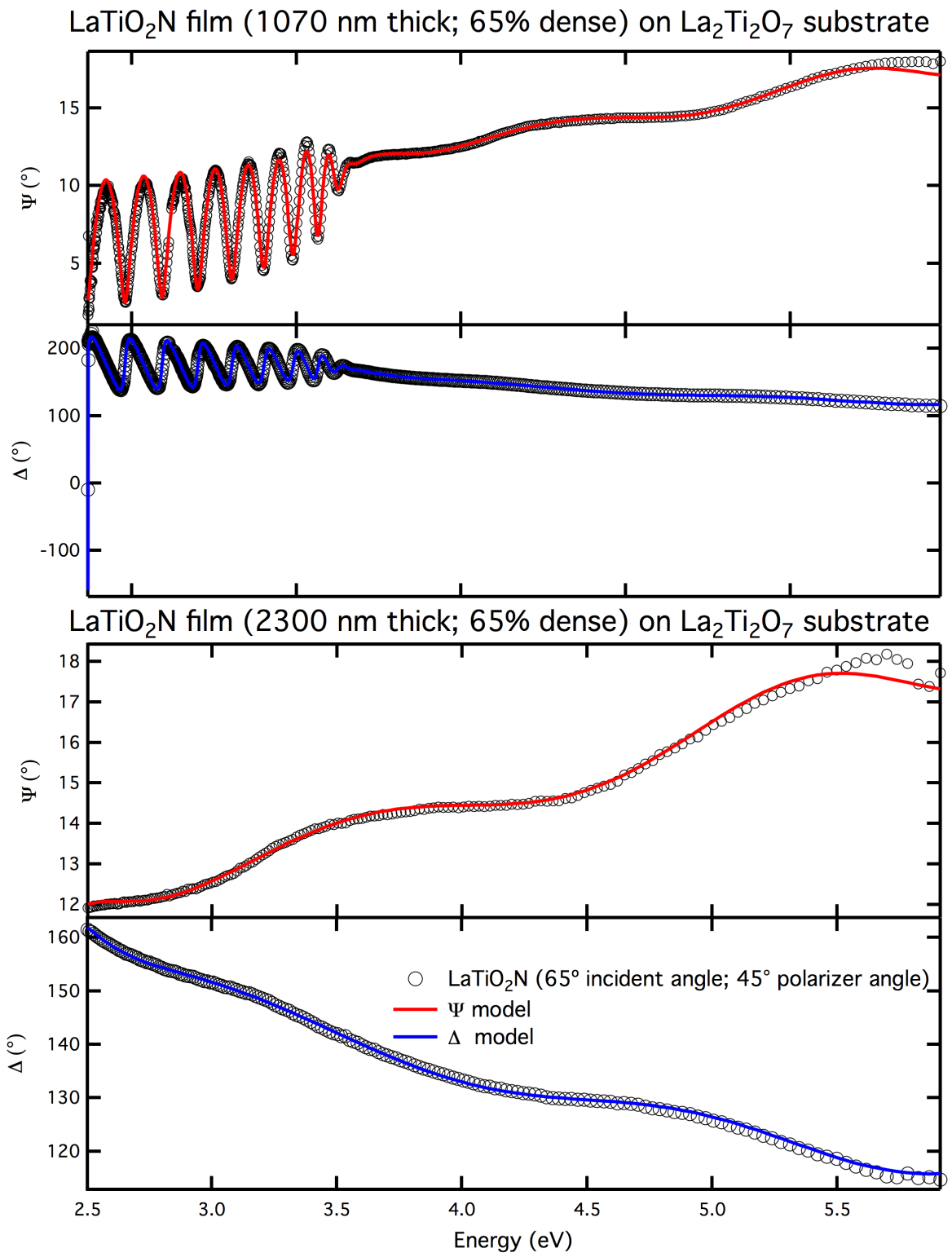

Figure S2.8 The quantities Ψ (°) and Δ (°) measured for the $LaTiO_2N$ samples grown on the $La_2Ti_2O_7$ substrate (both 100% dense and 65% dense models).

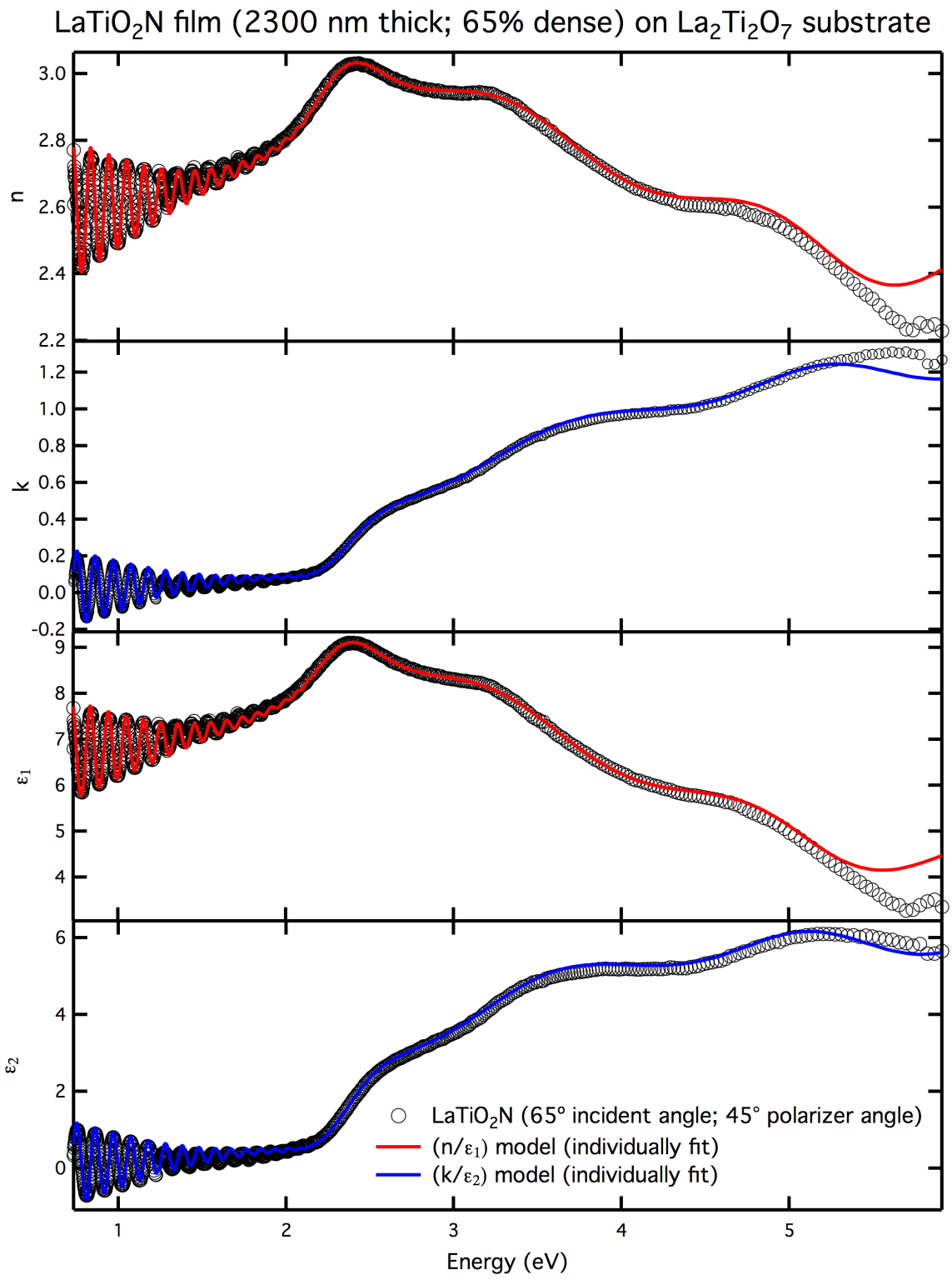
LaTiO2N film (2300 nm thick; 65% dense) on La2Ti2O7 substrate
n
k
ε1
ε2
Energy (eV)
LaTiO2N (65° incident angle; 45° polarizer angle)
(n/ε1) model (individually fit)
(k/ε2) model (individually fit)

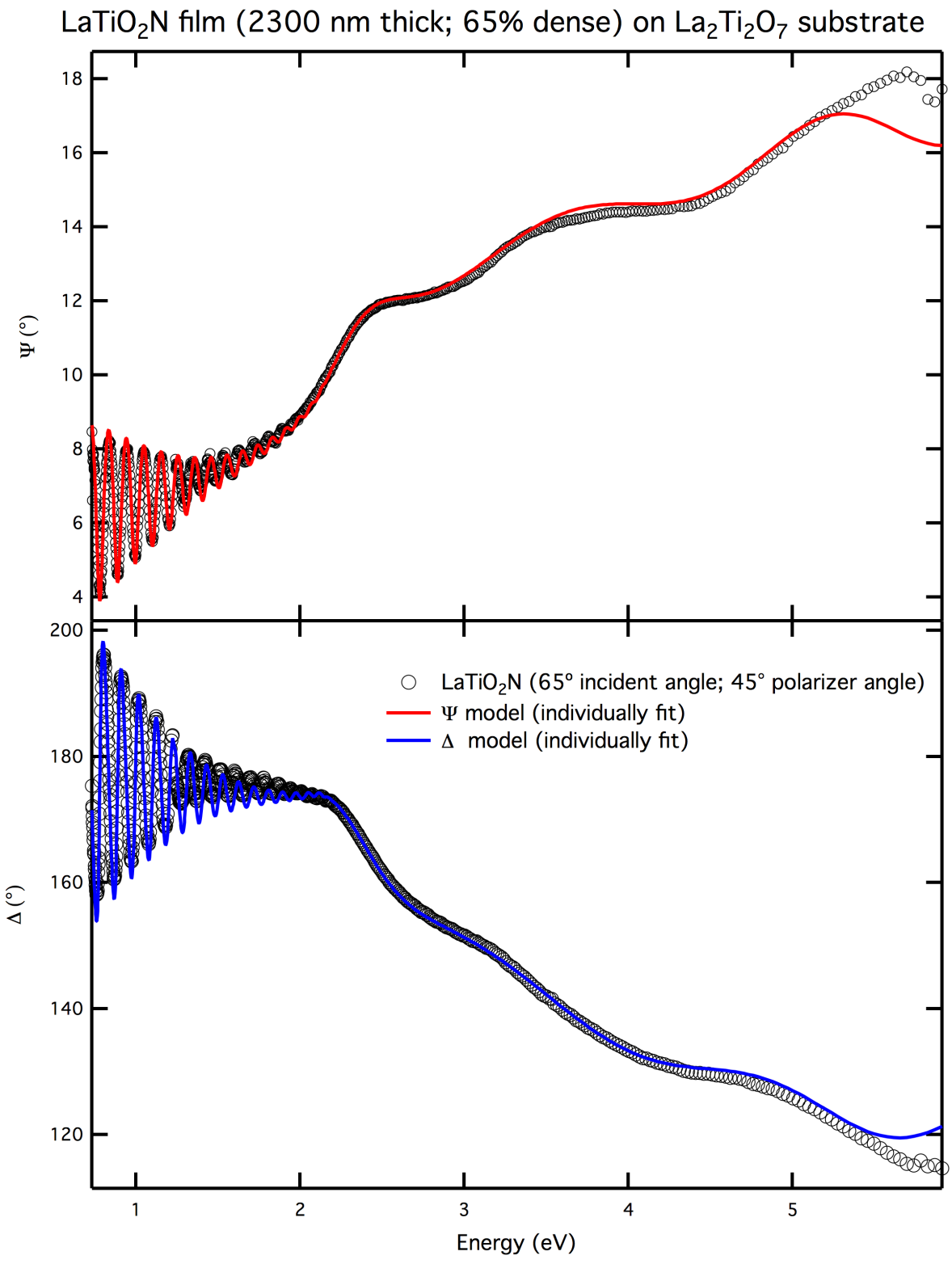

Figure S2.9 Optical constants (n,k), the dielectric constants (ε_1, ε_2) and the quantities Ψ (°) and Δ (°) of $LaTiO_2N$ on $La_2Ti_2O_7$ nitrided for 120 minutes under 80 mL/minute flowing NH_3 gas at 950° C. The data was fit independently from the other data using a 65% dense model.

Table S2.2 Fit parameters obtained using only data collected on the $LaTiO_2N$ sample nitride for 120 min. under flowing NH_3 gas at 950° C. 165% dense model.

$LaTiO_2N$ Film on $La_2Ti_2O_7$ substrate, thickness= 22920(30) Å

Type	Amplitude	Center (eV)	Broadening (eV)	Gap (eV)
Gaussian	19(5)	7.5(2)	2(1)	-
Gaussian	1.3(2)	2.9(5)	3.0(5)	-
Tauc-Lorentz	86(20)	2.39(3)	0.71(9)	2(1)
Tauc-Lorentz	80(20)	3.57(5)	2.0(3)	2(1)
Tauc-Lorentz	37(40)	5.2(2)	1.7(5)	2(1)

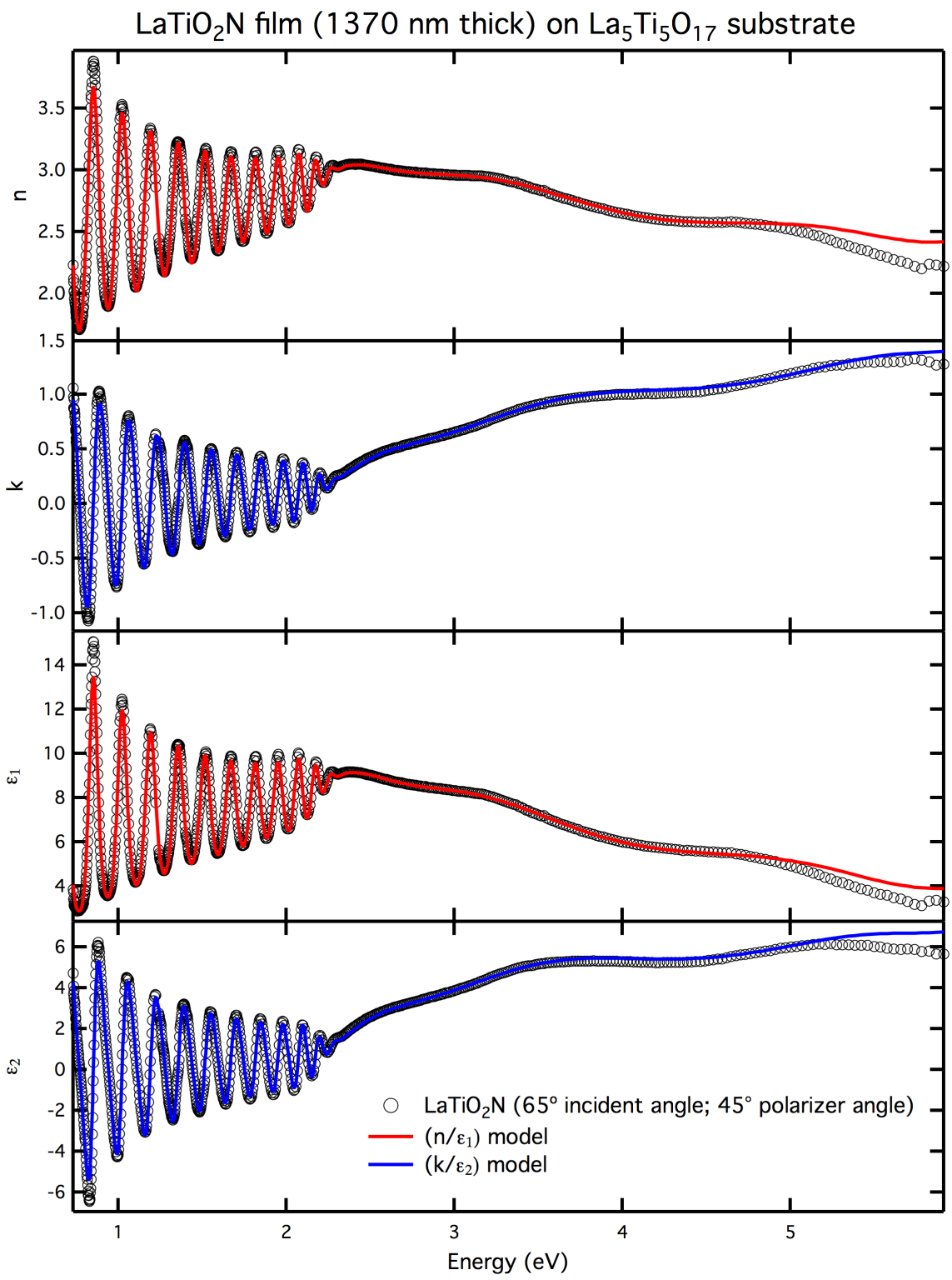
LaTiO2N film (1370 nm thick) on La5Ti5O17 substrate
n
k
ε1
ε2
Energy (eV)
LaTiO2N (65° incident angle; 45° polarizer angle)
(n/ε1) model
(k/ε2) model

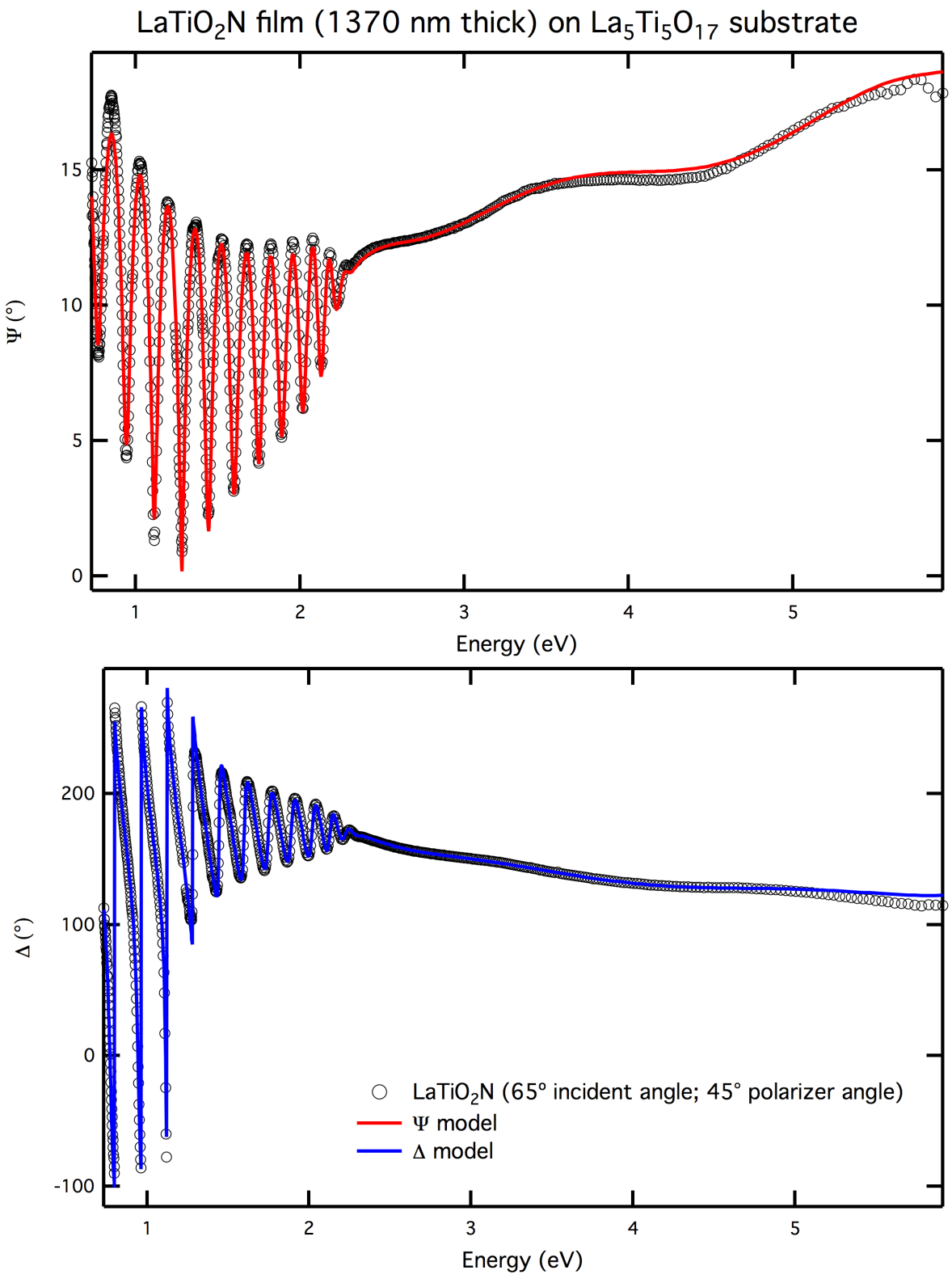

Figure S2.10 Optical constants (n,k), the dielectric constants (ε_1, ε_2) and the quantities Ψ (°) and Δ (°) of $LaTiO_2N$ on $La_5Ti_5O_{17}$ nitrided for 60 minutes under 80 mL/minute flowing NH_3 gas at

950° C. The data was fit independently from the other data. Because the fit of the $La_5Ti_5O_{17}$ data was poor the substrate's Drude oscillator was allowed to refine with the $LaTiO_2N$ film model.

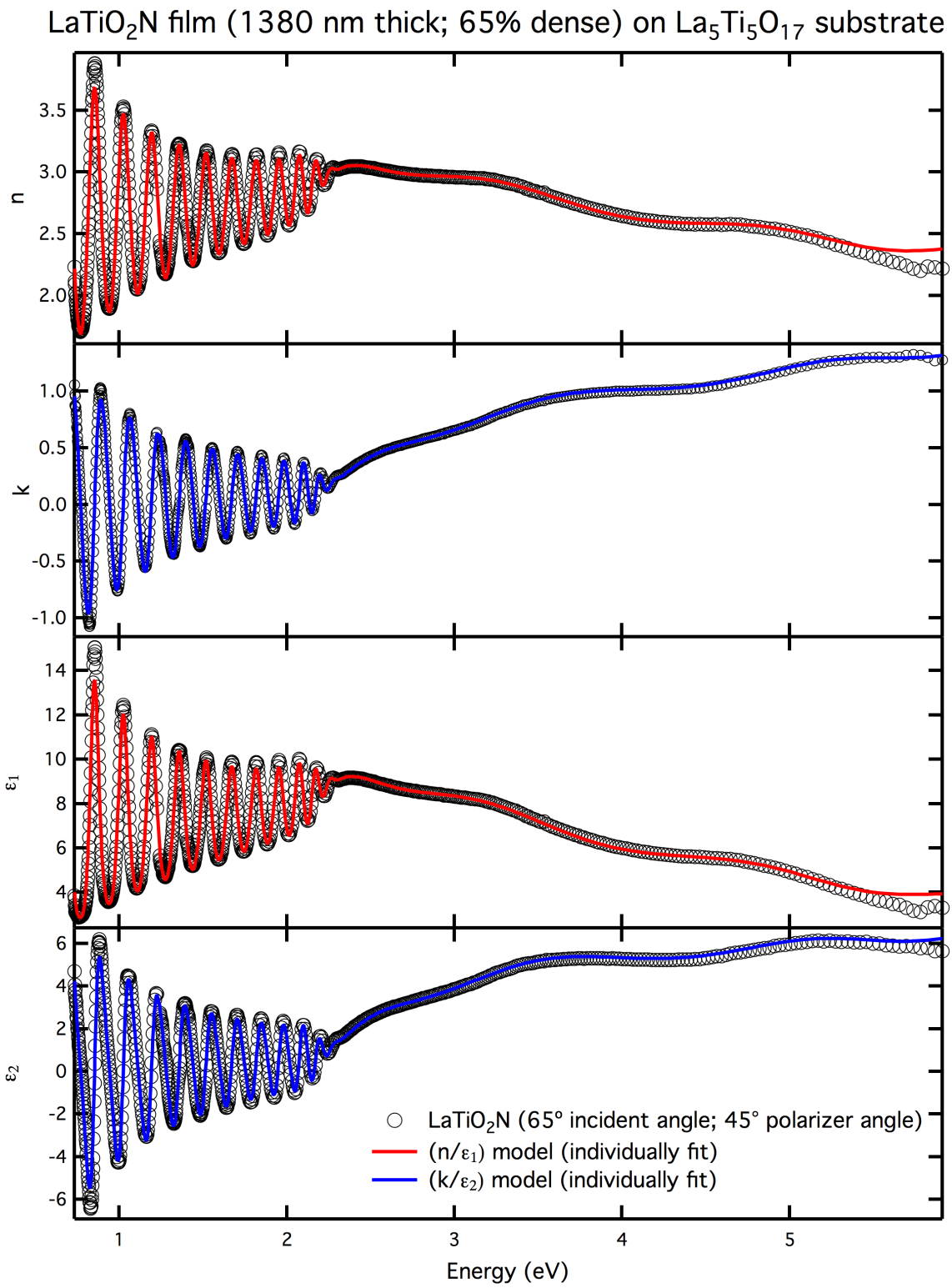
LaTiO2N film (1380 nm thick; 65% dense) on La5Ti5O17 substrate
n
k
ε1
ε2
Energy (eV)
LaTiO2N (65° incident angle; 45° polarizer angle)
(n/ε1) model (individually fit)
(k/ε2) model (individually fit)

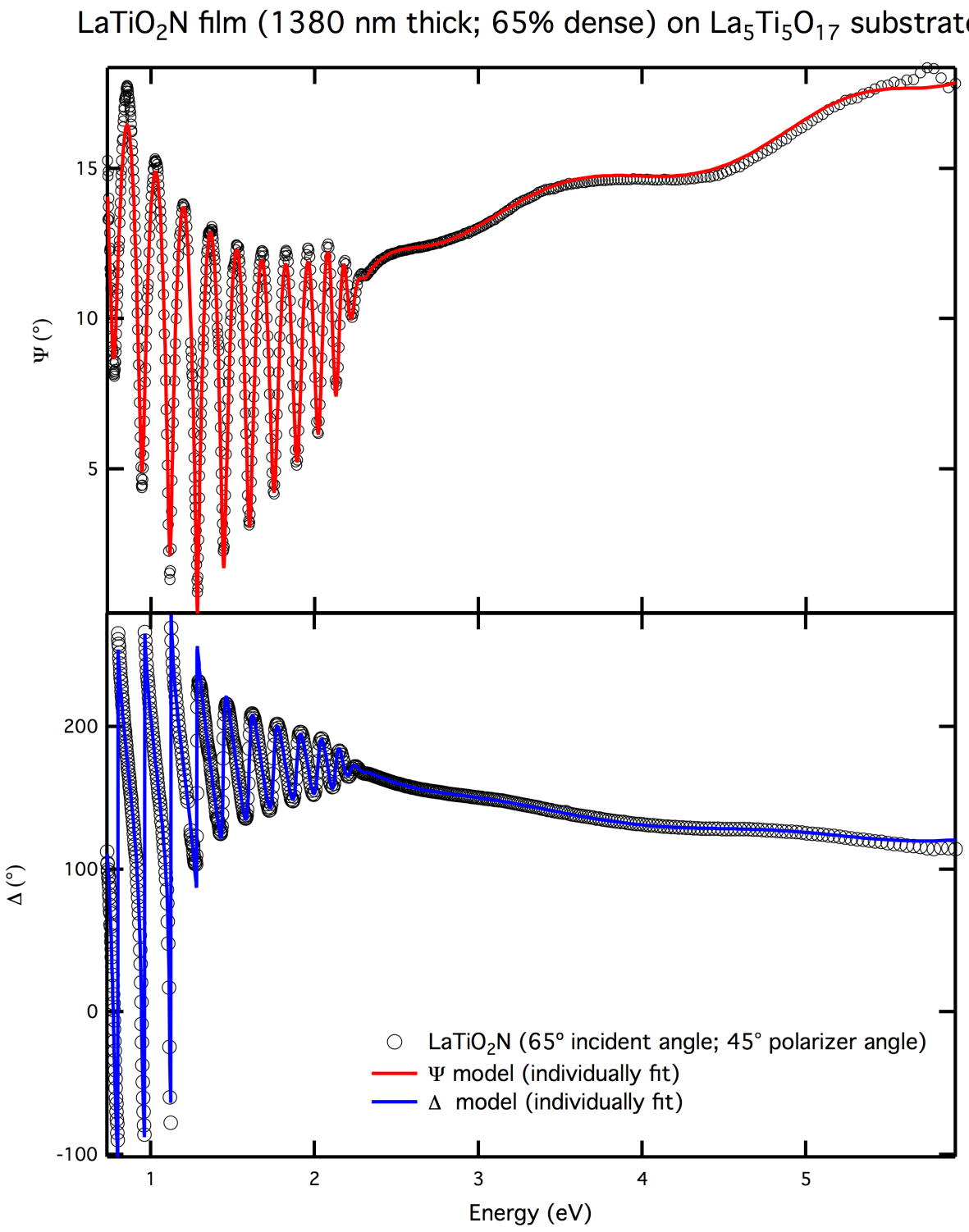

Figure S2.11 Optical constants (n,k), the dielectric constants (ε_1, ε_2) and the quantities Ψ (°) and Δ (°) of $LaTiO_2N$ on $La_5Ti_5O_{17}$ nitrided for 60 minutes under 80 mL/minute flowing NH_3 gas at 950° C. The data was fit independently from the other data using a 65% dense model.

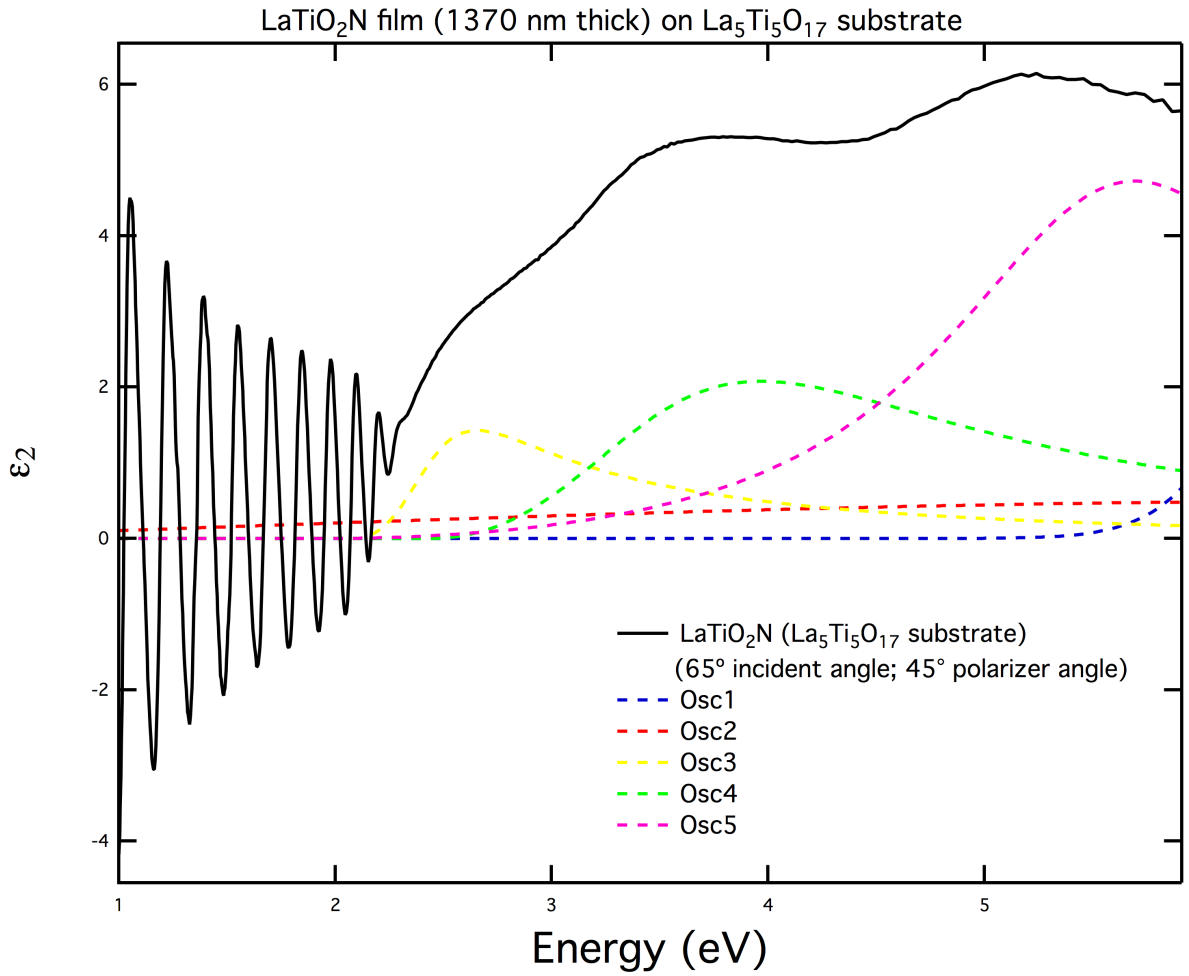

Figure S2.12 Oscillators used to model the optical response of $LaTiO_2N$ on $La_5Ti_5O_{17}$ and the orbital assignment of visible light absorption transitions.

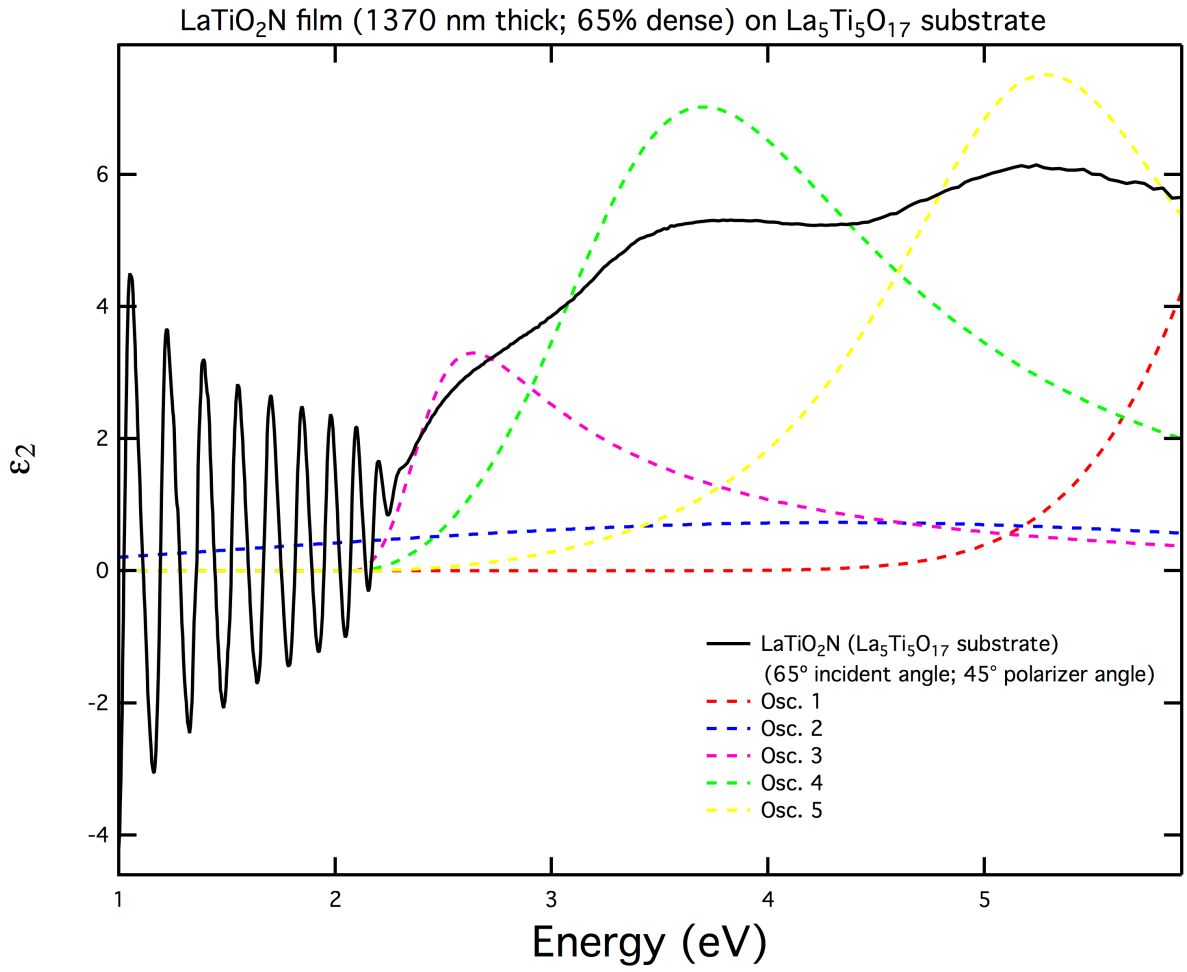

Figure S2.13 Oscillators used to model the optical response of $LaTiO_2N$ on $La_5Ti_5O_{17}$ and the orbital assignment of visible light absorption transitions. 65% dense model.

Table S2.3 Fit parameters to data collected on the $LaTiO_2N$ grown on a $La_5Ti_5O_7$ substrate, nitrided for 60 min. under flowing NH_3 gas at 950° C.

Amorphous surface layer

Thickness (Å)	5.9(4)
N ($1/cm^3$)	1.5811×10^{22} (fixed)
μ	0.3(1)
m*	1
ρ (Ω•cm)	0.0013009
τ (fs)	0.17254

$LaTiO_2N$ Film on $La_5Ti_5O_{17}$ substrate

Type	Amplitude	Center (eV)	Broadening (eV)	Gap (eV)
Gaussian	10(10)	7.3(4)	1(1)	-
Gaussian	0.5(3)	7(5)	10(10)	-
Tauc-Lorentz	35(11)	2.41(4)	0.7(1)	2.09(2)
Tauc-Lorentz	40(14)	5.54(7)	2.1(4)	2.04(3)
Tauc-Lorentz	20(20)	5.7(6)	2(1)	1.98(3)

Refined $La_5Ti_5O_{17}$ Drude model

Amplitude	Broadening (eV)
3.49(9)	1.7(1)

Table S2.4 Fit parameters to data collected on the $LaTiO_2N$ grown on a $La_5Ti_5O_7$ substrate, nitrided for 60 min. under flowing NH_3 gas at 950° C. 1-(1/1.35) void space model.

Amorphous surface layer

Thickness (Å)	4.9(3)
N ($1/cm^3$)	$1.5811x10^{22}$ (fixed)
μ	0.5(1)
m*	1
ρ (Ω•cm)	0.0013009
τ (fs)	0.17254

$LaTiO_2N$ Film on $La_5Ti_5O_{17}$ substrate

Type	Amplitude	Center (eV)	Broadening (eV)	Gap (eV)
Gaussian	22(6)	7.6(2)	2.1(7)	-
Gaussian	0.7(4)	4(2)	5(3)	-
Tauc-Lorentz	81(10)	2.40(1)	0.68(6)	2(5)
Tauc-Lorentz	79(17)	3.48(4)	1.9(3)	2(5)
Tauc-Lorentz	39(20)	5.3(2)	1.9(5)	2(5)

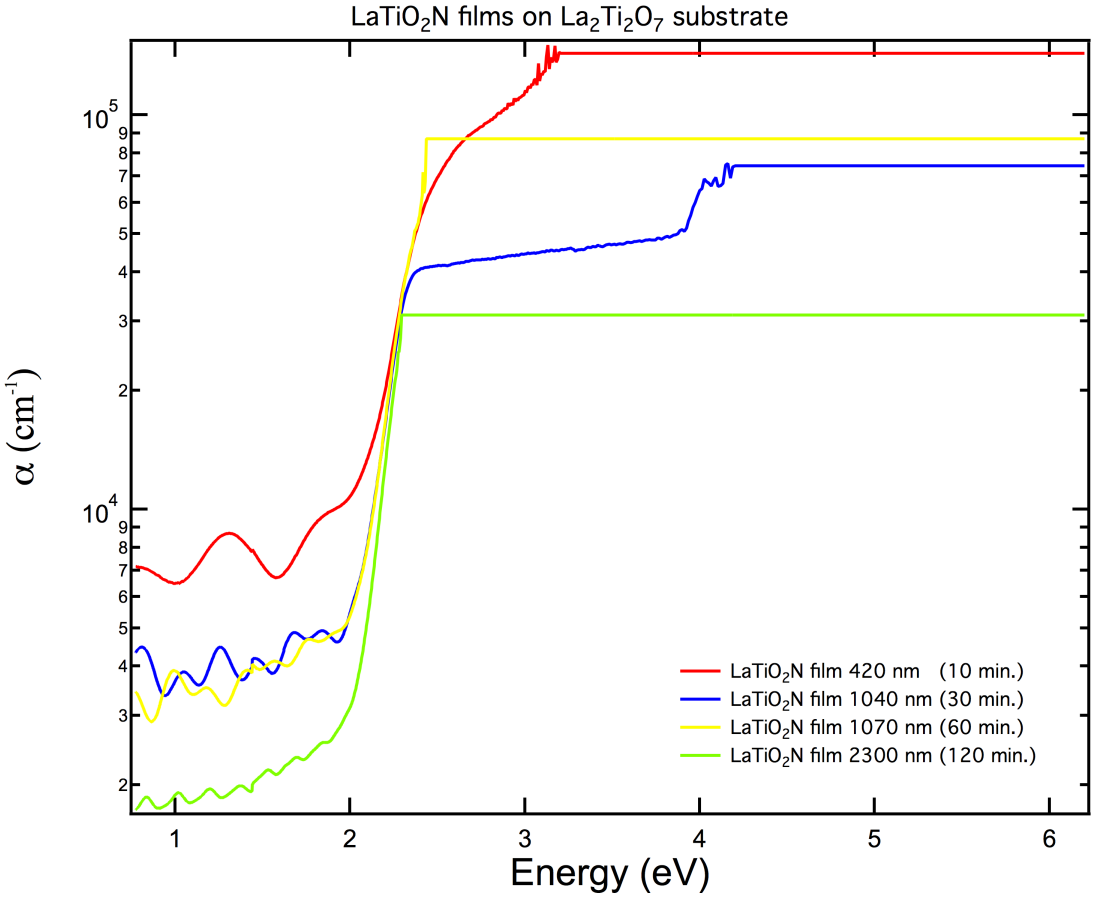

Figure S2.14 The raw transmission data collected on $LaTiO_2N$ films grown on $La_2Ti_2O_7$ substrates.

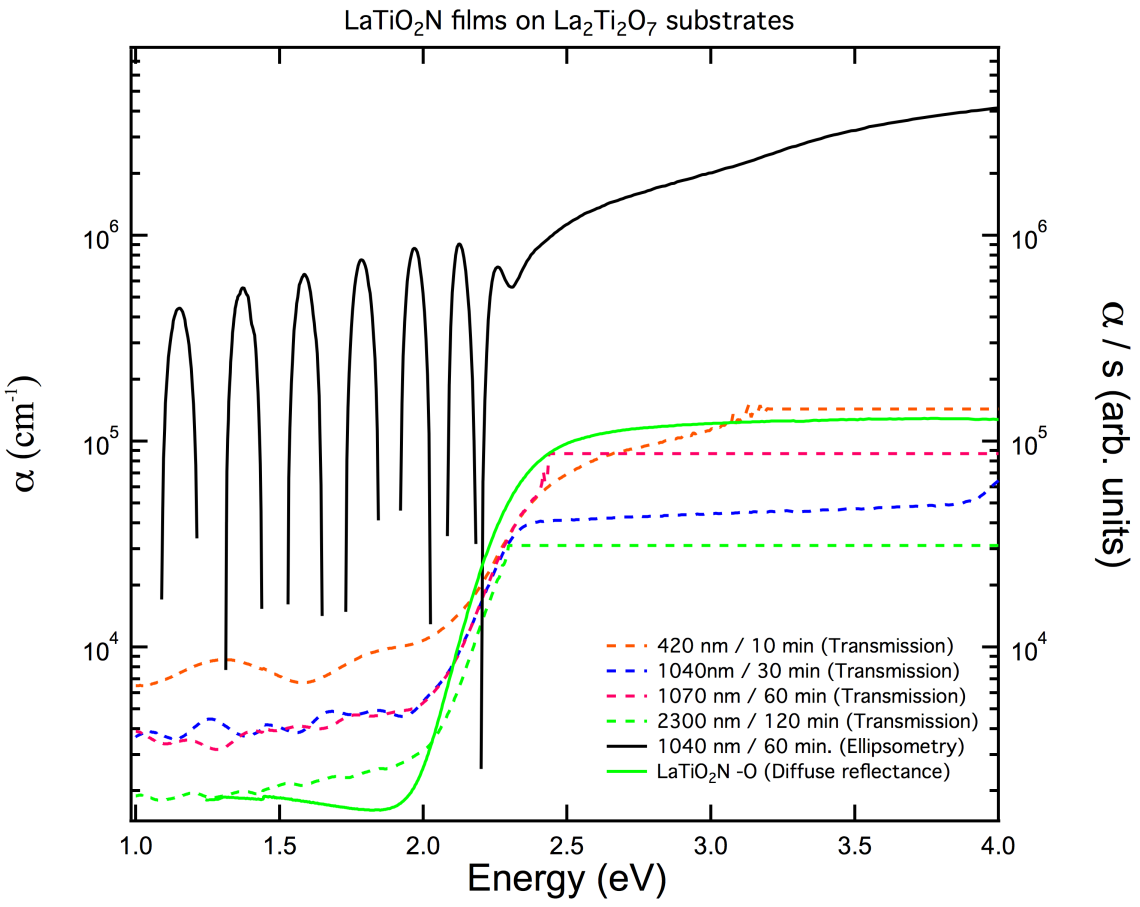

Figure S2.15 The un-scaled absorption of $LaTiO_2N$ collected using various techniques over the entire energy range collected.

References

1. Tan, M. X.; Laibinis, P. E.; Nguyen, S. T.; Kesselman, J. M.; Stanton, C. E.; Lewis, N. S., Principles and Applications of Semiconductor Photoelectrochemistry. *Prog. Inorg. Chem.* **1994,** *41*, 21-145.

2. Dry, M. E., The Fischer–Tropsch process: 1950–2000. *Catal. Today* **2002,** *71*, 227-241.

3. Honda, K.; Fujishima, A., Electrochemical Photolysis of Water at a Semiconductor Electrode. *Nature* **1972,** *238*, 37-38.

4. Krol, R. v. d., Yongqi Liand, Joop Schoonman, Solar hydrogen production with nanostructured metal oxides. *J. Mater. Chem.* **2008,** *18*, 2311-2320.

5. Zou, Z.; Ye, J.; Sayama, K.; Arakawa, H., Direct Splitting of Water Under Visible Light Irradiation with an Oxide Semiconductor Photocatalyst. *Nature* **2001,** *414*, 625-627.

6. Kudo, A.; Miseki, Y., Heterogeneous photocatalyst materials for water splitting. *Chem. Soc. Rev.* **2009,** *38*, 253-278.

7. Maeda, K., Kazunari Domen, New Non-Oxide Photocatalysts Designed for Overall Water Splitting under Visible Light. *J. Phys. Chem. C* **2007,** *111*, 7851-7861.

8. Maeda, K.; Domen, K., New Non-Oxide Photocatalysts Designed for Overall Water Splitting under Visible Light. *The Journal of Physical Chemistry C* **2007,** *111* (22), 7851-7861.

9. Maeda, K.; Domen, K., Solid Solution of GaN and ZnO as a Stable Photocatalyst for Overall Water Splitting under Visible Light. *Chem. Mater.* **2010,** *22* (2), 612-623.

10. Fuertes, A., Chemistry and applications of oxynitride perovskites. *J. Mater. Chem.* **2012,** *22* (8), 3293–3299.

11. Ebbinghaus, S. G.; Abicht, H.-P.; Dronskowski, R.; Müller, T.; Reller, A.; Weidenkaff, A., Perovskite-related oxynitrides – Recent developments in synthesis, characterisation and investigations of physical properties. *Prog. Solid State Chem.* **2009,** *37* (2-3), 173-205.

12. Tessier, F.; Maillard, P.; Cheviré, F.; Domen, K.; Kikkawa, S., Optical properties of oxynitride powders. *J. Ceram. Soc. Jpn.* **2009,** *117* (1), 1-5.

13. Kasahara, A.; Nukumizu, K.; Hitoki, G.; Takata, T.; Kondo, J. N.; Hara, M.; Kobayashi, H.; Domen, K., Photoreactions on $LaTiO_2N$ under Visible Light Irradiation. *J. Phys. Chem. A* **2002,** *106* (29), 6750-6753.

14. Glazer, A., The classification of tilted octahedra in perovskites. *Acta Crystallographica Section B* **1972,** *28* (11), 3384-3392.

15. Woodward, P. M., Octahedral Tilting in Perovskites. I. Geometrical Considerations. *Acta Crystallogr. Sect. B: Struct. Sci.* **1997,** *B53*, 32-43.

16. Lufaso, M. W.; Woodward, P. M., Jahn-Teller distortions, cation ordering and octahedral tilting in perovskites. *Acta Crystallogr. Sect. B: Struct. Sci.* **2004,** *B60*, 10-20.

17. Levin, I.; Bendersky, L. A., Symmetry classifcation of the layered perovskite-derived $A_nB_nX_{3n+2}$ structures. *Acta Crystallogr. Sect. B: Struct. Sci.* **1999,** *55* (6), 853-866.

18. Foner, S., Versatile and Sensitive VibratingSample Magnetometer. *Rev. Sci. Instrum.* **1959,** *30* (7), 548-557.

19. Martin, D. H., *Magnetism in Solids*. Iliffe Books Ltd.: London, 1967.

20. Kittel, C., *Introduction to Solid State Physics*. Fifth Edition ed.; John Whiley and Sons, Inc.: New York, 1976.

21. Bunker, G., *Introduction to XAFS: A Practical guide to X-ray Absorption Fine Structure Spectroscopy*. Cambridge University Press: New York, United States of America, 2010; p 260.

22. Wendlandt, W. W.; Hecht, H. G., *Reflectance Spectroscopy*. Interscience Publishers: United States, 1966; Vol. 21.

23. Torrent, J.; Barron, V., Diffuse Reflectance Spectroscopy. In *Methods of Soil Analysis. Part 5. Mineralogical Methods.*, Soil Science Society of America: Madison, 2008; Vol. 5, pp 367-385.

24. Kubelka; Munk, The Kubelka-Munk Theory of Reflectance. *Zeit. Für Tekn. Physik* **1931,** *12*.

25. Pankove, J. I., *Optical Properties in Semiconductors*. Dover Publications: New York, 1971.

26. Giacovazzo, C.; Monaco, H. L.; Artioli, G.; Viterbo, D.; Ferraris, G.; Gilli, G.; Zanotti, G.; Catti, M., *Fundamentals of Crystallography*. 2 ed.; Oxford University Press: New York, 2002; Vol. 7, p 825.

27. Farrow, C. L.; Juhas, P.; Liu, J. W.; Bryndin, D.; Bozin, E. S.; Bloch, J.; Proffen, T.; Billinge, S. J. L., PDFfit2 and PDFgui: computer programs for studying nanostructures in crystals. *J. Phys.: Condens. Matter* **2007,** *19*, 335219.

28. Tucker, M. G.; Keen, D. A.; Dove, M. T.; Goodwin, A. L.; Hui, Q., RMCProfile: reverse Monte Carlo for polycrystalline materials. *J. Phys.: Condens. Matter* **2007,** *19* (33).

29. Fultz, B.; Howe, J. M., *Transmission Electron Microscopy and Diffractometry of Materials*. 2 ed.; Springer-Verlag: Berlin; Heidelberg; New York, 2002.

30. Malingowski, A. C.; Stephens, P. W.; Huq, A.; Huang, Q.; Khalid, S.; Khalifah, P. G., Substitutional Mechanism of Ni into the Wide-Band-Gap Semiconductor $InTaO_4$ and Its Implications for Water Splitting Activity in the Wolframite Structure Type. *Inorg. Chem.* **2012,** *51* (11), 6096-6103.

31. Strehlow, W. H.; Cook, E. L., Compilation of Energy Band Gaps in Elemental and Binary Compound Semiconductors and Insulators. *J. Phys. Chem. Ref. Data* **1973,** *2*, 163.

32. Ikeda, S.; Fubuki, M.; Takahara, Y. K.; Matsumura, M., Photocatalytic activity of hydrothermally synthesized tantalate pyrochlores for overall water splitting. *Appl. Catal., A* **2006,** *300* (2), 186-190.

33. Matsushima; Shigenori; Obata, K.; Nakamura, H.; Arai, M.; Kobayashi, K., First-principles energy band calculation for undoped and Ni-doped $InTaO_4$ with layered wolframite-type structure. *J. Phys. Chem. Solids* **2003,** *64*, 2417-2421.

34. Chang, H.; Kong, K.; Choi, Y. S.; Choi, Y.; Baeg, J.-O.; Moon, S.-J., First Principles Studies of Doped $InTaO_4$ for Photocatalytic Applications. *C.R. Chimie* **2006,** *9*, 841-845.

35. Chang, H.; Kong, K.; Choi, Y. S.; In, E.; Choi, Y.; Baeg, J.-O.; Moon, S.-J., Electronic Structures of $InTaO_4$, a Promising Photocatalyst. *Chem. Phys. Lett.* **2004,** *398*, 449-452.

36. Oshikiri, M., Mauro Boero, Jinhua Ye, Zhigang Zou, Giyuu Kido, Electronic Structures of Promising Photocatlysts $InMO_4$ (M = V, Nb, Ta) and $BiVO_4$ for Water Decomposition in the Visible Wavelength Region. *J. Chem. Phys.* **2002,** *117* (15), 7313-7318.

37. Li, G.-L.; Yin, Z., Theoretical insight into the electronic, optical and photocatalytic properties of $InMO_4$ (M = V, Nb, Ta) photocatalysts. *PCCP* **2011,** *13* (7), 2824-2833.

38. Rico, V. J.; Frutos, F.; Yubero, F.; Espinos, J. P.; Gonzáles-Elipe, A. R., Synthesis, characterization, and photoactivity of $InTaO_4$ and $In_{0.9}Ni_{0.1}TaO_4$ thin films prepared by electron evaporation. *J. Vac. Sci. Technol., A* **2010,** *28* (1), 127-134.

39. Harneit, O.; Muller-Buschbaum, H., $InTaO_4$ und $GaTaO_4$ mit geordneter und ungeordneter Metallverteilung. *J. Alloys Compd.* **1993,** *194*, 101-103.

40. Villars, P.; Cenzual, K. *Pearson's Crystal Data: Crystal Structure Database for Inorganic Compounds (on CD-ROM), Version 1.0*, 1.0; ASM International: Materials Park, Ohio, USA, 2007/ 8.

41. Shannon, R. D., Revised effective ionic radii and systematic studies of interatomic distances in halides and chalcogenides. *Acta Crystallogr. Sect. A: Found. Crystallogr.* **1976,** *A32* (5), 751-767.

42. Zou, Z.; Ye, J.; Sayama, K.; Arakawa, H., Effect of Ni substitution on the structure and photocatalytic activity of $InTaO_4$ under visible light irradiation. *J. Mater. Res.* **2002,** *17* (6), 1419-1424.

43. Zou, Z.; Ye, J.; Arakawa, H., Structural Properties of $InNbO_4$ and $InTaO_4$: Correlation with Photocatalytic and Photophysical Properties. *Chem. Phys. Lett.* **2000,** *332* (3-4), 271-277.

44. Zou, Z.; Ye, J.; Abe, R.; Sayama, K.; Arakawa, H. In *Effect of 3d transition-metal (M) doping in* $In_{1-x}M_x\ TaO_4$ *photocatalysts on water splitting under visible light irradiation* Studies in Surface Science and Catalysis 2002, Proceedings of the Fourth Tokyo conference on Advance Catalytic Science and Technology, 2003; pp 165-168.

45. Douiheche, M.; Haberkorn, R.; Beck, H. P., On the Photocatalytic Performance of Indium Tantalate and its Modifications. *Z. Naturforsch., B: Chem. Sci.* **2008,** *63b*, 1160-1168.

46. Newville, M., IFEFFIT: interactive EXAFS analysis and FEFF fitting. *J. Synchrotron Rad.* **2001,** *8*, 322-324.

47. Ravel, B., ATOMS: crystallography for the X-ray absorption spectroscopist. *J. Synchrotron Rad.* **2001,** *8*, 314-316.

48. Ravel, B.; Newville, M., ATHENA, ARTEMUS, HEPHAESTUS: data analysis for X-ray absorption spectroscopy using IFEFFIT. *J. Synchrotron Rad.* **2005,** *12*, 537-541.

49. Murphy, C. P.; Sethuram, B.; Rao, T. N., Oxidation by Tetravalent Nickel. *Z. phys. Chemie, Leipzig* **1986,** *267* (6), 1212-1218.

50. *IGOR Pro*, 6.12; WaveMetrics: Lake Oswego, OR, USA, 2009.

51. Cotton, F. A.; Wilkinson, G., *Advanced Inorganic Chemistry*. 5 ed.; Wiley-Interscience: New York, 1988.

52. Kubelka, P.; Munk, F., An Article on Optics of Paint Layers. *Zeit. Für Tekn. Physik* **1931,** *12*, 593.

53. Weiher, R. L.; Ley, R. P., Optical Properties of Indium Oxide. *J. Appl. Phys.* **1966,** *37* (1), 299-302.

54. Zou, Z.; Ye, J.; Arakawa, H., Photophysical and Photocatalytic Properties of $InMO_4$ (M = Nb^{5+}, Ta^{5+}) Under Visible Light Irradiation. *Mater. Res. Bull.* **2001,** *36*, 1185-1193.

55. Zou, Z.; Ye, J.; Arakawa, H., Photocatalytic behavior of a new series of $In_{0.8}M_{0.2}TaO_4$ (M = Ni, Cu, Fe) photocatalysts in aqueous solutions. *Catal. Lett.* **2001,** *75* (3-4), 209-213.

56. Zou, Z.; Ye, J.; Arakawa, H., Surface Charecterization of Nanoparticles of $NiO_x/In_{0.9}Ni_{0.1}TaO_4$: Effects on Photocatalytic Activity. *J. Phys. Chem. B* **2002,** *106* (51), 13098-13101.

57. Zou, Z.; Ye, J.; Arakawa, H., Photocatalytic water splitting into H_2 and/or O_2 under UVand visiblelight irradiation with a semiconductor photocatalyst. *Int. J. Hydrogen Energy* **2003,** *28*, 663-669.

58. Zou, Z.; Ye, J.; Sayama, K.; Arakawa, H., Photocatalytic Hydrogen and Oxygen Formation Under Visible Light Irradiation with M-Doped $InTaO_4$ (M = Mn, Fe, Co, Ni and Cu) Photocatalysts. *Journal of Phochemistry and Photobiology A* **2002,** *148*, 65-69.

59. Zou, Z.; Arakawa, H., Direct water splitting into H_2 and O_2 under visible light irradiation with a new series of mixed oxide semiconductor photocatalysts. *Journal of Phoochemistry and Photobiology A* **2003,** *158*, 145-162.

60. Kasahara, A.; Nukumizu, K.; Takata, T.; Kondo, J. N.; Hara, M.; Kobayashi, H.; Domen, K., $LaTiO_2N$ as a Visible-Light (≤600 nm)-Driven Photocatalyst (2). *J. Phys. Chem. B* **2003,** *107* (3), 791-797.

61. Le Paven-Thivet, C.; Ishikawa, A.; Ziani, A.; Le Gendre, L.; Yoshida, M.; Kubota, J.; Tessier, F.; Domen, K., Photoelectrochemical Properties of Crystalline Perovskite Lanthanum Titanium Oxynitride Films under Visible Light. *The Journal of Physical Chemistry C* **2009,** *113* (15), 6156-6162.

62. Zhang, F.; Yamakata, A.; Maeda, K.; Moriya, Y.; Takata, T.; Kubota, J.; Teshima, K.; Oishi, S.; Domen, K., Cobalt-Modified Porous Single-Crystalline $LaTiO_2N$ for Highly Efficient Water Oxidation under Visible Light. *J. Am. Chem. Soc.* **2012,** *134* (20), 8348-8351.

63. Maegli, A. E.; Pokrant, S.; Hisatomi, T.; Trottmann, M.; Domen, K.; Weidenkaff, A., Enhancement of Photocatalytic Water Oxidation by the Morphological Control of $LaTiO_2N$ and Cobalt Oxide Catalysts. *J. Phys. Chem. C* **2013,** *Article ASAP*.

64. Aguiar, R.; Kalytta, A.; Reller, A.; Weidenkaff, A.; Ebbinghaus, S. G., Photocatalytic decomposition of acetone using $LaTi(O,N)_3$ nanoparticles under visible light irradiation. *J. Mater. Chem.* **2008,** *18* (36), 4260-5.

65. Ebbinghaus, S. G.; Aguiar, R.; Weidenkaff, A.; Gsell, S.; Reller, A., Topotactical growth of thick perovskite oxynitride layers by nitridation of single crystalline oxides. *Solid State Sciences* **2008,** *10* (6), 709-716.

66. Ziani, A.; Paven-Thivet, C. L.; Gendre, L. L.; Fasquelle, D.; Carru, J. C.; Tessier, F.; Pinel, J., Structural and dielectric properties of oxynitride perovskite $LaTiO_xN_y$ thin films. *Thin Solid Films* **2008,** *517* (2), 544-549.

67. Ziani, A.; Le Paven-Thivet, C.; Fasquelle, D.; Le Gendre, L.; Benzerga, R.; Tessier, F.; Cheviré, F.; Carru, J. C.; Sharaiha, A., Dielectric oxynitride $LaTiO_xN_y$ thin films deposited by reactive radio-frequency sputtering. *Thin Solid Films* **2011**.

68. Le Paven-Thivet, C.; Le Gendre, L.; Le Castrec, J.; Cheviré, F.; Tessier, F.; Pinel, J., Oxynitride perovskite $LaTiO_xN_y$ thin films deposited by reactive sputtering. *Prog. Solid State Chem.* **2007,** *35* (2-4), 299-308.

69. Aguiar, R.; Weidenkaff, A.; Schneider, C. W.; Reller, A.; Ebbinghaus, S. G., Synthesis and properties of oxynitrides $(La,Sr)Ti(O,N)_3$ thin films. *Prog. Solid State Chem.* **2007,** *35* (2-4), 291-298.

70. Abe, R.; Higashi, M.; Sayama, K.; Abe, Y.; Sugihara, H., Photocatalytic Activity of R_3MO_7 and $R_2Ti_2O_7$ (R = Y, Gd, La; M = Nb, Ta) for Water Splitting into H_2 and O_2. *The Journal of Physical Chemistry B* **2006,** *110* (5), 2219-2226.

71. Cheviré, F.; Tessier, F.; Marchand, R., Optical Properties of the Perovskite Solid Solution $LaTiO_2N–ATiO_3$ (A = Sr, Ba). *Eur. J. Inorg. Chem.* **2006,** *2006* (6), 1223–1230.

72. Jarrendahl, K.; Arwinb, H., Multiple sample analysis of spectroscopic ellipsometry data of semi-transparent films. *Thin Solid Films* **1998,** *313-314* (13), 114-118.

73. Agilent *CrysAlis PRO*, Agilent Technologies: Yarnton, Oxfordshire, England, 2010.

74. Burla, M. C.; Caliandro, R.; Camalli, M.; Carrozzini, B.; Cascarano, G. L.; Giacovazzo, C.; Mallamo, M.; Mazzone, A.; Polidori, G.; Spagna, R., SIR2011: a new package for crystal structure determination and refinement. *J. Appl. Crystallogr.* **2012,** *45* (2), 357-361.

75. Sheldrick, G. M. *SHELXS-97 - Program for Crystal Structure Refinment*, University of Göttingen: Germany, 1997.

76. Synowicki, R. A., Suppression of backside reflections from transparent substrates. *phys. stat. sol. (c)* **2008,** *5* (5), 1085-1088.

77. *Spectroscopic Ellipsometry Software WVASE32*, J. A. Woollam Co., Inc.: 2002.

78. Gillespie, J. B.; Lindberg, J. D.; Laude, L. S., Kubelka-Munk Optical Coefficients for a Barium Sulfate White Reflectance Standard. *Appl. Opt.* **1975,** *14* (4), 807-809.

79. Patterson, E. M.; Shelden, C. E.; Stockton, B. H., Kubelka-Munk optical properties of a barium sulfate white reflectance standard. *Appl. Opt.* **1977,** *16* (3), 729-732.

80. Blöchl, P. E., Projector augmented-wave method. *Phys. Rev. B: Condens. Matter* **1994,** *50* (24), 17953-17979.

81. Kresse, G.; Furthmuller, J., Efficient iterative schemes for ab initio total-energy calculations using a plane-wave basis set. *Phys. Rev. B: Condens. Matter* **1996,** *54* (16), 11169-11186.

82. Kresse, G.; Joubert, D., From ultrasoft pseudopotentials to the projector augmented-wave method. *Phys. Rev. B: Condens. Matter* **1999,** *59* (3), 1758-1775.

83. Clarke, S. J.; Guinot, B. P.; Michie, C. W.; Calmont, M. J. C.; Rosseinsky, M. J., Oxynitride Perovskites: Synthesis and Structures of $LaZrO_2N$, $NdTiO_2N$, and $LaTiO_2N$ and Comparison with Oxide Perovskites. *Chem. Mater.* **2002,** *14* (1), 288-294.

84. Kang, W.; Hybersten, M. S., 2010.

85. Connolly, J. W. D.; Williams, A. R., Density-functional theory applied to phase transformations in transition-metal alloys. *Phys. Rev. B: Condens. Matter* **1983,** *27* (8), 5169-5172.

86. Sanchez, J. M.; Ducastelle, F.; Gratias, D., Generalized cluster description of multicomponent systems. *Physica A* **1984,** *128* (1-2), 334-350.

87. Van de Walle, A.; Asta, M.; Ceder, G., The alloy theoretic automated toolkit: A users guide. *Calphad* **2002,** *26* (4), 539-553.

88. Van de Walle, A., Multicomponent multisublattice alloys, nonconfigurational entropy and other additions to the Alloy Theoretic Automated Toolkit. *Calphad* **2009,** *33* (2), 266-278.

89. Onida, G.; Reining, L.; Rubio, A., Electronic excitations: density-functional versus many-body Green's-function approaches. *Reviews of Modern Physics* **2002,** *74* (2), 601-659.

90. Kang, W.; Hybertsen, M. S., Quasiparticle and Optical Properties of Rutile and Anatase TiO_2. *Phys. Rev. B: Condens. Matter* **2010,** *Submitted*.

91. Levine, Z. H.; Allan, D. C., Quasiparticle calculation of the dielectric response of silicon and germanium. *Phys. Rev. B: Condens. Matter* **1991,** *43* (5), 4187-4207.

92. Guide to Using WVASE32. J. A. Woollam Co., Inc.: 2010.

93. Tompkins, H. G.; McGahan, W. A., *Spectroscopic Ellipsometry and Reflectometry: A User's Guide*. Wiley-Interscience: United States of America, 1999.

94. Woollam, J.; Johs, B.; Herzinger, C. M.; Hilfiker, J.; Synowicki, R.; Bungay, C. L., Overview of Variable Angle Spectroscopic Ellipsometry (VASE), Part I: Basic Theory and Typical Applications. In *Optical Metrology*, SPIE: Denver, Colorado, 1999; Vol. CR72, pp 3-28.

95. Pascual, J.; Camassel, J.; Mathieu, H., Fine structure in the intrinsic absorption edge of TiO_2. *Phys. Rev. B: Condens. Matter* **1978,** *18* (10), 5606-5614.

96. Kavan, L.; Grätzel, M.; Gilbert, S. E.; Klemenz, C.; Scheel, H. J., Electrochemical and Photoelectrochemical Investigation of Single-Crystal Anatase. *J. Am. Chem. Soc.* **1996,** *118* (28), 6716-6723.

97. Jellison Jr., G. E., Data analysis for spectroscopic ellipsometry. *Thin Solid Films* **1993,** *234* (1-2), 416-422.

98. Burmistrova, P., 2014.

99. Sturge, M. D., Optical Absorption of Gallium Arsenide between 0.6 and 2.75 eV. *Physical Review* **1962,** *127* (3), 768-773.

100. *TOPAS V4*, Bruker AXS: Karlsruhe, Germany, 2008.

101. Takamura, T.; Moriya, Y.; Takase, M.; Matsukawa, M.; Yamaguchi, A.; Teshima, K.; Oishi, S.; Khalifah, P. G.; Domen, K., Photocatalytic Activity of $LaTiO_2N$ Derived from La-rich La-Ti^{IV} Binary Oxide Precursors and Its Relationship with Ti-Reduced Species. 2014.

102. Gendre, L. L.; Marchland, R.; Laurent, Y., A New Class of Inorganic Cpmpounds Containing Dinitrogen-Metal Bonds. *J. Eur. Ceram. Soc.* **1997,** *17*, 1813-1818.

103. Tessier, F.; Le Gendre, L.; Cheviré, F.; Marchand, R.; Navrotsky, A., Thermochemistry of a New Class of Materials Containing Dinitrogen Pairs in an Oxide Matrix. *Chem. Mater.* **2005,** *17* (13), 3570-3574.